þÿ D e e p N - b a n d n u l l i n g i n t e r f e r o m e t r i c i m a g i n g o f ± L y r a

Auteur : Rousseau, Hélène
Promoteur(s) : Defrère, Denis
Faculté : Faculté des Sciences
Diplôme : Master en sciences spatiales, à finalité approfondie
Année académique : 2019-2020
URI/URL : http://hdl.handle.net/2268.2/9332

University of Liège

Master in Space Sciences

Deep N-band nulling interferometric imaging of α Lyrae and β Leo with the LBTI

presented by Hélène Rousseau

Under the supervision of Dr. Denis Defrère

Jury members:

Dr. Olivier Absil

Dr. Anne-Lise Maire

Dr. Steve Ertel

Pr. Philip Hinz

Academic year 2019/2020

Abstract

Since the discovery of an exoplanet around a main-sequence star by Mayor and Queloz (1995) the field of exoplanetology has never stopped to expend. Nowadays, several thousands confirmed exoplanets have been discovered and some other thousands are waiting for confirmation. However, even if the number of "known" exoplanets keeps increasing, we have only very few information about them. Do they have an atmosphere? What is their chemical composition? What is their surface temperature? This is only a few examples of the questions still unanswered for the vast majority of confirmed exoplanets. Characterizing exoplanets is one of the most challenging topic in current exoplanetology, the ultimate goal being to one day be able to determine the habitability of an exoplanet and the possible presence of life.

To characterize exoplanets, we nowadays depend on two main methods: the transit method where the atmosphere is characterized using the photons coming from the host star and passing through the atmosphere of the exoplanet before reaching us, and direct imaging where the photons from the planets (reflection of the host star light or thermal emission) are directly recovered and used for the characterization. Direct imaging domain itself decomposed into two main methods: coronography and nulling interferometry. In this master thesis, we will focus on this last method. In both domains the planet faintness is a huge challenge to the characterization. Indeed a terrestrial planet is about 10^7 fainter than its host star and 10^9 than the Earth atmospheric background at 10 μm. Transit method is in addition limited to planets orbiting close to their host star, and which actually pass in front of it seen from Earth. On the other hand direct imaging techniques have to deal with the angular separation to the star and face the challenge to detect, let alone characterize, planets close to their host star. The advantage of nulling interferometry is to combine the angular resolution of interferometry and star light suppression.

In this master thesis, we will focus on two post-processing methods used in direct imaging: Angular Differential Imaging (ADI, Marois et al 2006) and Reference (star) Differential Imaging (RDI, Lafreniere et al 2007; Ruane et al 2019). We will compare these methods on different datasets obtained by nulling interferometry thanks to NASA's Large Binocular Telescope Interferometer (LBTI) during the HOSTS survey (Hunt for Observable Signatures of Terrestrial Systems, Ertel et al 2020) which was looking for exozodiacal disks in the habitable zone of the targeted stars to put constraints on their impact on exoplanet imaging. Our goal will be twofold: looking for the signature of resolved circumstellar emission around the target stars and characterize the imaging performance of the LBTI in its nulling mode. Those datasets present different ranges and distributions of parallactic angles, photometry of the star, level of the nulling quality, flux distribution and we intend to retrieve for a given type of dataset (for example with small parallactic angles ranges) an optimal method. In order to achieve this goal we will, in the following, use the VIP python library (Gonzalez et al 2017) to perform analysis with the different methods (ADI, RDI) and different models of PSF subtraction (median subtraction, least-square approximation, full-frame PCA, etc) on all the different datasets. Finally, we will give a conclusion for each method on which type of dataset is the most adapted, and provide an helpful guide on which method is optimal for the processing of a particular dataset.

Acknowledgement

First and foremost, I would like to thank Dr. Denis Defrère who supervised me all along this master thesis and was extremely available for any question I might have. I am very grateful for the guidelines and numerous feedback he gave me as well as for his patience and kindness.

I would like to thanks the jury members for the helpful feedback they gave me on my preliminary results. They allowed me to significantly improve my work. I am also grateful for the time they accorded to my work.

Then, I would also like to thanks Dr. Valentin Christiaens for answering my questions about the RDI mode of VIP. Thanks to him I was able to rapidly deal with this part of VIP and this allowed me to make important comparisons for this work.

Finally I would like to thanks my family and my friends for their help and their support. I would, in particular, thank Mathilde Timmermans, Alexandre de Becker and my sister for their help in improving my report. I would also gratefully thank my parents for allowing me to pursue my studies in perfect conditions.

Contents

1 Introduction **6**
- 1.1 Exoplanets and Habitable Zones . . . 6
- 1.2 Detection methods . . . 7
- 1.3 Exozodis . . . 10
- 1.4 HOSTS Survey . . . 11

2 Nulling Interferometry **13**

3 Data description **18**
- 3.1 Data acquisition . . . 18
- 3.2 Image cubes and frame selection . . . 19
  - 3.2.1 α Lyrae . . . 19
  - 3.2.2 β Leo . . . 21

4 Data Processing **23**
- 4.1 VIP . . . 23
- 4.2 No PSF subtraction . . . 24
- 4.3 ADI . . . 24
- 4.4 RDI . . . 26

5 Data Analysis **27**
- 5.1 No PSF subtraction . . . 27
  - 5.1.1 α Lyrae . . . 27
  - 5.1.2 β Leo . . . 29
- 5.2 ADI processing . . . 30
  - 5.2.1 α Lyrae . . . 30
  - 5.2.2 β Leo . . . 39
  - 5.2.3 Improvement of the contrast curves . . . 42
- 5.3 RDI processing . . . 47
  - 5.3.1 α Lyrae . . . 47
  - 5.3.2 β Leo . . . 54

6 Comparison of the methods **59**
- 6.1 α Lyrae . . . 59
- 6.2 β Leo . . . 61
- 6.3 Comparison of α Lyrae and β Leo results . . . 63

7 Conclusion and Prospects **65**

Bibliography **67**

Glossary

ADI: Angular Differential Imaging.

ADU: Analogue to Digital Units.

AO: Adaptive Optics.

AU: Astronomical Unit.

CAL: Calibrator.

EEID: Equivalent to Earth Insolation Distance.

FFPCA: Full-Frame Principal Component Analysis.

FOV: Field Of View.

FPC: Fast Pathlength Corrector.

HOSTS: Hunt for Observable Signatures of Terrestrial Systems.

IR: Infrared.

JWST: James Webb Space Telescope.

LBT: Large Binocular Telescope.

LBTI: Large Binocular Telescope Interferometer.

LLSG: Local Low-rank Sparse Gaussian noise components analysis.

MNT: Maximum Null leak Threshold.

NMF: Negative Matrix Factorisation for Angular Differential Imaging.

OB: Observational Bloc.

PC: Principal Component.

PCA: Principal Component Analysis.

PSF: Point Spread Function.

RDI: Referential Differential Imaging.

S/N map: Signal to Noise ratio map.

SCI: Scientific target.

SDI: multi-Spectral Differential Imaging.

SPC: Slow Pathlength Corrector.

VIP: Vortex Image Processing.

Introduction

1.1 Exoplanets and Habitable Zones

With height planets, countless dwarf planets and smaller bodies, our Solar system already shows us a wide variety of celestial objects. Focusing only on the planets, we can already see an important diversity with the small terrestrial planets like Mercury and Mars which have very thin or no atmosphere, Venus and the Earth, bigger, and with much more consequent atmospheres, the ice giant like Uranus and Neptune and the gaseous giant like Jupiter and Saturn. When the exoplanetology field emerged the diversity grew beyond our imagination, the solar system planets were transposed to extrasolar planets with in particular the hot-Jupiters, gaseous giant about the size of Jupiter but orbiting much closer to their star, the mini-Neptunes, super-Earths and Earth-like planets.Those denominations in themselves show the hope of astrophysicist to find somewhere else planets similar to those in our solar system, and in particular similar to the Earth.

Indeed since we learned that stars are as many potential planetary systems, we wonder whether Earth is unique and the only planet hosting life. These questions bring many others: would life be similar to the one we know? How frequent is it? What are the conditions those other life forms need to appear and develop? Is intelligence emerging whenever life appear? And so many others that it would be truly impossible to quote them all. Before answering those questions there is still a long way to go and many preliminary questions need to be answered. To do so we need on one hand to detect even more planets in even more systems to reduce as much as possible the observational biases nowadays present in the data. Also the detection methods and the instruments at our disposal need to be improved to reach much higher sensitivity and be able to detect much fainter signals. Reducing the biases will already help to further constraint planetary formation models, the planets number in our galaxy, the diversity of systems architectures and doing so giving hints of answers about life on other planets. The use of different detection methods is already a great step in the reduction of biases as they are not sensitive to the same exoplanet parameters. The detection methods and their sensitivities will be discussed in the following section.

On the other hand, detecting more planets is insufficient to answer the aforementioned questions, we need to learn a lot more about the detected exoplanets and their environment. This is called exoplanet characterization. This emerging domain would allow to answer a lot more questions than simple detection, in particular about their atmosphere, composition, temperature, masses, densities, radii but also if they are tidally locked with their host star, if they are in resonance with other planets, if they possess one or several moons, etc. With extremely precise instruments those information could in theory answer the questions about life in the universe but this is nowadays very unlikely. However, this knowledge could provide precious information on the formation and evolution of the planets, if they possess habitable conditions, if they did in the past, and how long they will in the future. Being able of efficiently characterizing a large number of planets will represent a huge step in our understanding of life appearance in the universe.

For some exoplanets, detected with particular methods some of these parameters are already known, often the masses and the radii, but in most of the cases we know very little of the detected (and confirmed) exoplanets. Sadly not all the detection methods allow further characterization, emphasizing one more time the advantages to use several methods. This will also be discussed in the following section.

Of course detecting and characterizing larger exoplanets similar to the giants gaseous planets in our solar system is much easier than small terrestrial ones as all the detection methods we use nowadays are more sensitive to larger or more massive planets. However as life as we know it appears on a terrestrial planet, this is on those, fainter, harder to detect, signals that we will focus on. Indeed, to efficiently search for life outside our solar system we need to define the most probable planets able to host life. This is why the notion of habitable zone around other stars has been defined. It selects, among the variety of planets existing and theorized, parameters we though mandatory for life appearance.The most important parameters is the capability of the planet to sustain large amounts of liquid water on its surface which with the actual knowledge seems to be mandatory for life appearance. However a lot of other parameters are added to this first one. If some of them can see completely justified (presence of an atmosphere) some might seem much more restrictive. In the standard definition it notably excludes the gaseous planets and the moons as the only life we know about appear on a terrestrial planet and that detecting moons is even more challenging that detecting exoplanets. It also excludes the planetary systems with O, B and A-type stars, due to their too short lifetime, and multiple stars systems due to the gravitational instabilities this would generate for the potential exoplanets. However several alternative definitions of habitable zones have been introduced later to better take into account the huge diversity of exoplanets and planetary systems. Those studied, among others, the impact of the mass, the rotational period, the composition of the atmosphere and the eccentricity of the orbit. The habitable zone notion has also been extend to earlier type stars and multiple stars systems and even pre- and post-main sequence stars. However those alternative definitions would probably not be used in the first place as the main goal of the habitable zone definition is to efficiently select targets which are the most probable to host life. Nonetheless, it very likely that with the progress of exoplanet characterization more exotic definition will be used.

As describe above the habitable zone is a really important concept and the region around the star we want to explore because this is where life is more likely to appear. However, in our solar system, the whole habitable zone contains zodiacal dust. To be able to detect small terrestrial planets promising for life appearance, one first needs to carefully consider the light emission coming from this dust. We will discuss in more details of the zodiacal disks and the issue it represents for exoplanet detection in a following section.

1.2 Detection methods

Since the premises of exoplanetology, many detection methods have been proposed: transit, radial velocity, astrometry, gravitational lensing and direct imaging. Among those, the transit method is the one with the greatest number of detection (3164 exoplanets, NASA exoplanet archive 2020-05-21), followed by the radial velocity method (802 exoplanets, NASA exoplanet archive 2020-05-21). The direct imaging method with fewer detections is however perfectly complementary with these two first techniques. In the following we propose a brief overview of these methods and their advantages

The principle of the transit method is to monitor the luminosity of the target star and to detect small drops in its lightcurve which would correspond to a planet passing in front of its host star. This technique is of course much more sensitive to close and big planets as the drop depth and frequency will depend on those two parameters. Indeed the larger the planet the greater the portion of the star it masks when passing in front. This is also true for the distance parameters, as the further away the planet, the smaller it will appear. The main limitation of this method is that the planets must actually pass in front of their host star seen from the Earth. This limits the detectable planets to those on orbits with an inclination close to 0° (0° corresponding to an axis joining the observation location to the center of the target star). The principle of this detection method is illustrated in Figure 1.1.

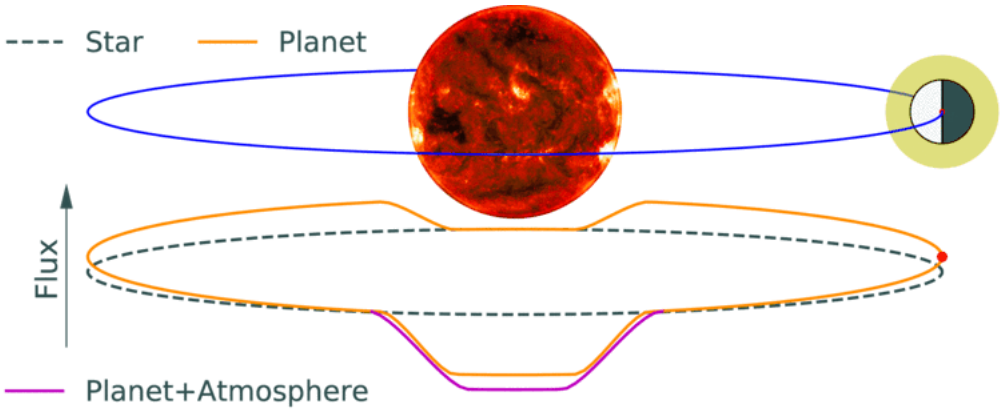

Figure 1.1: Schematic representation of the transit detection method principle

This limitation in angles put also an indirect upper limit on the distance at which the planet can be detectable with this method, as the further away it is the smaller the allowed angles range. Thanks to this method the orbital period of the exoplanets (if it is short enough to have been detected at least twice), as well as its distance from the star (if the orbital period is known) and an estimation of its radius can be provided. An important advantage of this method, excluding its great number of detections, is its capacity to further characterize the exoplanet. Indeed when the planet passes in front of its host star, a small fraction of the star light will go through the exoplanet atmosphere. Taking the spectrum of the star (and so of the planet too) at those particular moments, and comparing them to spectra taken when the planet is hiden by the star, we can retrieve information on the atmosphere of the exoplanet if it possesses one, such as its main components. This is however still very challenging to perform due to the smallness of the atmosphere compared to exoplanet, let alone to the star, and to the small portion of light passing through the atmosphere. Then this small amount of light might be dispersed in order to obtained a spectrum, which reduce again the amount of light we retrieve and are able to analyze. The next generation of space telescope like the James Webb Space Telescope (JWST) has been designed to be able to efficiently detect and characterize such atmosphere around late-type stars, and great knowledge is to be expected of this new generation of space telescopes in this domain.

Regarding the radial velocity method, we do not monitor the luminosity of the star but its spectrum. If a planet orbits a star, the gravitational interaction between them will cause a oscillation in the position of the star. This oscillation, if caused by an exoplanet will be periodic. This movement will be translated in the spectrum by a displacement of the spectral lines. Indeed if the planet creates a movement of the star toward us the star light will be blueshifted, on the other hand if its move the star forward us the light will be redshifted. Due to the nature of the gravitational interaction this method is more sensitive to close and massive exoplanets. It is interesting to note that if the effect of the gravitational interaction depends only on those two parameters, the effect on the spectra highly depends on the inclination of the orbit with respect to the 0° axis going from the observational location and the center of the star. Indeed in the case of a 90° inclination, the movement of the star due to the exoplanet will be fully contained in the plane perpendicular to this axis and will not induce blue- and redshift and thus will stay undetectable. The idea of the radial velocity method is shown in Figure 1.2

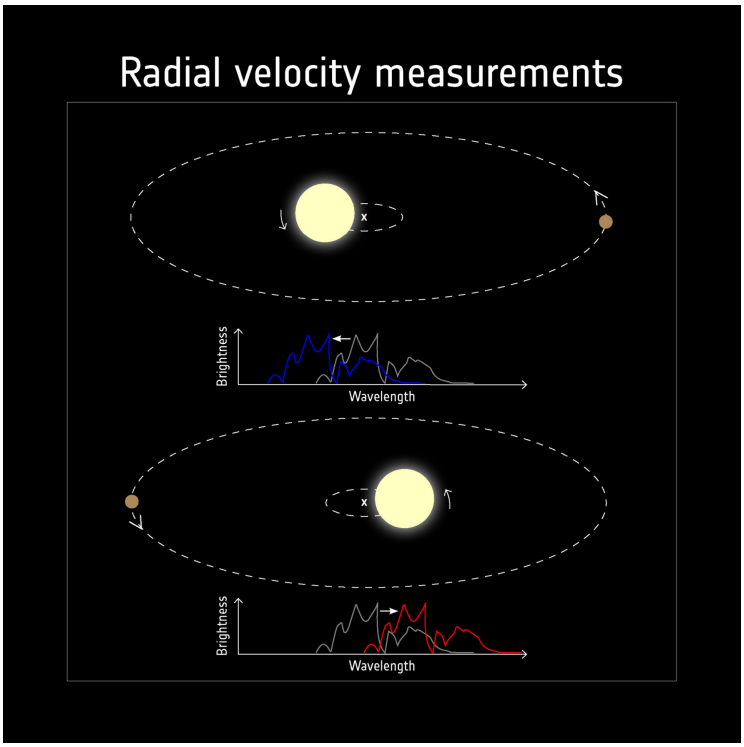

Figure 1.2: Schematic representation of the radial velocity detection method principle. With the movement of the planet the center of mass of the system oscillates and so do the star too. This oscillation induces a movement backward and forward the observer translated in blue- and red-shift in the spectrum of the star.

As the oscillation induced by the exoplanets remains extremely small, in particular for terrestrial planets, this in practice limits the angles of inclination of the orbit at which an exoplanet can be detected by this method. However this limit is not as critical as in the transit method and so allows detection further away from the star, if the planet is not too small to produce a detectable oscillation of the star. This method provides the orbital period of the exoplanet, its distance from the star, and put constraint on its minimum mass but do not allow further characterization of all its detected exoplanets as the spectrum of the exoplanet is lost in the one of its host star in most of the cases. However, in the case of exoplanets detected by the radial velocity method which transit and eclipse, it is possible to characterize them through the same process than in the transit method.

As we can see, the two previously described methods are more sensitive to close exoplanets, on the contrary, the direct imaging method is much sensitive to exoplanets orbiting further away from their host star. Indeed in direct imaging, as we want to retrieve the light of the exoplanet itself, and to get rid of the star light, the further the exoplanet orbit the easier it will be to detect. In direct imaging the two major issues are thus the angular separation and the contrast between the star and its potential companions. For instance, in the visible, a terrestrial exoplanet is about 10^{10} times less bright than its host star. In the infrared the situation is slightly better with a contrast of approximately 10^{7}. At those wavelengths however, the dominant noise is the Earth atmosphere (10^{9} times brighter than a terrestrial exoplanet) as the direct imaging is nowadays perform mostly from the ground. Several projects of direct imaging space telescopes are currently examined or in development which would greatly improve the achievable sensitivity by getting rid of the atmosphere turbulences and brightness. Direct imaging can be performed thanks to two techniques: coronography and nulling interferometry. In the first technique a single dish telescope can be used and the star light will be suppressed by a central mask, which blocks the major part of the star light and redirects the residuals toward the outer part of the beam; and a Lyot stop which reduces the effect of diffraction thus removing an important part of the remaining star light. In the original image a part of the light from the star is scattered through the images due to the atmospheric turbulences creating speckles which are removed in a great proportion thanks to adaptive optics which corrects the deformed wavefront thus refocusing the light contained in the

speckles in the core of the PSF. After greatly reducing the amount of star light received it is thus possible to detect much fainter objects. The working principle of the coronograph as well as an image with direct imaging detected exoplanets are shown in Figure 1.3.

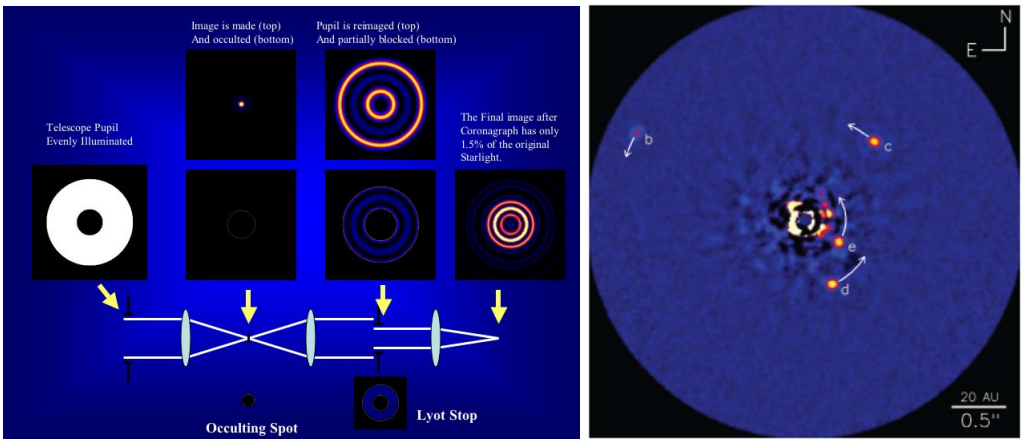

Figure 1.3: Schematic representation of a coronograph working principle (left) and a coronographic image of exoplanets detection (right, NRC-HIA/C. MAROIS/W. M. KECK OBSERVATORY).

Nulling interferometry is the working method of the HOSTS Survey from which we obtained the images used in this master thesis, this method we will thus discuss in more details in a dedicated section.

1.3 Exozodis

The zodiacal disk in our solar system is a disk of dust particles of size roughly ranging between 1 and 100 μm, contained in the zodiacal plan and concentrated between the asteroid belt (1.7 to 4.5 AU from the Sun) and the Sun. It is thus located near the terrestrial planets, and in particular the habitable zone of our Sun. This zodiacal disk is, after the Sun, the brightest object in the Solar system, outshining even Jupiter (Kelsall et al (1998)). Seen from the outside, the zodiacal disk can thus hide the planets to direct imaging detection methods.

When looking at the spectrum of the zodiacal disk, it is very similar to the Sun's one. This spectrum indicates thus mainly a reflection of the Sun light with little additional absorption due to the composition of the dust particles; and an excess in the infrared arising from the thermal emission of the particles heated by the Sun light. Another particularity of this disk is the movement of its particles toward the Sun due to the Poynting-Robertson(J.H.Poynting (1903), Robertson and Russell (1937)) effect and are thus absorbed by our star. However, even with this depletion the zodiacal disk maintains for a very long time implying a constant income of material. This material is though to be produced by the comets breakups and asteroids collisions which take place in this area (Reidemeister et al (2011),Wyatt (2005) and Nesvorný et al (2010)).

Comets and asteroids are very common objects which are expected to be present in every planetary system, thus zodiacal dust is also expected around a vast majority of stars. Depending on the income rate of comets and asteroids, and the efficiency of the Poynting-Robertson effect in the system a zodiacal disk such as our could appear.Those are called exozodiacal disks. If the presence of an exozodiacal disk is very likely around most of the stars it seems however really unlikely that they present the same density, location or extension than in our Solar system. But, as the zodiacal disk is the second brightest object in our Solar system, and thus outshining all the planets, we easily understand that detecting and characterizing those exozodiacal disks is of primary importance for the development of future direct imaging missions targeting planets in the habitable zones of their host star. Indeed some systems could have denser disks which could be unfriendly to terrestrial exoplanets detection whereas some other could possess thinner disks which

would constitute ideal targets. Characterizing the exozodiacal disks is thus very important for target selection. Furthermore constraining the probability to find an exozodiacal disk of a certain density in a system would greatly help in constraining the probability of exoplanet detection.

In addition, searching for, and characterizing, exozodiacal disks could already help in predicting the presence of planets. In particular, knowing the location and extension of those disks would allow to put constraint on the content of the systems thanks to models of disk evolution. Indeed planets would gravitationally interact with the disk, thus modifying its structure, but also with the comets and asteroids thus impacting the income of material inside the disks. Such constraint will give an insight on the system architecture thus further helping in the selection of the most promising targets but also in the unfriendly systems for planetary detection where thanks to models it would be possible to predict the presence of an exoplanet if needed to explain the behavior, the evolution of the location and extension of the exozodiacal disk.

The HOSTS Survey, that will be presented in the following section, studied those exozodiacal disks in preparation for several future exo-Earth imaging missions targeting the habitable zones such as : WFIRST Starshade Rendezvous (Green et al (2012)), HabEx (HabEx Team (2019)), LUVOIR 8m and LUVOIR 15m (LUVOIR Team (2019)).

1.4 HOSTS Survey

The Hunt for Observable Signatures of Terrestrial Systems (HOSTS, Ertel et al (2020)) survey was focused on the detection and characterization of exozodiacal disks around nearby stars. The survey was performed thanks to nulling interferometry on the LBTI (Hinz et al (2016)) in the N-band, more precisely at 11μm, with the NOMIC instrument. The goal of this survey was twofold: putting constraint on the dust content of nearby systems to estimate the feasibility of the missions but also to find correlations between the dust content of those systems and other physical parameters of the systems in order to find efficient selection criteria for the targets of those future missions.

During this survey, 38 stars were observed. They were chosen among the list proposed by Weinberger et al (2015) and constitute about half of this list of stars. The observed targets can be divided in two groups. The first one is composed of early-types stars (A to F5) for which the observation were more sensitive and the Sun-like stars (F6 to K8) which are the most promising targets for Exo-Earth imaging.

To analyze the data of this survey a reference zodi level was set at the dust level in our Solar System which would here correspond to 1 zodi. Three apertures were defined to estimate the zodi level of the systems: 143 mas, 233 mas and the EEID + 313 mas for the conservative aperture (EEID: Earth Equivalent Insolation Distance). A star was considered to have an excess if the ratio N^{as}/σ^{N} exceed 4 for at least one aperture, with N^{as} being the calibrated astrophysical null measurement and σ^{N} its measurement uncertainty. The absolute uncertainty medians range from 0.08% for the smaller aperture considered to 0.18% for the conservative one.

The analysis of the HOSTS survey data (Ertel et al (2020)) shows that the median zodi level might be below 27 zodis with a 95% of confidence. However it is expected to be much lower (below 9 zodis). According to those results the Solar System dust content might be consistent with being typical. It is thus likely that we could exclude a very pessimistic scenario where our Solar System would have been really poor in dust and thus that other systems would have contains amounts of dust prohibitively large for efficient detection in the habitable zones.

Thanks to those results the HOSTS survey have proved that the previously mentioned missions would be able to achieve their objectives for their median sample targets.

Beside those statistics on the dust content, the HOSTS data have been analyzed in order to find correlation between several parameters: spectral type of the star, age of the star and the presence of cold or hot dust. The only correlation which was found was with the presence of cold dust. Seven stars possessing a cold debris disk among nine show a significant excess against only 3 among 28

for the star without any detected cold dust. This might ruled out the stars with cold debris disk from the target selection for the future exo-Earth imaging missions. However, one should notice that 2 stars with cold debris disk do not show any excess. This is the case in particular of α Lyrae which will also be studied in this master thesis.

It should be mentioned that even if no correlation was found with other parameters that such correlation can have gone unnoticed due to the small number of stars observed during the survey. Indeed if the improvement of the LBTI sensitivity would help further constraining the feasibility of the different objectives of the future exo-Earth imaging missions, observing a larger sample of stars would greatly help in constraining the correlation of such exozodiacal disks with other stellar parameters or systems parameters.

During the survey 10 stars out of 38 have shown significant excess (all those stars have a ratio $N^{as}/\sigma^{N} > 5$ and/or have been detected at least twice in independent observations). Among those were α Lyrae and β Leo which will be studied in this master thesis. Indeed, we will try through different processing methods to detect the zodis of those two stars as well as to detect resolved emission around the stars.

Nulling Interferometry

In direct imaging two main kinds of techniques are nowadays available to suppress the stellar light: coronography and nulling interferometry. If coronography is currently the most widely-used technique, we will focus here on nulling interferometry which was used to produce the images used in this master thesis.

In nulling interferometry we do not use a mask and a Lyot stop to block the star light but take advantages of undulatory properties of light. Indeed, as angular separation is a major issue in direct imaging, using interferometry already provides great advantages. The interferometry technique allows to combine the light of two telescopes in order to mimic the angular resolution of a single telescope with a diameter equal to the baseline length of the two, real, telescopes. We show below a schematic representation of an interferometer.

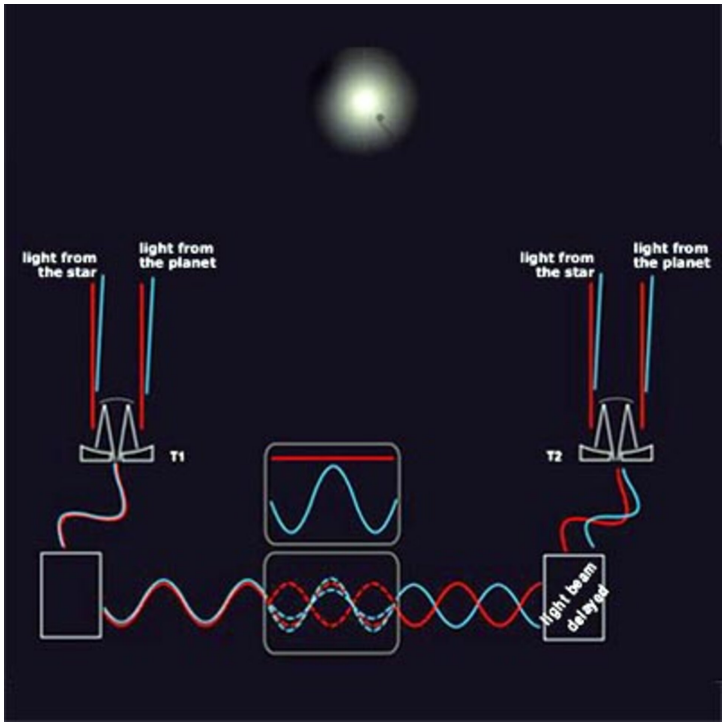

Figure 2.1: Schematic representation of a nuller working principle. The light from the star is at the center of the field of view of the two telescopes thus interfere destructively. However the light from the planet is off-axis and thus can, passing through the same delay line, interfere constructively (see also Figure 2.2).

As we can see on Figure 2.1 light enters the optical system through two different apertures and then follows two different paths. Indeed in Figure 2.1, one sees on the right telescope a block which delays the line compared to the path followed by light entering the left telescope, before the two paths finally converge to combine the light. This block is called the delay line. The delay line allows to compensate the optical path difference between the two telescopes to coherently combine

the two beams in time. Indeed the strength of the interferometry technique is to allow the beams to constructively interfere thus providing better angular resolution and sensitivity than the simple sum of the images of each telescopes would provide. It is important to note, as the light travels through different paths to reach the telescopes, that the wavefronts are different for each telescope. However as we want to make the two beams constructively interfere, we want those wavefronts as similar as possible. We therefore understand how important adaptive optics will be in interferometry, in particular in the search for very faint signals. In the case of the LBTI, the two telescopes have a 8.4m aperture and both possess secondary deformable mirrors which are controlled thanks to 672 actuators, for each, which are able to correct 500 Zernike modes. This allows very high Strehl ratio, in particular at the wavelength we are using in this master thesis (11μm), where it can reach 99%.

The LBTI has a nuller mode which allows to image the stars with the nulling interferometry technique. This technique, as mentioned above, relies on the properties of interferometry itself. Indeed in standard interferometry the beams constructively interfere thanks to the delay line which sets the phase between those two beams at $0[2\pi]$. However, it is possible to use the delay line not to get a 0 phase between the two wavefronts but on the opposite a π phase thus making the beams destructively interfere. It is this particular propriety which is used in nulling interferometry.

The basic idea of nulling interferometry, first proposed by Bracewell (1978), is to make the star light destructively interferes while get the other fainter planetary signals to constructively interfere. This principle is illustrated in Figure 2.2.

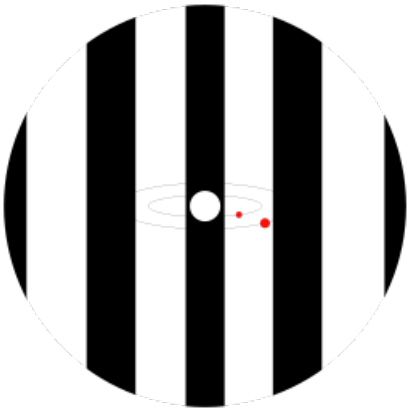

Figure 2.2: Schematic representation of the monochromatic nulling interferometric pattern. An interference pattern is created so that the star light interfere destructively.

However this pattern does not stay fixed in time, with respect to the sky, as the images are most often taken in pupil tracking mode (it is also the case of the images used in this master thesis). The interference pattern will thus rotates with the images and, if the star light would in a perfect case always been self-subtracted, the faint planetary signal could however go in and out of the dark fringes, meaning than for some images the planet signal will also destructively interfere. Nonetheless, as the star light is always suppressed, it will allow to bring fainter signals to detectable levels.

In the case of the LBTI the two telescopes are mounted on the same mount presenting a baseline much shorter than usual interferometers but presenting the advantage not to require long delay lines. Instead of those they use a fast pathlength corrector (FPC) and a slow pathlength corrector (SPC). The SPC is used to create the interference fringes while the FPC provides correction for the fast pathlength variations. A schematic view of the LBTI nuller mode (Defrère et al (2016)) is shown in Figure 2.3.

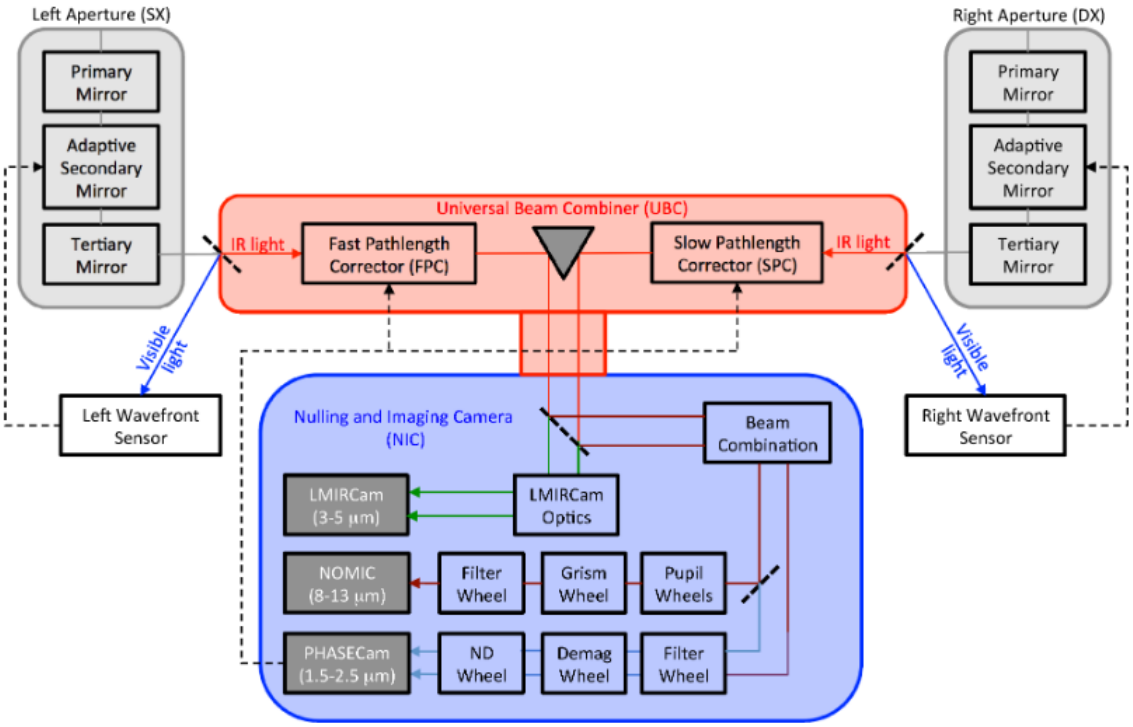

Figure 2.3: Schematic representation of the LBTI's nuller mode (Defrère et al.2020).

The light enters the two telescope apertures and reflects on the different mirrors before to be split into the IR scientific light and the visible light which is used for the adaptive optics system of the LBTI which controls the deformation of the secondary mirror to correct the entering wavefront. The IR light however enters the Universal Beam Combiner (UBC) which allows first to correct the delay between both wavefront so they are in time coherence thanks to the FPC and the SPC. The light is then send to the Nulling and Imaging Camera (NIC) where the beams are once again split into the 3 to 5μm waveband light which enters the LMIRCam optics and then goes to the LMIRCam detector and the rest of the IR light. This last one enters a Beam Combiner which sends a part of the light directly to PHASECam and the other part to NOMIC. The light going to NOMIC undergoes another splitting and the 1.5 to 2.5μm light is redirected to PHASECam. In this master thesis we used images taken at a wavelength of 11μm which corresponds to the wavelength of NOMIC.

The images produced by nulling interferometry could be very surprising at first glance as the best of them do not show the star at all. We show in Figure 2.4 several unprocessed images obtained by nulling interferometry with different nulling qualities.

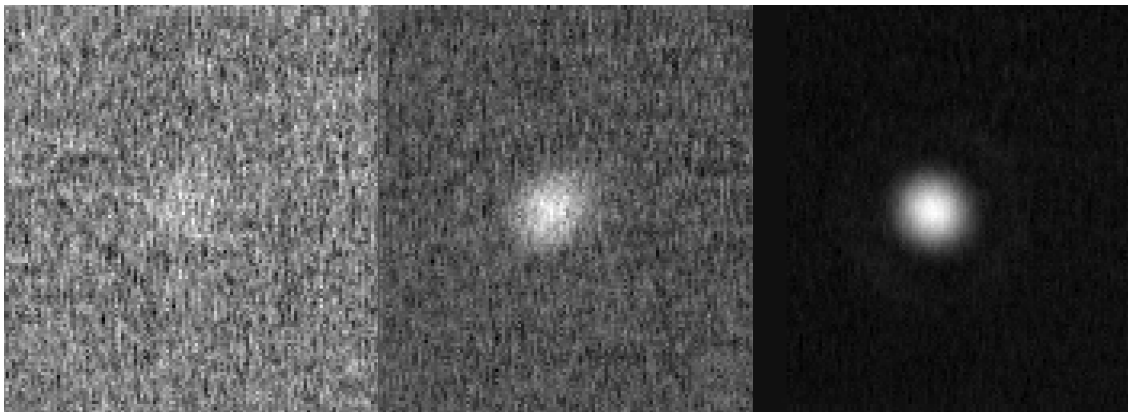

Figure 2.4: Different image qualities for nulling interferometry: very good null quality (10 099 ADU or 1.63% null leak threshold, left), mediocre null quality (20 665 ADU or 3.33% null leak threshold, middle) and very bad null quality (174 397 ADU or 28.15% null leak threshold, right).

As we can see on this trio of images, the star is hardly distinguishable on the best of them whereas on the worse we can even see the Airy rings. Indeed as we want to get rid of the star light the left images is the best suited as very little light from the star remains and much fainter signals would became detectable. For this reason it can be very interesting to select the images in order to discard the ones of poor quality. If we are very selective we can even discard the images similar to the middle one but this can lead to a very small number of kept frames. The selection operated on the null qualities is described in further details in the following section.

If we now want to go in deeper details for the construction of those images one might introduce the monochromatic single-aperture PSF and transmission map of the LBTI. Figure 2.5 (Defrère et al (2016)) shows those two.

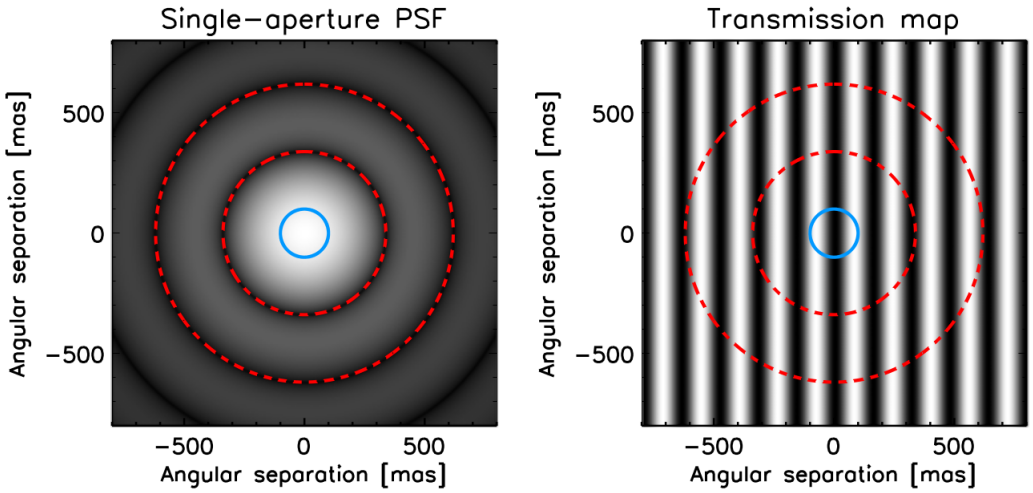

Figure 2.5: Monochromatic single-aperture PSF (left) and transmission map (right) of the LBTI. The red dashed lines correspond to the two first Airy minima of the PSF and the solid blue line to the Earth orbit. The size of the figures are 1.5 x 1.5 arcsec and have been computed for 11.1 μm.

As we can see the images are built with several fringes and interfringes. We want to determine the null depth for the images and for this we have to express the flux measurement at null (dark fringes) and the constructive flux (bright fringes). The following equations are directly taken from Defrère et al (2016). and express the flux in each case. The constructive flux I_+ is given by:

$$I_+ = I_1 + I_2 + 2\sqrt{I_1 I_2}$$

where I_1 and I_2 are the mean individual intensities. The instantaneous flux sequence I_(t) giving by the following expression:

$$\mathrm{I\_(t)} = \mathrm{I_1(t)} + \mathrm{I_2(t)} + 2|\mathrm{V}|\sqrt{I_1(t)I_2(t)}\,\cos(\Delta\ \phi(\mathrm{t}))+ \mathrm{B(t)}$$

with $\mathrm{I_1(t)}$ and $\mathrm{I_2(t)}$ the individual instantaneous photometries, $|\mathrm{V}|$ the absolute value of the source visibility at the instrument baseline, $\Delta\ \phi(\mathrm{t})$ the instantaneous phase between the two mirrors and B(t) the instantaneous measured background. The null depth is expressed as the ratio of the instantaneously measured flux at null and the constructive flux:

$$\text{Null Depth} = \frac{I\_(t)}{I_+}$$

In the following we will use a threshold on the null depth in order to select the best frames. This threshold is defined by the ratio between the maximum flux (computed in a central aperture of the size of the full-width-at-half-maximum (fwhm) of the LBTI's PSF - 17.98 pixels -) in the PSF for a frame to be selected $\mathrm{I_{max}}$ and the constructive flux. If $\mathrm{I\_(t)} < \mathrm{I_{max}}$ the frame is kept and the null leak threshold is thus define as:

$$\mathrm{L} = \frac{I_{\mathrm{max}}}{I_+}$$

and expressed in percent.

Data description

3.1 Data acquisition

The images used in this master thesis were obtained with the LBTI in nulling mode at 11μm during the HOST survey. The frames are composed of 128x128 pixels of 17.85μm. The data acquisition sequence is described in details inDefrère et al (2016) and we remind here the basic principles. Those images were taken following a sequence of observing blocks (OB) composed of: several OBs at null, one OB of photometric measurement and one OB of background measurement. The OBs at null are the images which will after data reduction compose the cubes, they correspond to images where the beams of the two telescopes overlap coherently in phase opposition thus greatly reducing the amount of star light in the final image. The OBs at null alternate different nod positions every few minutes at most. The OB of photometric measurement, after data reduction, allows to retrieve the star photometry needed to build the contrast curves. It consists in images where the beams of the two telescopes are separated and do not overlap. Finally the OB of background measurement allows to reduce the images mentioned above. It consists of images where the beams are nodded off the detector.

Before data reduction the frames with the same nod position are grouped in a single data cube. Then a mean image of the adjacent OB is build and subtracted to every frame of the data cubes. In the case of β Leo a median image of the adjacent OB was also build and subtracted to each frames of the data cubes and of the photometric measurement OB instead of the mean image. In the following we will designate those two different cubes by the Mean cube and the Median cube respectively. For all the other stars observed during the HOSTS survey only the Mean background subtraction was processed.

During the survey calibrator stars were observed along with the scientific targets following the sequence: CAL1-SCI-CAL2-SCI-CAL1-SCI-CAL3. Calibrators were observed to determine the instrumental null leak i.e to determine the nulling transfer function of the instrument and its response to a point source. Determining the instrumental null leak allows then to compute the astrophysical null (difference between the total null leak and the instrumental null leak) which finally gives the source flux transmitted through the instrument. The images used for this study were taken during three nights 2015-02-08, 2017-04-06 and 2018-03-28, with both scientific targets and calibrators. The stars observed during those nights are listed in Table 3.1 with their coordinates, spectral types, photometry, number of images, the exposure time of each images and for the calibrators the scientific stars they are dedicated to.

Target	frames number	right ascension	declination	spectral type	magnitude (V band)	exposure time (ms)	scientific target
α Lyrae	47005	18 36 56.336	+38 47 01.280	A0V	0.03	45	
β Leo	16599	11 49 03.578	+14 34 19.409	A3V	2.13	60	
HD114326	11592	13 09 47.847	+16 50 54.996	K4III	5.87	45	τ Boo
HD168775	11237	18 19 51.709	+36 03 52.369	K2III	4.34	45	α Lyrae
HD177808	13154	19 04 57.874	+31 44 38.653	M0III	5.56	45	α Lyrae
HD126597	12308	14 25 29.151	+38 23 34.990	K2III	6.28	45	gam Ser
HD129972	11889	14 45 14.460	+16 57 51.407	G8.5III	4.60	45	gam Ser
HD142574	16317	15 54 34.612	+20 18 39.491	K8III	5.44	45	gam Ser
HD149009	11926	16 31 13.431	+22 11 43.644	K5III	5.75	45	gam Ser
HD163770	7885	17 56 15.870	-58 42 15.461	F2V	9.90	45	α Lyrae
HD164646	11790	17 59 56.206	+45 30 04.954	M0III	5.67	45	α Lyrae
HD104979	7980	12 05 12.540	+08 43 58.749	G8III	4.12	60	β Leo
HD108381	7968	12 26 56.272	+28 16 06.320	K1III	4.34	60	β Leo
HD109792	16767	12 36 58.332	+17 05 22.326	K4III	5.66	60	β Leo

Table 3.1: List of the scientific stars and calibrators with their number of frames, their coordinates, spectral types, magnitude in the V-band and the associated scientific target for the calibrators.

The scientific stars data are described in further details in the following sections.

3.2 Image cubes and frame selection

3.2.1 α Lyrae

α Lyrae was observed twice during the HOSTS survey. A first image cube was taken during the night 2017-04-06 with an exposure time of 45 ms and a total of 23281 images. A second was obtained during the night 2018-03-28 with the same exposure time but this time for 23724 images in total. All the images of α Lyrae were corrected with the mean subtraction background. The results of the HOSTS survey for α Lyrae show a low zodi level (33.2 $\pm$ 7.5 zodis, Ertel et al (2020)). We proceed to a first study on the 2018's cube and then a second one on the merged cube. It is important to note that it was necessary to build two merged cube: a first one with a configuration 2017-2018 and another one with the inverse configuration (2018-2017). We will in the following designate this last one as the inversed merged cube. We plotted in Figure 3.1 the parallactic angles as a function of the frames when the configuration 2017-2018 is used, to show their discontinuity.

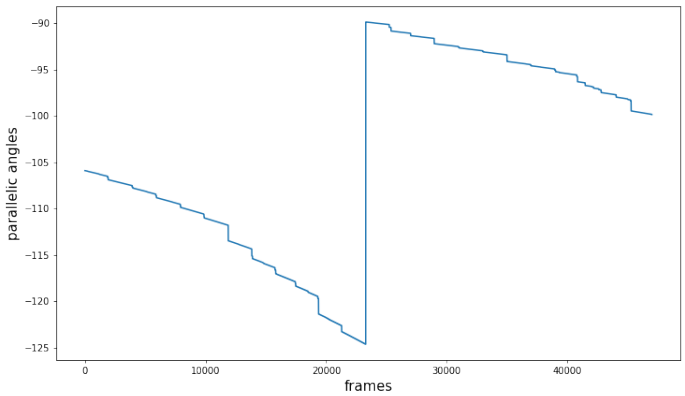

Figure 3.1: parallactic angles for the α Lyrae merged cube 2017-2018

We represented in Figure 3.2 the flux as a function of time, the parallactic angles as a function of time as well as the flux distribution for both cubes.

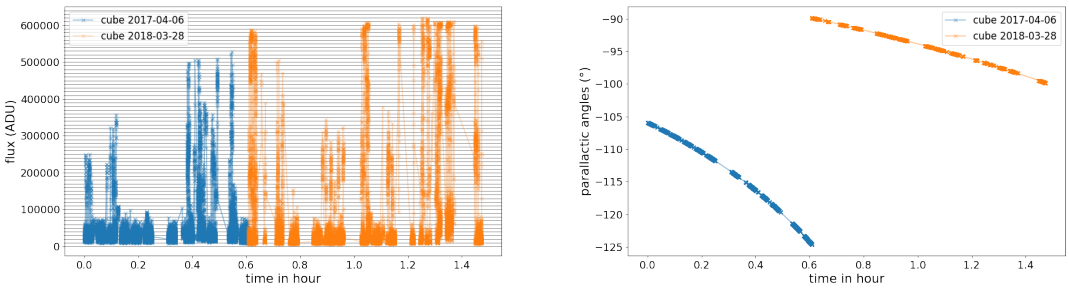

Figure 3.2: Flux (left) and parallactic angles (right) as a function of time for both image cubes. For the flux as a function of time we make coincide the time of the last image of the 2017's cube with the first image of the 2018's cube for better visibility.

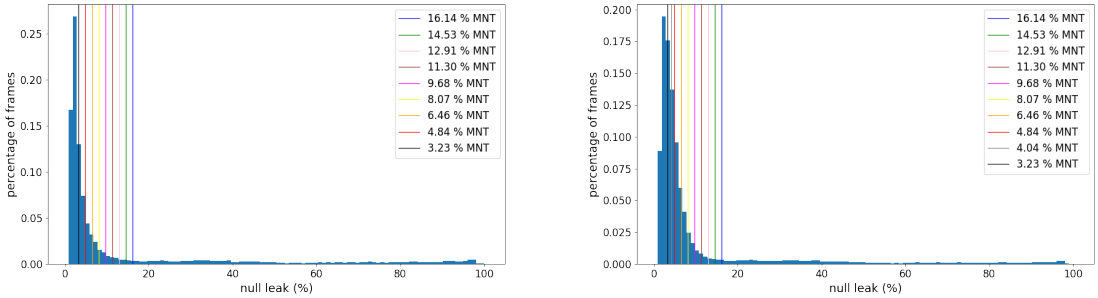

Figure 3.3: Flux distribution for the 2018's cube (left) and for the merged cube (right). The maximum flux (constructive interference) is about 619585 ADU for α Lyrae. The vertical line represents the selection operated on the null.

All this information allows us to make selections on the flux, knowing the loss on parallactic angles and number of frames such a selection will introduce. On this basis we built 9 other cubes for the 2018's original cube, and 10 for the original merged cube. The selection was first operated on the cube only containing the images from the night 2018-03-28.

We found that a first interesting selection would be to discard all frames with a flux greater than 100 000 ADU, thus corresponding to a 16.14% maximum null leak threshold (MNT) selection. We choose this first selection because it discards all the images with very bad nulling while keeping a great number of frames (18942 frames for the 2018's cube). A second selection was put at 40 000 ADU, corresponding to a 6.46% null leak threshold. This second selection was chosen in order to keep images with much greater null quality while keeping 17357 images. We then choose two selections at 30 000 and 20 000 ADU to study the effect of an important loss in the number of frames against the gain due to the quality of the preserved frames. We did not make more selective cubes due to the very small number of frames that would have been kept. However, to further estimate the effect of the gain and loss tied to the number of frames and null quality, we choose to build cubes with selection set at 50 000, 60 000, 70 000, 80 000 and 90 000 ADU which correspond to 8.07, 9.68, 11.30, 12.91 and 14.53% null leak threshold respectively. These cubes offer a constant improvement of the null quality, however, the diminution of the number of frames is not constant at all. This will allow us to estimate the effect of both parameters independently.

For the merged cube we choose the same selections than for the 2018's cube in order to compare the results obtained for the same null leak threshold but with a greater number of images and a wider range of parallactic angles. We add another cube with a selection on the flux set at 25 000

in order to get approximately the same number of frames than the original 2018's cube, but with a lower null leak threshold and a wider range of parallactic angles.

The cubes with selection on the flux, for both of the original cubes (2018, merged, inversed merged) will be called when referred as a whole, and not individually, as the "cleaned cubes" which would be opposed to the original cubes.

In order to assess the coherence of our results at different distances from the star we also checked the cropping of the images. We found that no result further than 0.81 arcsec away from the star should be considered.

Finally, to save computational time, all the cubes (cleaned and originals) were averaged 100 frames by 100. All the cubes presented in the following analysis are the averaged ones. A verification has of course been made to check if this average does not degrade the quality of the final curves we obtain, and no significant change have been found.

3.2.2 β Leo

β Leo was observed during the commissioning time of the HOSTS survey and was added to the unbiased survey as it does not introduce significant bias. A cube of 16599 images with 60ms of exposure time was produced with this observation, and later on added to the complete survey. These images were then corrected by two different background subtraction methods: the mean and the median.The Mean and Median images taken for the background subtraction are the Mean and Median images of the adjacent OB. Those images are then subtracted to each frame of the cubes. When subtracted with the Mean image the frames formed what we called in the following the Mean cube, when subtracted with the Median image they formed the Median cube. For the Mean subtraction methods the number of frames reduced at 16597. β Leo, on the contrary to α Lyrae present in the data of the HOSTS survey a significant excess for its zodi level (103.5 $\pm$ 11 zodis, Ertel et al (2020)) suggesting this time that its exozodiacal disk might be much denser than the one in our solar system thus dampening the chances for exoplanets detection inside or near this disk.

In Figure 3.4 and Figure 3.5 we plotted the flux in function of time, the parallactic angles in function of time and their flux distribution. Even if a single cube was taken in the 2015-02-08 night, we processed the two cubes resulting in the two different correction as independent. However as they are very similar and that their differences are not distinguishable on the graphs presented in Figure 3.4 we chose to display only the Mean cube.

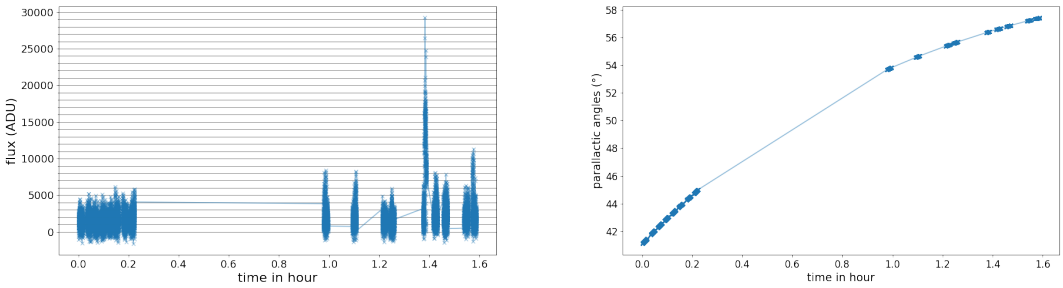

Figure 3.4: Flux (right) and parallactic angles (left) as a function of time. For the flux the two cubes present slight differences and have been plot side by side by adding the time of the last frame of the Mean cube to the first of the Median cube. For parallactic angles we choose to plot only one of the cube as there is only two additional frame between the Mean and Median cubes and no changes in parallactic angles besides those two frames.

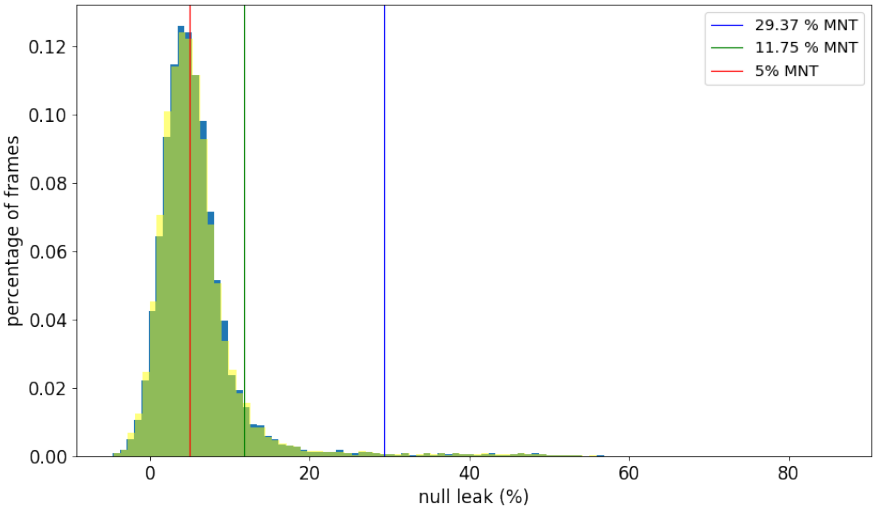

Figure 3.5: Flux distribution for the Mean cube (blue) and the Median cube (yellow) with the selections operated on the null

As we can see on Figure 3.5 the differences between them are tiny but still present. The null quality of the Mean cube is indeed slightly better than the Median one. For the two 100% null leak threshold cubes this induce nearly no difference. There is, however, slightly more frames in the selective Mean cubes thus inducing stronger differences. By looking at the corresponding graphs for α Lyrae, even taking the much greater value of the photometry into account, we can see that the null work a lot better on β Leo (see comparison with Figure 3.3). Indeed if some few images reach a flux value of 29 000 almost all the others (16349) are below 10000, which correspond to 29.37% of null leak threshold. This first selection allow us to discard the images which forms the peak that we can see in the Figure 4.2.1(left) while keeping nearly all the frames. We made a second selection on the flux at 4000 ADU as it drastically increases the quality of the null of the kept frames while keeping a good integration time (15 minutes). This selection corresponds to a 11,75% null leak threshold. A last cleaned cube was made at 5% null leak threshold to study the impact of a great loss in integration time and an important gain in the null quality.

As for α Lyrae we check the cropping to estimate until which distance the analyse of our images can still be consider coherent. It happens to be much more limited than in the α Lyrae case as the maximum coherent distance is here 0.62 arcsec.The β Leo's cubes were also averaged 100 frames by 100 to save computational time. Once again, we check that it does not degrade the quality of the contrast curves, but no significant changes were found.

Data Processing

4.1 VIP

In the context of this master thesis we processed the images using the Vortex Image Processing (VIP) package which is presented in details in Gonzalez et al (2017). This package is a python library which has been designed for the processing of high contrast imaging data, in particular taken with the ADI technique as it is nowadays the most commonly used. It also supports the RDI and SDI (multi-spectral differential imaging) techniques. If this library has been developed at first for coronography, thanks to its instrument-agnostic design, it is also very well adapted for images obtained with nulling interferometry data. The modular structure of VIP is indeed very practical as it allows to choose the needed functions to process our data but do not force them into our pipeline. For nulling interferometry, as an example, the re-centering process is not adapted, nor needed, and the flexibility of VIP allows a very fast adjustment to new instruments. A very easy-to-use tutorial for ADI is also provided through this package and has proven to be very useful for this master thesis.

The VIP library proposes a large choice of PSF model subtraction methods with different complexity of PSF building : median subtraction, median annular subtraction, pairwise frame differencing, least-square approximation, full-frame PCA, annular PCA, non-negative matrix factorization for ADI (NMF-ADI) and LLSG. These methods will be describe very briefly in the following. They can be used all in the same pipeline (as shown in the tutorial) to allow easy comparisons of the obtained final images, but also individually thanks to the flexibility of the VIP library. VIP also offers a very practical way to adapt the code from an ADI analysis to an RDI or SDI analysis as the function only needs additional parameters, among which the image cube of the reference star, to switch to those modes. Beyond practicality it also allows not to introduce additional biases in potential comparison of those different techniques. However, for the RDI mode, fewer PSF model subtraction technique are available will only the full-frame PCA and the annular PCA.

We very briefly describe the PSF subtraction methods proposed by VIP below. These descriptions are directly taken from the VIP website[1].

Median and Median annular subtraction

This algorithm is based on Marois et al (2006) and consists in taking the median of the image before its derotation and to subtract it to each frame of the image cubes. Then the derotation is operated on each frame and the frames are combined. In the case of the Median annular subtraction the median of the images cubes is operated annulus per annulus and so is the subtraction. This modification of the first algorithm allows to adapt the subtraction in function of the distance from the star.

Pairwise frame differencing

This algorithm uses separately the pixels from different annuli (which width is determine) to create pairs of most similar images. Then it performs pairwise subtraction and combine the residuals.

[1] https://vip.readthedocs.io/en/latest/vip$_h$*ci.pca.html*

Least-square approximation

Least-square approximation algorithm is based on the Locally Optimized Combination of Images algorithm (Lafreniere et al (2007)). It models a PSF with least-square combination of neighbouring frames (solving the equation ax = b by computing a vector x of coefficients that maximizes the Euclidian 2-norm $||b\text{-}ax||^2$).

Full frame PCA

The algorithm allows to model a reference PSF and a quasi-static speckles pattern thanks to Principal Component Analysis. This algorithm can work with ADI and RDI. In the case of ADI processing the images from the target cube itself are used to build the PSF and the quasi-static speckles pattern. It is based on Soummer et al (2012) and Amara and Quanz (2012). When used for RDI processing, a reference star image cube must be introduced in the function so the PSF and the quasi-static speckles pattern can be build from it.

Annular PCA

This algorithm is very similar to the previous one, and work also with ADI and RDI. However, in this case the PCA model is computed locally in each annulus. For each sector reference frames are discard taking into account a parallactic angles threshold and a radial movement threshold (those parameters are applied to the target image cube in the case of ADI and to the reference star image cube in the case of RDI)

Negative Matrix Factorization for ADI

Negative Matrix Factorization proposes an alternative to the full-frame PCA processing. Indeed, it does not rely on single value decomposition or eigenvalue decomposition, for obtaining low-rank approximation, as does full-frame PCA. This function embeds the scikit-learn Negative Matrix Factorization algorithm solved through coordinate descent method.

Local Low-rank Sparse Gaussian

Local Low-rank plus Sparse plus Gaussian decomposition method is described in details in Gomez Gonzalez et al (2016). It aims at decomposing ADI cube into three terms L (Low-rank) + S (Sparse) + G (Gaussian). As the moving planet should stay in the S term, separating the noise from the Sparse component allows to increase the S/N of potential planets.

4.2 No PSF subtraction

We began our analysis with a simple processing involving no PSF subtraction. We indeed simply derotated the images and then took the mean of this cube to build a Mean derotated image or its median to build a Median derotated image. This technique was performed with the original cubes and the cleaned cubes of both stars. For this analysis we slightly modified pre-existing VIP algorithms to compute the contrast curves. In particular, as this technique does not involve any subtraction we set the throughput to 1. It is important to note that for the Mean derotated images the cube were averaged 100 by 100 but for the Median derotated images we took the median of 100 by 100 images. This was done in order not to give an important impact of the averaging of the cubes in our comparison between the Mean and Median derotated images.

After this first analysis we tried to improve the obtained contrast curves by using more complex processing technique: ADI and RDI, which are described in the following sections.

4.3 ADI

The angular differential imaging (ADI) technique has first been described in Marois et al (2006). It refers in fact to on observational technique as well as a reference PSF subtraction technique.The observational ADI technique consists in allowing the field of view (FOV) to rotate while keeping the star at the center. This is shown in Figure 4.1.

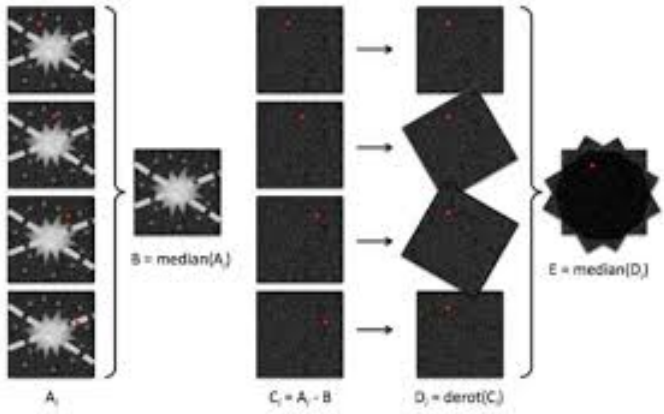

Figure 4.1: Schematic representation of ADI working principle. The FOV rotates around the star, then the median of the images is computed. This median is then subtracted to each frame. After this subtraction the images are derotated. A median of those new (subtracted + derotated) images is computed, this is the final image. It is important to note that the images subtracted are not always the median. The least-square approximation, FFPCA, annular PCA, NMF-ADI and LLSG methods do not subtracted the median but images build from more complex algorithms.

By this process the star light remains at the same location on the detector whereas the light coming from a potential off-axis companion will rotate with the FOV. When the images are combined but not derotated the star light will be summed up but the planet's light remains dispersed. The ADI technique uses this configuration to build a reference PSF based on those images and thus uses directly the light of the target star. Of course they are several algorithms to build the reference PSF from those images. In Marois et al (2006) they present the median subtraction and the median annular subtraction. However since then other algorithms have been developed for this method, in particular the full-frame PCA algorithm (Hunziker et al (2018)) which has proven to be very efficient and is commonly used nowadays. The development of this technique as greatly improved the contrast reachable for point-like sources compared to previous classical observation technique.

However this technique also has drawbacks. The first of them might be that it can only be used with altitude/azimute telescopes as this configuration is required to allow the FOV to rotate around the target star. Another drawback of this technique is the self-subtraction it induces for extended circular structure such as proto-planetary disks. Indeed with a centered circular configuration this light will self-subtract in the same way than the star light. Finally, to be efficient at small angular separation, this technique requires very wide range of parallactic angles which can prove to be time consuming and thus decreases the efficiency of the ADI technique. Indeed its main purpose is to considerably reduce the quasi-static speckles noise and other a long time scale (typically above an hour) the light distribution might change sufficiently to reduce ADI performances.

This technique has been developed for coronography, however it is also very well adapted to our nulling imaging data. Indeed an additional effect of this observation technique when used with nulling interferometry is that the interference pattern will not be fixed compared to the image. If we consider the situation in the frame of reference of the images, the interference pattern is rotating, thus the planets might go in and out of the dark fringes. It thus prevent the potential planets to be permanently hidden by a dark fringe during the whole observation. Figure 4.2 illustrates this idea.

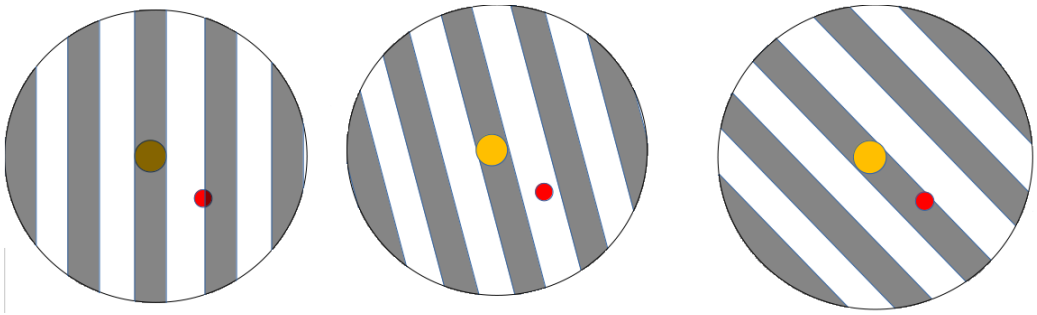

Figure 4.2: Rotation of the interference pattern compared to the star and its companion

The ADI technique is thus really important in the case of nulling interferometry as it allows to suppress blind zones due to the interference pattern. However, it does not mean that data taken with the ADI observational technique have to be processed thanks to ADI PSF subtraction methods.

In this master thesis the images have been taken in pupil-tracking mode, which is well suited for ADI processing. When we refer to the ADI processing we, however, are considering the PSF subtraction methods for ADI and not the observational technique.

4.4 RDI

The Reference star Differencial Imaging (RDI, Lafreniere et al (2007), Ruane et al (2019)) technique has been developed to overcome some of the drawbacks of ADI. The main motivation was to increase the sensitivity close to the star where ADI was limited by its need of wide parallactic angles range. RDI also allows to overcome the circumstellar disk self-subtraction issue and can be used with all kind of telescopes. Its basic principle is to use a reference star from which the reference PSF for the target star treatment will be build. With this technique there is no need to rotate the FOV but it requires observational time for the calibrators (reference stars). This technique thus does not require a particular observation technique as ADI. The huge advantage of RDI over ADI at small angular separation is that it is not limited by parallactic angles range, thus it allows to probe the environment closer to the star.

In the case of RDI, however, the reference PSF is not build from the target star's images themselves but from the calibrator's (or reference star) images. While it does not require any rotation it can however introduce differences in the reference PSF which come directly from the fact that no stars are perfectly identical or acquired in the same conditions. It also means different wavefront errors, different background, but for some case also different seeing quality, etc... The overall effect is that if RDI is, indeed, more efficient close to the star, ADI remains better further from it. Those methods thus tend to be complementary.

Another interesting characteristic of this method is that it can be used on all type of images. Indeed RDI reference PSF subtraction methods can be used on images taken with ADI but the opposite is not true as ADI needs a parallactic angles range to operate and RDI observations would not have such a range. For SDI (Multi-spectral Differential Imaging), RDI could also be used in theory as it needs nothing more than images from the target star and from a calibrator.

An important point to take into account here is that the images used for this master thesis were taken following the ADI observation technique, even if calibrators were also observed. Indeed, when working with nulling interferometry a fixed pattern would be very unefficient and as mentioned previously, the ADI technique is a good way to overcome this issue. It is thus important to remember that the images are only processed thanks to RDI but have been taken with the ADI technique. It might thus induce, even in the RDI processing, some sensibilities due to the observational technique.

Data Analysis

5.1 No PSF subtraction

5.1.1 α Lyrae

The analysis without PSF subtraction for α Lyrae was directly made on the merged cube as we strongly suspected than more integration time would favor this method. As described earlier we derotated the images before to build the Mean and the Median derotated images. We obtained two very similar images which are shown in Figure 5.1.

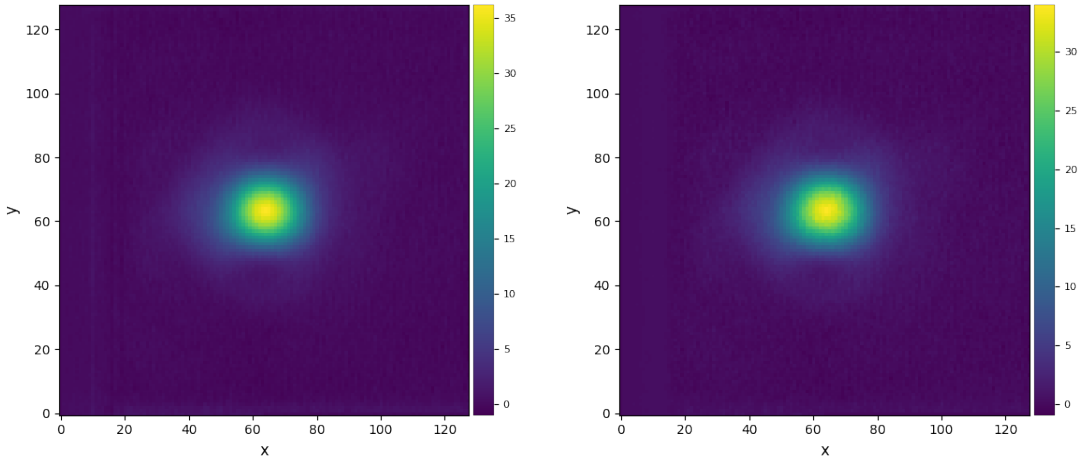

Figure 5.1: Mean (left) and Median (right) derotated images for the 3.23% null leak threshold merged cube.

As we can see in both the images we can guess a ring around the star. In Figure 5.2 we put a mask of 17 pixels radius (for a full-width-at-half-maximum -FWHM- of 17.98) over the center of the frame to better show this ring. This was done on the Mean derotated image but a very similar result is obtained for the Median derotated image.

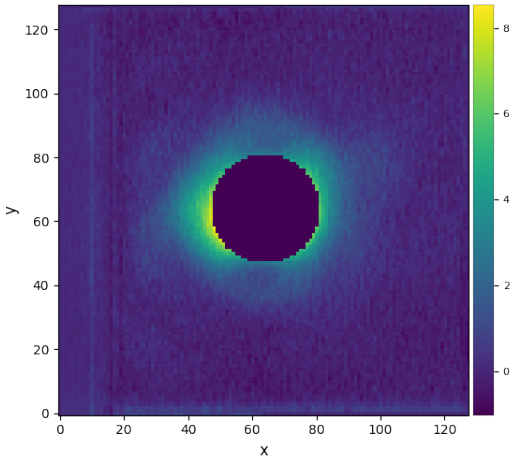

Figure 5.2: Mean derotated image with a central mask of 17 pixels radius.

We then compute the contrast curves for those two images, for different MNT levels. These results are shown in Figure 5.3 .

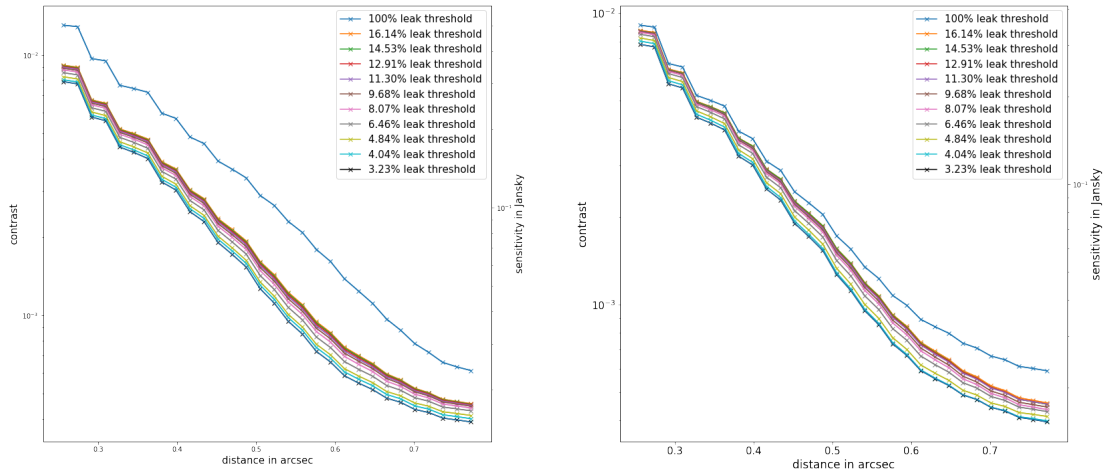

Figure 5.3: Contrast curve for the Mean (left) and Median (right) derotated images of merged cubes without subtraction.

As we can see here the more selective cubes always give better results, suggesting a great importance of the selection on the flux. Indeed as there is no PSF subtraction, it is of first importance to discard the bad frames. It would be very interesting to investigate until which point the selection improves the contrast reachable and thus when the lack of integration time begin to overcome the improvement brought by the flux selection. Another interesting behavior to notice is the one of the cubes with no selection. In Figure 5.3, for the left part (Mean derotated image) we notice that the 100% null leak threshold cube is much worse than the other whereas on the right part (Median derotated image) it is much closer to the other contrast curves but for the very external part. This can be explained by the nature of the mean and the median techniques themselves but one should thus carefully consider which image (Mean or Median) will be more adapted in function of the overall null quality of the cubes. Indeed if the cube contains a lot of relatively poor null and that no selection is operated the median is probably more adapted. On the contrary if the cube has

very little poor null or that a selection has been made, the Median derotated image tends to be slightly better close to the star, whereas the Mean gives slightly better results far from the star. However, if an aggressive selection has been made and that only very good frame are preserved, the Mean derotated image might prove to be the best choice.

5.1.2 β Leo

We proceed to the same analysis on the β Leo Mean and Median cubes, for which we build a Mean and a Median derotated image. As for α Lyrae the Mean and Median derotated images are very similar but so are the Mean and Median derotated images of the Mean and Median cubes. We thus chose to display only one of them in Figure 5.4.

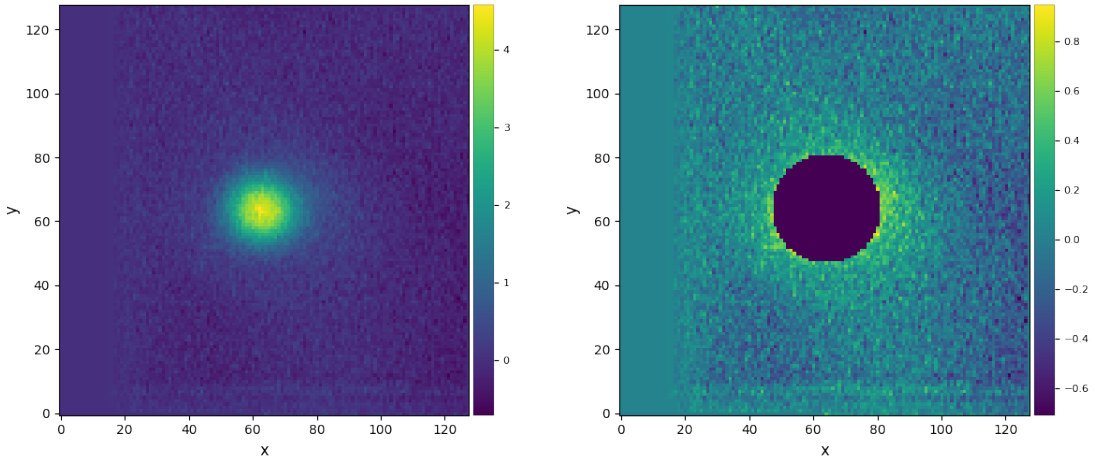

Figure 5.4: Mean derotated image of the 11.75% null leak threshold Mean cube with (right) and without (left) a mask of 17 pixels in radius.

Contrast curves were nonetheless compute for the four derotated images (mean image for the mean background subtracted cube, median image for the same cube, mean image for the median background subtracted cube and median for this last cube) and are display in Figure 5.5.

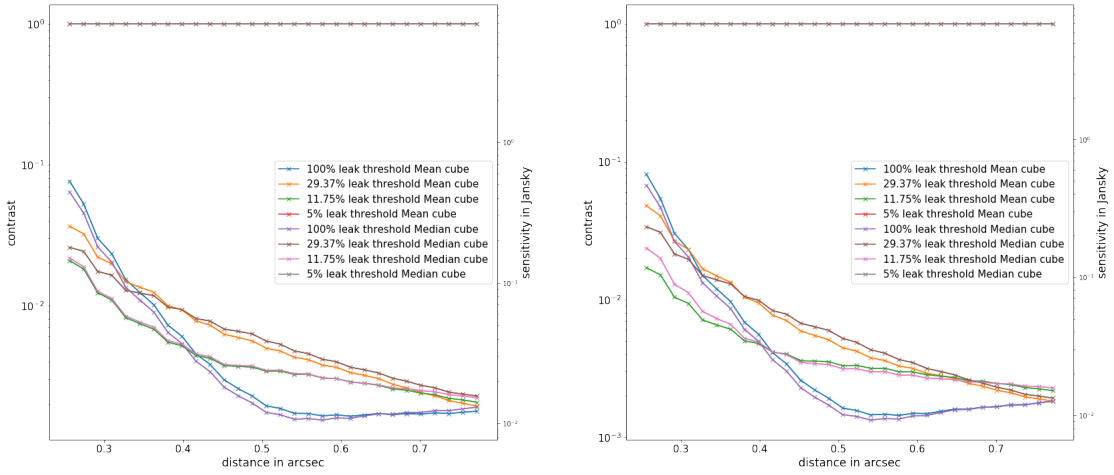

Figure 5.5: Contrast curves for the Mean (left) and Median (right) derotated images.

As we can see on those graphs in both case the 11.75% null leak threshold Mean cube gives the best results close to the star and the 100% null leak threshold Median cube become better further away from the star. This would suggest that for this method Mean background subtraction is more efficient close to the star and Median background subtraction far from it. Another interesting result is that the Median derotated image gives better results for those two curves which tends to indicate that the Median derotated image is more adapted to β Leo cubes configuration. Further comparison between β Leo and α Lyrae will be detailed in a dedicated section.

5.2 ADI processing

5.2.1 α Lyrae

After the first processing without PSF subtraction, presented in the previous section, a more complex analysis is made, on α Lyrae, using the ADI technique. The VIP package we use to process the images proposes a large panel of PSF subtraction methods for ADI: median subtraction, median annular subtraction, pairwise frame differencing, least-square approximation, full-frame PCA (FF-PCA), annular PCA, ADI-NMF and LLSG. We first compare the throughput obtained with each method on each merged cube (cleaned and the original). This is shown in Figure 5.6. The same comparison was also made on the 2018's cubes and displays similar results. It is useful to note that the methods median annular subtraction, pairwise frame differencing, least-square approximation and annular PCA were performed on the inversed merged cube because these methods were not working with the discontinuity in parallactic angles present in the merged cube.

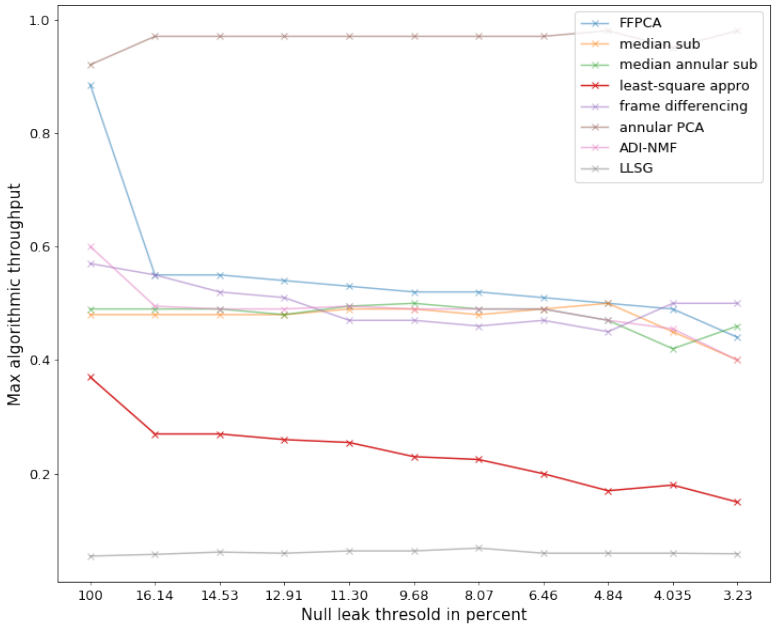

Figure 5.6: Maximum algorithmic throughput for each merged cube and each method

As we can see in Figure 5.6 the annular PCA and FFPCA methods are the most promising in term of algorithmic throughput. In addition, the throughput for the annular PCA might be overestimated as, it is define in a way that at every distance the best subtraction of the PSF and of the quasi-static speckles is operated. However, in term of contrast the last one was the most stable and performing method for these cubes. Indeed if median subtraction and median annular subtraction methods provide slightly better results for some particular cubes they were much more variable from one cube to an other. The same drawback was noticed for the LLSG

method which provides extremely good results close to the star for the 4.84% null leak threshold cube but bad ones for all the other cubes. We believe the stability criterion of is great importance as unstable results would considerably reduce the conclusion we can make on the impact of the different parameters of the cubes (integration time and null leak threshold among others). Considering all those aspects we choose the FFPCA method to further analyse and compare these data.

It is important to note that we consider the impact of the principal components (PCs) number used to build the throughput and contrast curves. For both the 2018's and merged cube we run several times a same cube with for each run a different number of PCs comprised between 1 and 10. In Figure 5.7 we present the results obtained for the 14.53% null leak threshold 2018's cube.

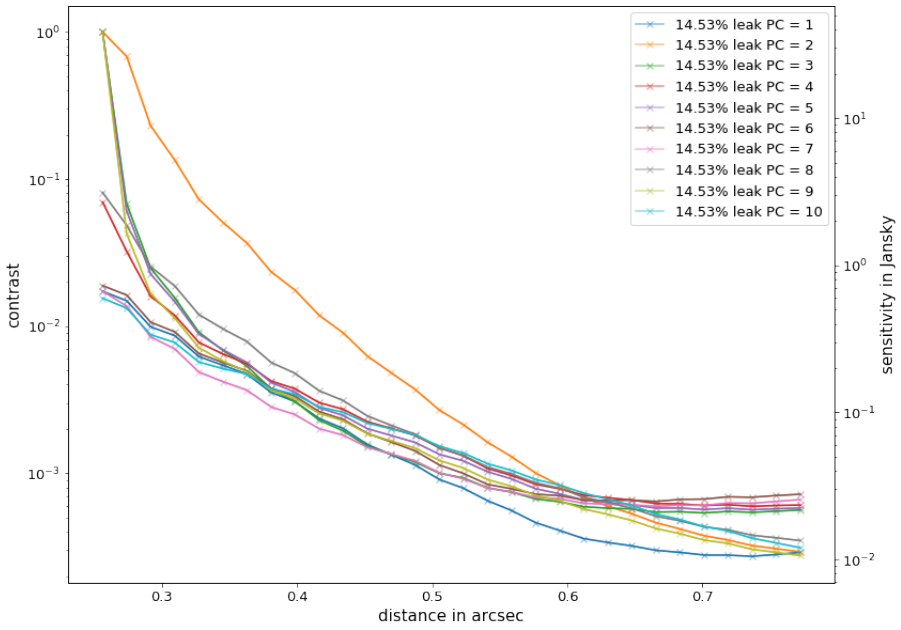

Figure 5.7: Comparison of the contrast curves with different PCs number for the 14.53% null leak threshold 2018's cube

As we can see in Figure 5.7, some PCs numbers give relatively poor contrast curves. This conclusion tends to be the same for all the cubes (ADI and RDI, α Lyrae and β Leo). The contrast curves computed with 2 PCs were, for almost all the cubes used in this master thesis, very bad compared to others. Further investigations are required to understand this result. Nonetheless, we discard all those PCs numbers which provide in several cubes contrast curves much more pessimistic than the others. Then we consider the ones which on the contrary provide the best results. Here those are the 1,7 and 10 PCs. Of course they were not the same for all the cubes, let alone between ADI and RDI. We decided to choose a PCs number which will give overall better results for all the cubes and techniques. It happens to be 1. In the following 1 PC will thus be used to build the throughput curves as well as the contrast curves.

We begin the real analysis of α Lyrae by the 2018's cubes. An interesting characteristic of these cubes is their very narrow range of parallactic angles (10) which in the case of ADI could lead to an important self-subtraction of the potential exoplanet. The variety of cubes we used also provide a good insight on the impact of the loss in integration time and the gain in null leak threshold. The contrast curves obtained with the FFPCA method for all the 2018's cubes are presented in Figure 5.8.

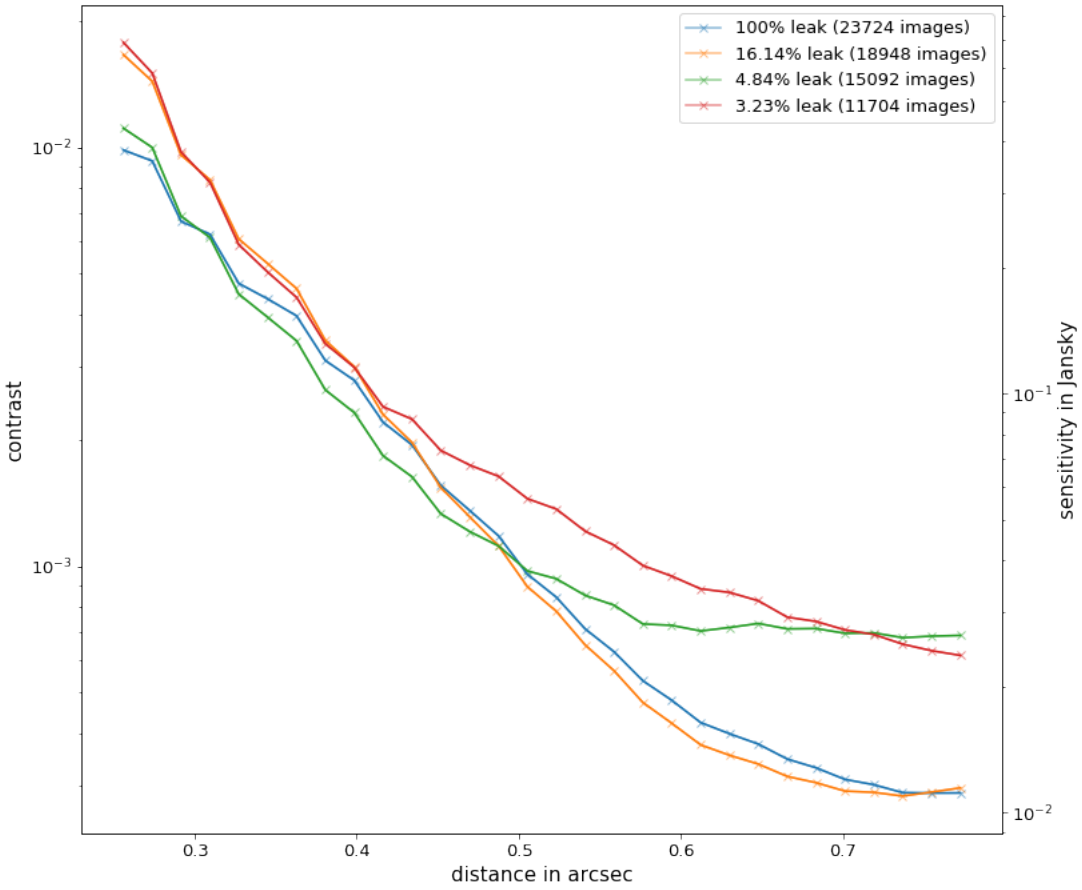

Figure 5.8: Contrast and sensitivity curves for each cube as a function of the distance to the star in arcsec

We plotted here the four most interesting curves for our study. The 100% null leak threshold cube was taken as a reference to compare the improvement or degradation of the other curves depending on their selection and integration time. A first important difference, that we can see in Figure 5.8, with what we would have expected is the very good contrast provided by the 100% null leak threshold at 0.25 arcsec from the star. Indeed the contrast close to the star is expected to become better as the null quality improve, thus corresponding to the most selective cubes. In the same time, we can notice that the cube which is expected to provide the best results at 0.25 arcsec gives in fact the worst one. A possible explanation of these results is the loss in integration time. There is indeed an important loss between the 100% null leak threshold cube and all the other cleaned cubes. This could suggest that the gain in null quality was not enough to compensate for the loss in integration time. The results obtained at 0.77 arcsec are, however, much closer to the expected ones as the cubes with greater integration time give the better results. We can see nonetheless that the 16.14% null leak threshold cube gives results very close than those of the 100% null leak threshold cube, this can suggest that in this case the loss in integration time is compensated by the gain in null quality. We further discuss the behavior of the contrast close (at 0.25 arcsec) and far (at 0.77 arcsec) to the star in the following with the insight provided by the analysis of the merged cube.

We display in Figure 5.9 the final images corresponding to the contrast curves plotted in Figure 5.8 for a reference PSF built thanks to FFPCA with 4 PCs and for an optimized number of PCs.

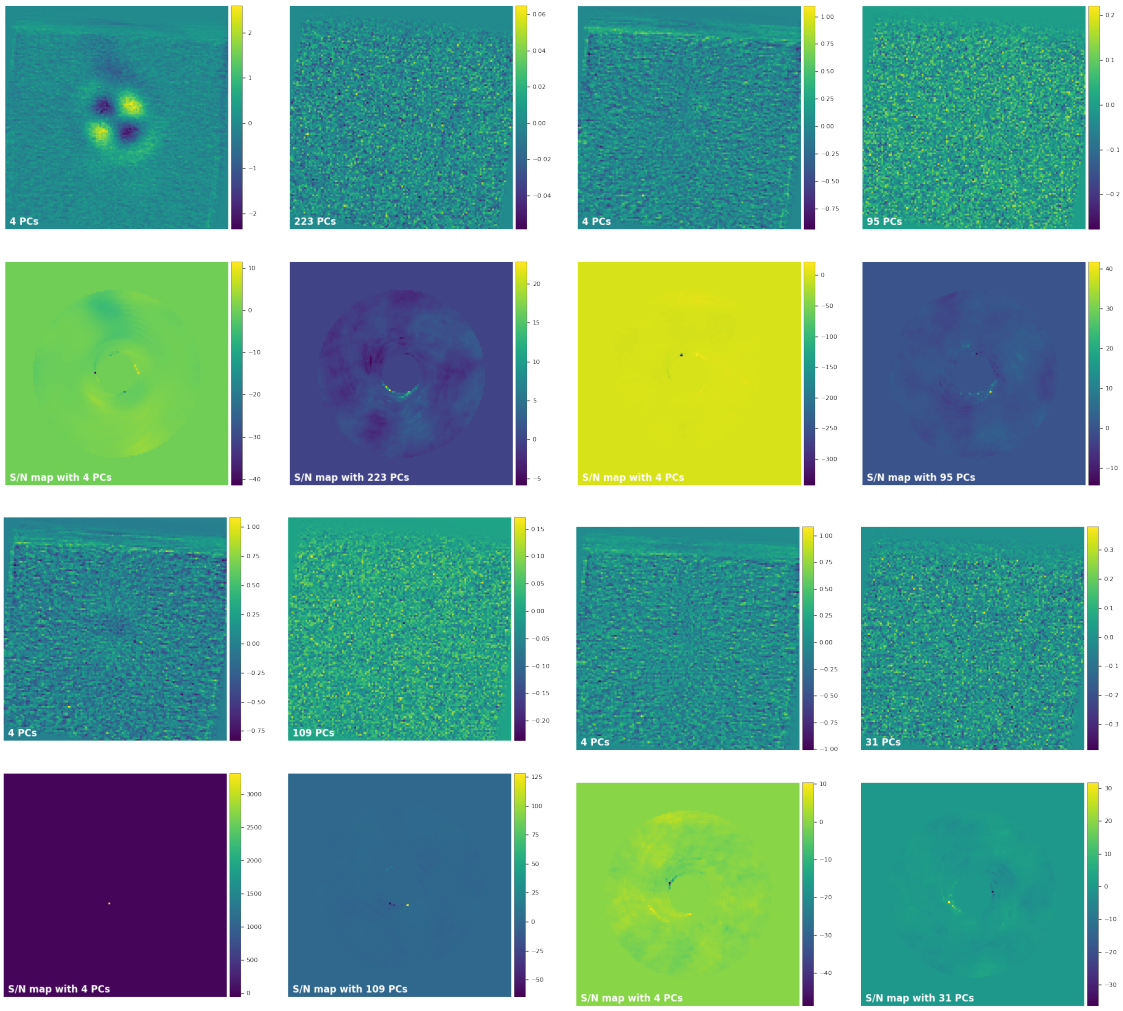

Figure 5.9: Final images for the 100% null leak threshold 2018's cube (top left), the 16.14% null leak threshold 2018's cube (top right), the 4.84% null leak threshold 2018's cube (bottom left) and the 3.23% null leak threshold 2018's cube (bottom right) with their S/N maps.

The merged cube provides a wider range of parallactic angles and a greater integration time. It is important to note that a 4.04% null leak threshold cube was added and has no equivalent in the 2018's cubes. This cube gives a point of comparison with the 2018's cubes as it possess approximately the same integration time than the 100% null leak threshold 2018's cube. As expected, all the results obtained with this cube were better than on the previous ones, which is shown in Figure 5.10.

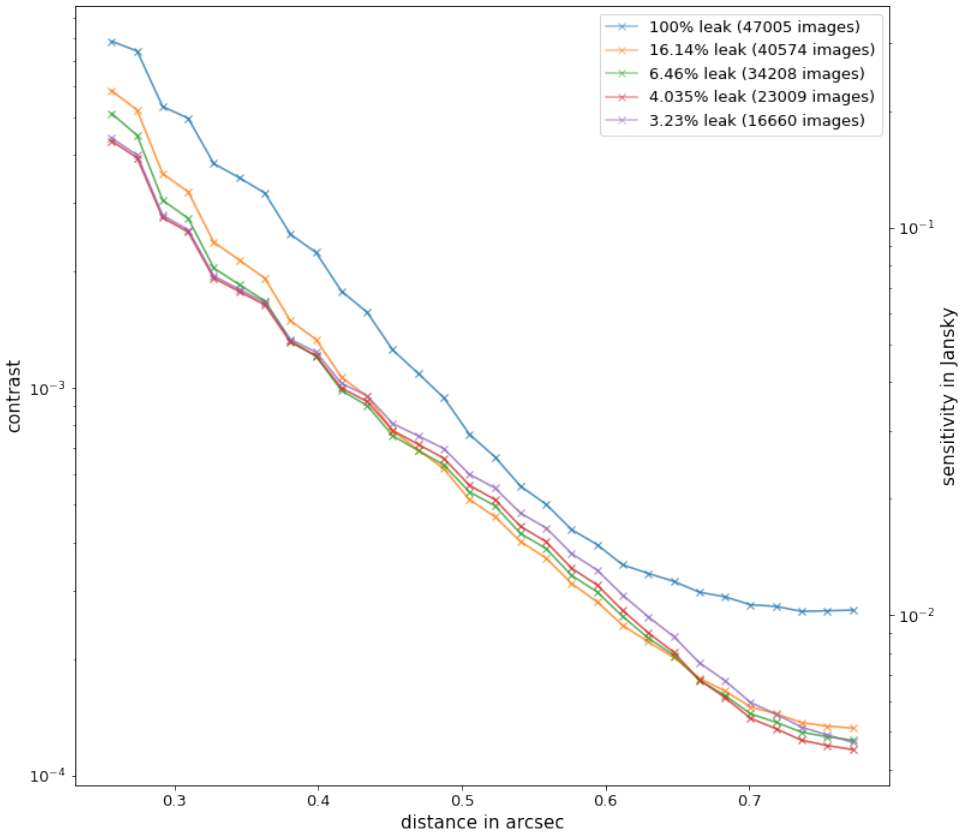

Figure 5.10: Contrast and sensitivity curves for the merged cubes

A first major difference we can see between these cubes and the 2018's cubes is the better results of the cleaned cubes compared to the 100% null leak threshold cube. This suggests that with the overall gain in integration time this parameter became less critical and the selection is not as much counter-balanced by the loss in the number of frames. If we now focus on the 0.25 arcsec contrast values we can see that they look exactly like expected if not for the tiny inversion between the 4.84% and the 3.23% null leak threshold cubes. However this can once more be explained by the important loss in integration time (8.5 minutes of integration time loss) between these cubes. A much more surprising result is found at 0.77 arcsec where the most selective cubes provide the better results. Indeed far from the star the contrast is supposed to became better as the integration time increase.

In Figure 5.11 we display the final images obtained for the merged cubes which contrast curves have been plot in Figure 5.10, for 4 PCs used to build the reference PSF through the FFPCA methods and for an optimized number of PCs along with their S/N maps.

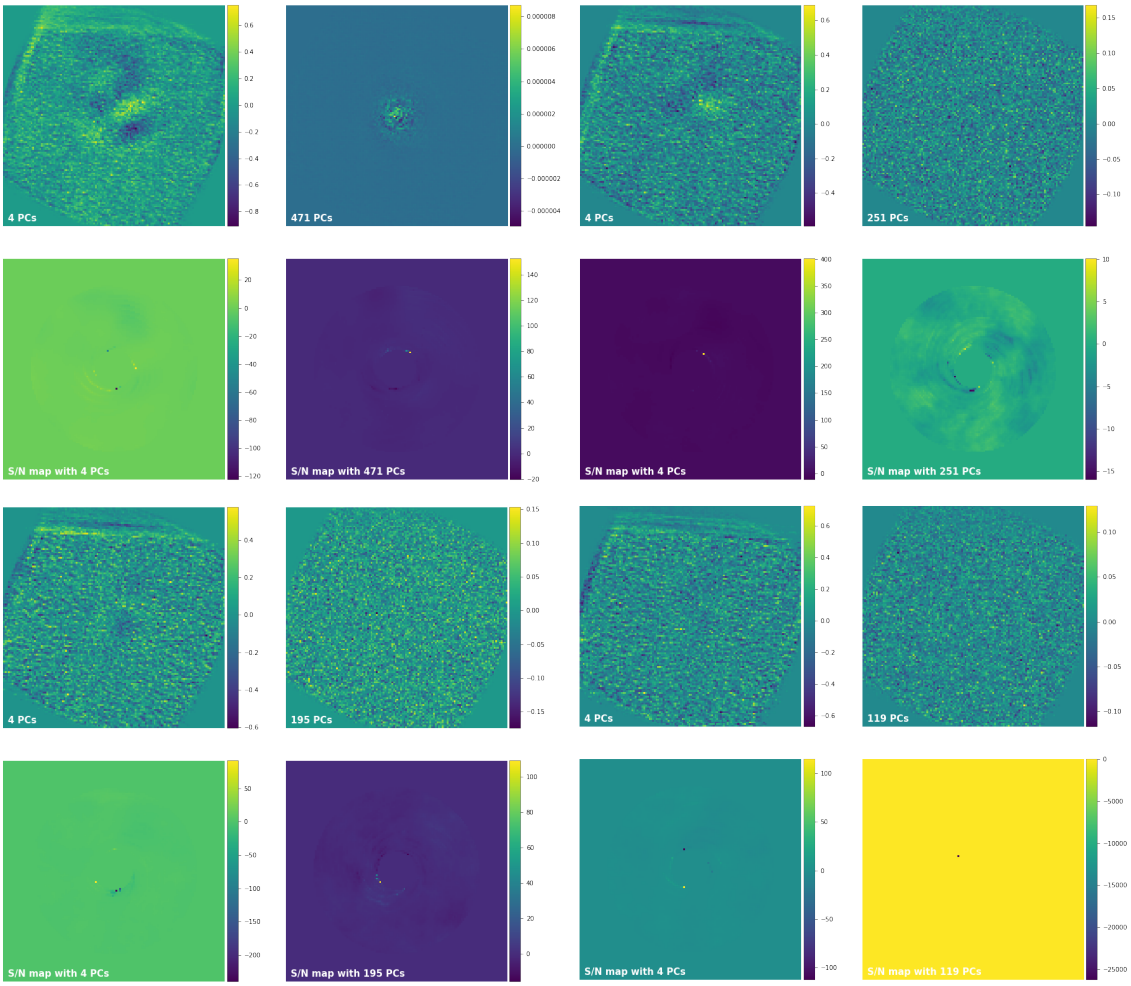

Figure 5.11: Final images for the 100% null leak threshold merged cube (top left), the 16.14% null leak threshold merged cube (top right),the 6.46% null leak threshold merged cube (bottom left) and the 3.23% null leak threshold merged cube (bottom right) with their S/N maps.

To better understand the impact on the different parameters close to the star (at 0.25 arcsec) and far from it (at 0.77 arcsec) we plotted the behavior of the contrast in each case. To do so, we take for each cube the value of the contrast at 0.25 arcsec and 0.77 arcsec for the different level of MNT.

Far from the star, we know that the contrast is supposed to improve as the inverse of the square root of the integration time in the background-limited regime. As a first step we plotted the contrast at 0.77 arcsec for each cube along with his supposed behavior that we denoted "Theoretical curve" in Figure 5.12. It is important to note that we use a normalization factor to make coincide the obtained contrast for the 16.14% null leak threshold cube and its theoretical value. This normalization factor is defined as:

$$C_{16.14}\sqrt{T_{16.14}}$$

with $C_{16.14}$ the contrast value for the 16.14% null leak threshold cube and $T_{16.14}$ its integration time.

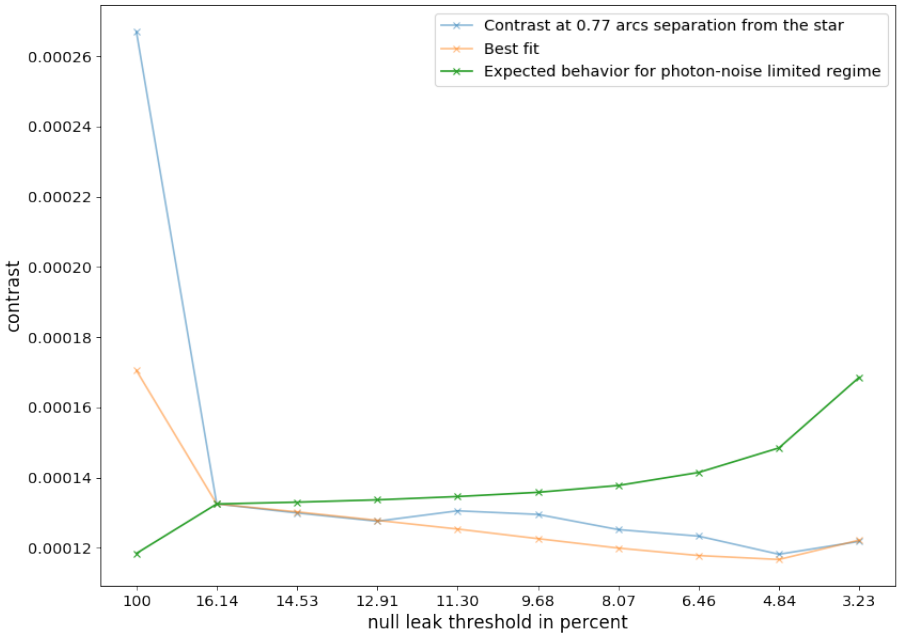

Figure 5.12: Expected behavior of the contrast as a function of the null leak threshold, assuming we are in the background limited regime, and obtained contrast at 0.77 arcsec

As we can see the expected behavior does not match properly the obtained contrast and even tend to show the opposite behavior when we become more and more selective on the flux. Considering this divergence and to better understand the impact of both parameters (integration time and null leak threshold) on the contrast behavior at 0.77 arcsec we tried to build a curve which will fit the obtained contrast better. We first check if other orders of the integration time provided a better fit (square root, square, inverse of the cubic root,...) but the inverse of the square root was still the best fit. We so introduce a factor taking into account the null leak threshold of the cube and once again try different order until we found the best match with the fifth root of the null leak threshold. The curve "Best fit" of this graph corresponding to

$$\frac{C^{\text{ext}}{}_{16.14}\sqrt{T_{16.14}}}{\sqrt{T}} * \sqrt[5]{L}$$

with $C^{\text{ext}}{}_{16.14}$ the obtained contrast for the 16.14% null leak threshold cube, $T_{16.14}$ its integration time, T the integration time of the considered cube and L its null leak threshold.

We did the same analysis for the internal behavior (at 0.25 arcsec). We know in this case that close to the star the behavior must be tied to the null quality and therefore the null leak threshold of the cubes. We started from this knowledge to build a curve that will fit the internal behavior. As for the external analysis we tried several orders of the null leak thresholds (square, square root, cubic root, fourth root,...). Even if significant differences from the fit persist we found the best curve to be the sixth root of the null leak threshold. Once again it was normalize but this time only with the value of the contrast obtained for the 16.14% null leak threshold cube, providing a final equation for the fitting curve:

$$C^{\text{int}}{}_{16.14}\sqrt[6]{L}$$

with L the null leak threshold of the considered cube. This result is shown in Figure 5.13.

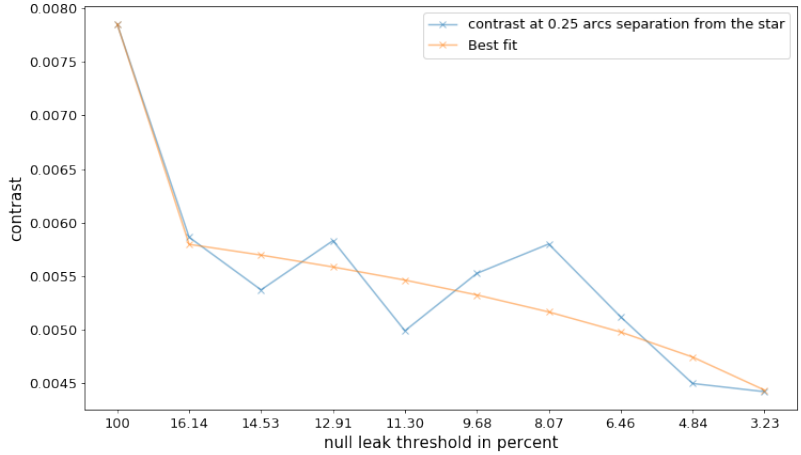

Figure 5.13: Obtained contrast at 0.25 arcsec as a function of the null leak threshold and its best theoretical fit

As we can see the fitting curve only follows the general evolution of the contrast but not its smaller variations which seem to adopt a sinusoidal-type behavior.

The analysis of the external behavior curve shows that even at 0.77 arcsec from the star we are still out of the photon-noise limited regime. Indeed, we can see on Figure 5.12 that the expected behavior for such a regime is not consistent with the obtained contrast, in particular for the most selective cubes. The factor $\sqrt[5]{L}$ we found to correct this theoretical curve is also a good indicator to prove we still didn't reach the photon-noise limited regime. By looking at the contrast curves for both the 2018's cube and the merged cube we can see that almost all the curves did not yet reach their plateau at the large separation. For the 2018's cube only the 4.84% and 6.46% null leak threshold cubes seems to have already reached it. In the case of the merged cubes the 100% null leak threshold cube is the only one showing a similar behavior. It is however interesting to note for the 2018's cubes that most selective cubes seems to reach their plateau first, in particular if we take a look at the 8.07% null leak threshold cube which also seems to be about to reach is plateau. This could suggest that the $\sqrt[5]{L}$ corrective term we found for the best-fit curve is partly due to the tendency of the most selective cubes to reach their plateau faster than the less selective ones. However, Figure 5.10 does not present a similar behavior. This can be due to the greater integration time of the merged cube, as the most selective cubes have the smaller number of frames, but this is unlikely as the 6.46% null leak threshold 2018's cube and the 3.23% null leak threshold merged cube share approximately the same integration time and do not display similar behaviors. The possibility of the null leak threshold to be responsible is also very unlikely as the cubes sharing the same null leak threshold do not show similar behaviors. If the difference between the 2018's cubes and merged cubes for the distance at which they reach their plateau is to be input to a parameter of the cubes it might be the range of parallactic angles. However there is a distinct possibility that this difference comes from different level of noises as, in both cases, we are still out of the photon-noise limited regime.

In the case of the contrast at 0.25 arcsec from the star, the overall behavior seems to be even more complex. Indeed if the $\sqrt[6]{L}$ curve seems to provide a good general approximation of the contrast behavior, the huge differences and the unexpected inversion strongly suggest that a least one additional parameter is needed to theoretically describe this behavior. As the parallactic angles range stay the same for the merged cubes, the inversion could hardly be explained thanks to this parameter. The integration time, furthermore, if it varies cannot explain by its own the inversions as it, of course, decreases with the selection. One also could think of the ratio of the null quality and the integration time as the selection provide a gain in null quality which can be balanced with the loss in integration time. However this would have concentrated the inversion to the three most selective cubes as they are the only ones with important integration time loss compared to their gain in null quality. Indeed the cubes 16.14%, 14.53%, 12.91%,11.30% and 9.68% null leak

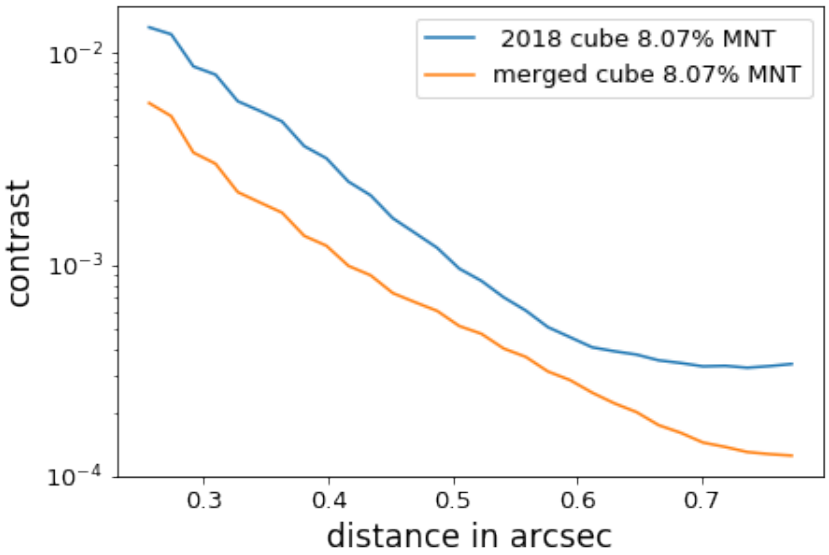

Figure 5.14: Comparison between the 2018 and merged 8.07% null leak threshold. The two curves show a significant improvement of the overall curve. We know have to determine which parameter has the strongest impact.

threshold cubes have a very small decrease of their integration time and a continuous gain in null quality. This behavior is probably due once again to noises which might take more importance from one selection to another.

Further investigations for the reason of the behavior of the contrast at 0.25 arcsec as well as 0.77 arcsec is, however, beyond the scope of this master thesis.

To get a better insight in the role of each parameter of the cubes in the ADI processing we further compare two pairs of cubes: the 8.07% null leak threshold 2018's and merged cubes, which have the same null quality but a different range of parallactic angles and integration time, and the 14.53% and modified 14.53% null leak threshold merged cubes, which have the same range of parallactic angles and null quality but different integration time. This last cube was specifically built for this comparison by taking only one in two images from the 14.53% null leak threshold cube. We choose this cube in particular for its important number of images and the quality of its contrast curve.

In this first analysis we compare the 2018's and merged cube 8.07% null leak threshold cubes to see the combined impact of the parallactic angles range widening and of the integration time increase. This comparison is shown in Figure 5.14.

As we can see on this figure we found a significant improvement of the overall contrast curve. However it also shows a greater relative improvement close to the star than far from it. Indeed the improvement close to the star is of the order of 46% and far from it drops to 35%. When considering the impact of both of the varying parameters in function of distance: the parallactic angles range widening having a greater impact close to the star and the integration time increases far from it; it seems to indicate a greater effect of the parallactic angles range widening.

We then compare the modified and original 14.53% null leak threshold cubes to study the effect of the integration time alone. This is shown in Figure 5.15.

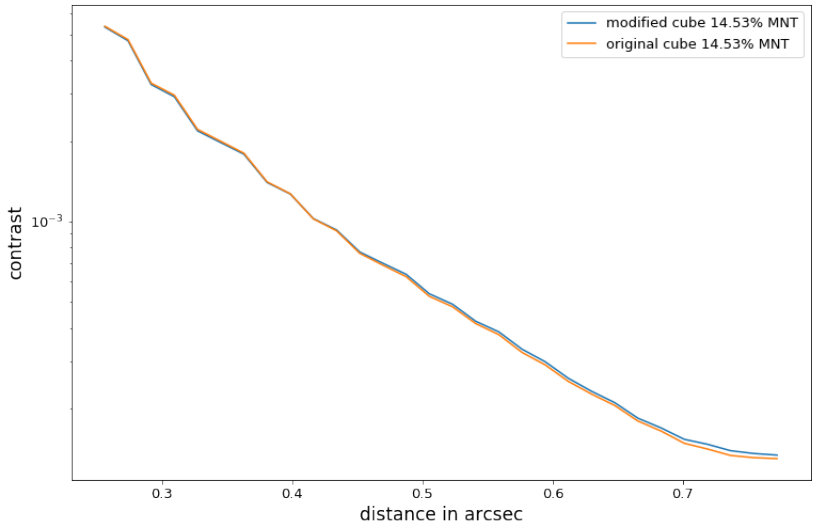

Figure 5.15: Comparison between the original and modified 14.53% null leak threshold cubes. The difference between the two cube are tiny in comparison of the difference obtained in Figure 5.14 suggesting that the impact of the integration time is very weak in this case.

As we can see in Figure 5.15, the effect of the integration time increases is very small which was, in itself, unexpected. There is however an even more surprising result shown on this graph which is the inversion between the original and the modified cubes, this last one showing slightly better results close to the star. This can be explained if we consider than among the images discarded in the modified cube were some of the lowest quality and thus that the null leak threshold in the modified cube is very slightly lower. However this shows how very little the increase of the integration time improve the contrast curve compare to the other parameters. The other half of the images was also studied in the same way showing an even stronger effect of the slight improvement of the null quality.

Even considering that the integration time has only been doubled and that the parallactic angles range has been widen by a factor 3.5, it hardly explains that huge difference between both parameters. These results tend to indicate one more time that widening the parallactic angles range is much more efficient to improve the contrast curve than the integration time increase. This is even more flagrant when we remember that the modified cube contains only 20165 images, even less than the 4.84% null leak threshold cube with which the original 14.53% already shows a greater contrast difference.

5.2.2 β Leo

In order to be coherent with the analysis of α Lyrae, we kept as much identical parameters as possible. We, in particular, kept the FFPCA method to analyse the β Leo images, as it shows good and stable results for them too. Another parameter we kept is the PCs number. However we perform a full analysis on the impact of the PCs number to check that it does not introduce significant changes in the contrast curves. As for α Lyrae we discard the PCs number providing relatively bad curves for each cubes. In the remaining PCs number was 1 which we choose for its quality as well as for coherency.

Those parameters chosen, we then perform a complete analysis for both the Mean cubes and the Median cubes. We present the results in Figure 5.16.

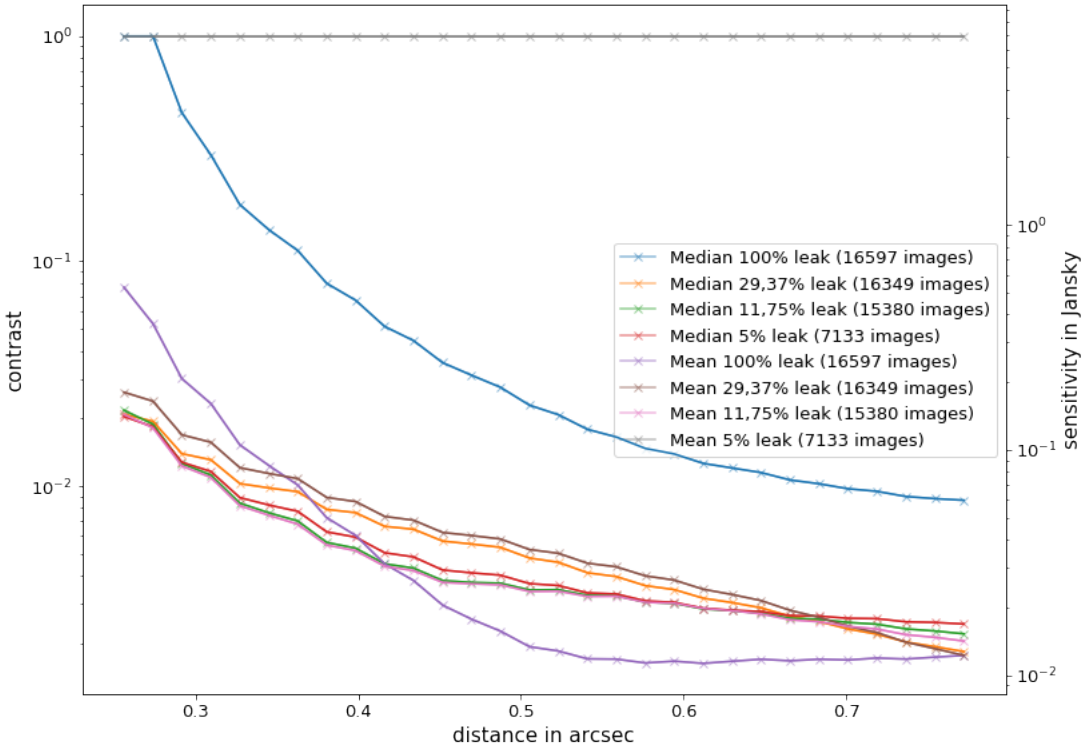

Figure 5.16: Contrast and sensitivity curves for the Mean and the Median cubes and for the different MNT levels. We can see than the Mean subtraction gives the best results in all cases. However, the Mean 5% MNT curve is extremely bad. The reason why the corresponding Median curve behaves that differently would need further investigation.

A first interesting result is that at separation larger than 0.4 arcsec the curve giving the best result is the Mean 100% null leak threshold cube, as we would have expected, and that by comparison with α Lyrae cubes, this time it already reached its sensitivity-limited plateau. It is important to remember however that no results further than 0.62 should be taken into account due to the cropping of the frames. If we now consider the 0.25 arcsec case, we can see that the best curve is obtained with the Mean 11,75% null leak threshold cube. It was expected that the 5% null leak threshold cubes would give the best results close to the star as they are the most selective. If the Median 5% null leak threshold cube is very close to the contrast given by the best contrast curve at 0.25 arcsec, the Mean 5% null leak threshold cube gave a contrast equal to 1. This can be partly explained by the important loss in integration time compared to the improvement in null quality. However the different behaviors of the Mean and Median 5% null leak threshold cubes is very interesting as it could suggest a difference of sensibility to the integration time, and that for example the Median subtraction could be much efficient for small cubes. Another interesting result when compared to the 2018's α Lyrae cubes is that the sensitivity obtained is very similar, in particular far from the star. It is also important to note that the best curves (at 0.25 arcsec as well as at 0.62 arcsec) are both given by Mean cubes, suggesting that this background subtraction method might be more adapted to this cube. However this should be considered carefully, as we can see in Figure 5.16, it is not the case for all the cubes when compared with their corresponding Median cubes.

In Figure 5.17 we display the final images obtained for the mean and median cubes, respectively, which contrast curves have been plotted in Figure 5.16, for 4 PCs used to build the reference PSF through the FFPCA methods and for an optimized number of PCs along with their S/N maps.

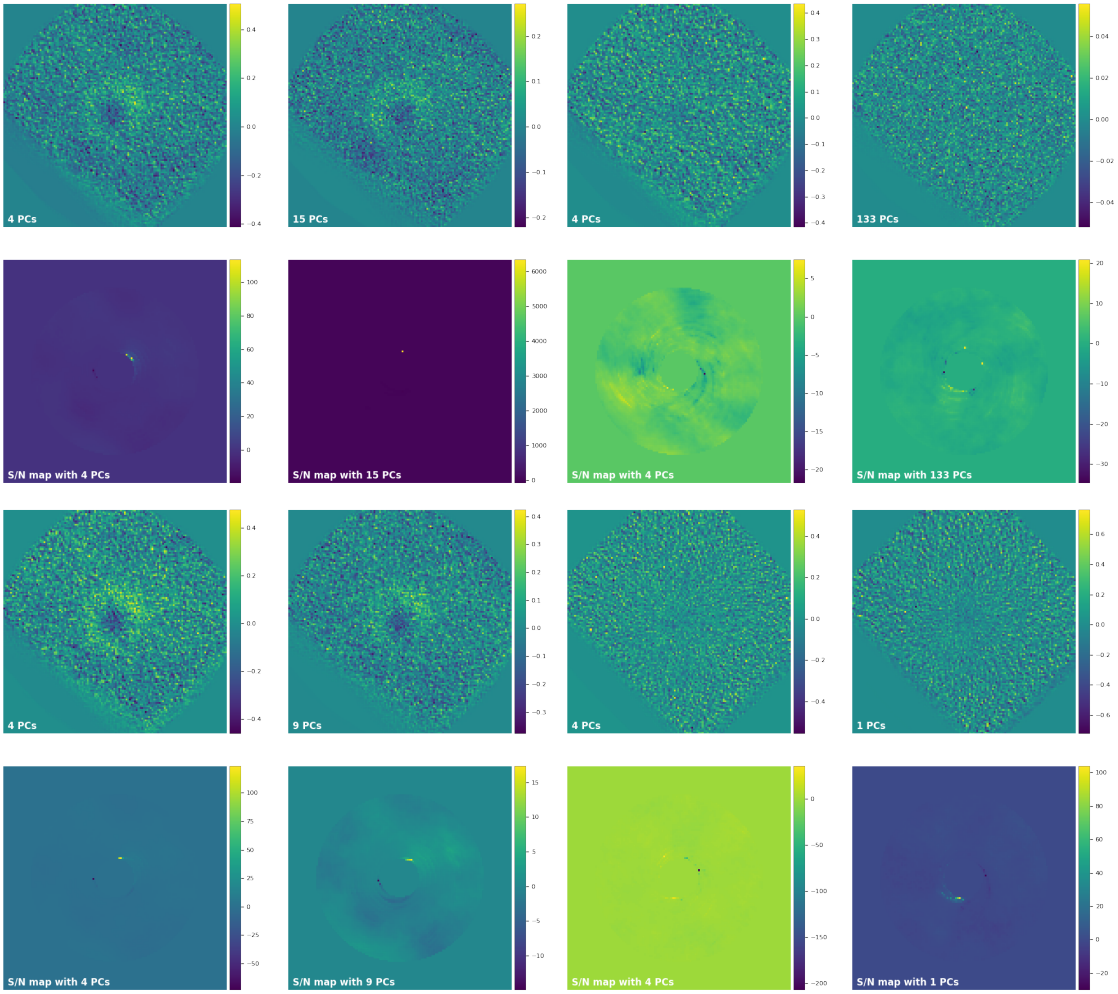

Figure 5.17: Final images for the 100% null leak threshold Mean cube (top left) and the 11.75% null leak threshold Mean cube (top right),the 100% null leak threshold Median cube (bottom left) and the 11.75% null leak threshold Median cube (bottom right) with their S/N maps.

We then compare in more details, as for α Lyrae, the impact of the different parameters (integration time, parallactic angles and null quality). For β Leo we were not able to compare two cubes with the same leakage but different integration time and parallactic angles or different leakage but same integration time as we did for α Lyrae. Indeed we work on one cube which background has been subtracted in two different ways but they have the same integration times and the same parallactic angles unlike the 2018's and merged cubes for α Lyrae. However we were able to estimate the effect of the background subtraction method as it has been shown in Figure 5.16. It was also possible to estimate the effect of the integration time on β Leo 's cubes. We did this comparison for both the Mean and Median 11.75% null leak threshold cubes in order to check if the background subtraction method introduces or not a difference in the effect of the integration time as suggested by the contrast curves shown in Figure 5.16. For this purpose we built a modified cube where we took only one image over two thus reducing the integration time while keeping the same range of parallactic angles. This is shown in Figure 5.18.

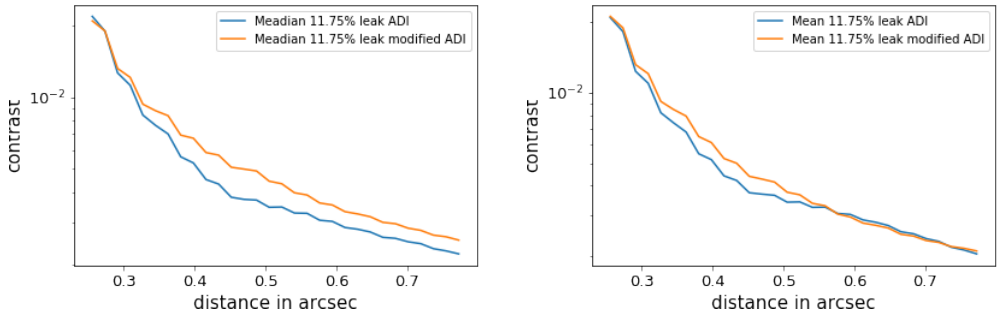

Figure 5.18: Comparison of the integration time modified cube and the original cube for the Median background subtraction method (left) and the Mean background subtraction method (right)

As we can see, in both cases, the reduction of the integration time introduces a degradation of the contrast curves at almost every distance from the star. In the case of the Median cubes we can see however that the modified cube is slightly better at 0.25 arcsec, this can be easily explained if we consider that taking one image over two can introduce a little selection on the flux as we can discard some of the worst frames. The inversion on the Mean cubes, is on the other hand hardly explained by this possible selection on the flux. However as we are close to the cropping of the images, it is possible that frames of higher noise at 0.6 arcsec have been discard thus improving the quality of the modified cube at this distance. It is also interesting to point out that the Median background subtraction method seems more sensitive to the integration time variation than the Mean subtraction method.

We made a second comparison, this time to estimate the impact of the parallactic angles range. To do so, we built a cube which corresponds to only the first half of the original cube. Doing so we obtained a cube with the same integration time than the previous modified cubes but with a parallactic angles range much smaller. Once again we did this comparison on both the Mean and Median cubes. The results are presented in Figure 5.19.

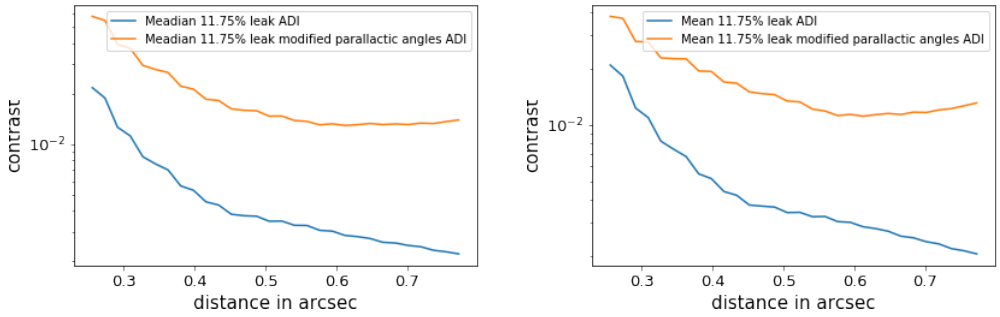

Figure 5.19: Comparison of the parallactic angles modified cube and the original cube for the Median background subtraction method (left) and the Mean background subtraction method(right)

In both cases we can see a huge degradation when the range of parallactic angles is reduced. When compared to the comparison based on the reduction of the integration time, we can see that the parallactic angles have a much greater effect in improving the contrast curves.

5.2.3 Improvement of the contrast curves

α Lyrae

In order to improve the contrast curves we proceed to two additional tests, consisting in subtracting the Mean or the Median images of the whole cube before running the FFPCA processing. The Mean and Median images of the cube were build before derotating the images so the potential

companions do not significantly self-subtract. After those subtractions we obtained images with narrower flux ranges. This result is shown in Figure 5.20.

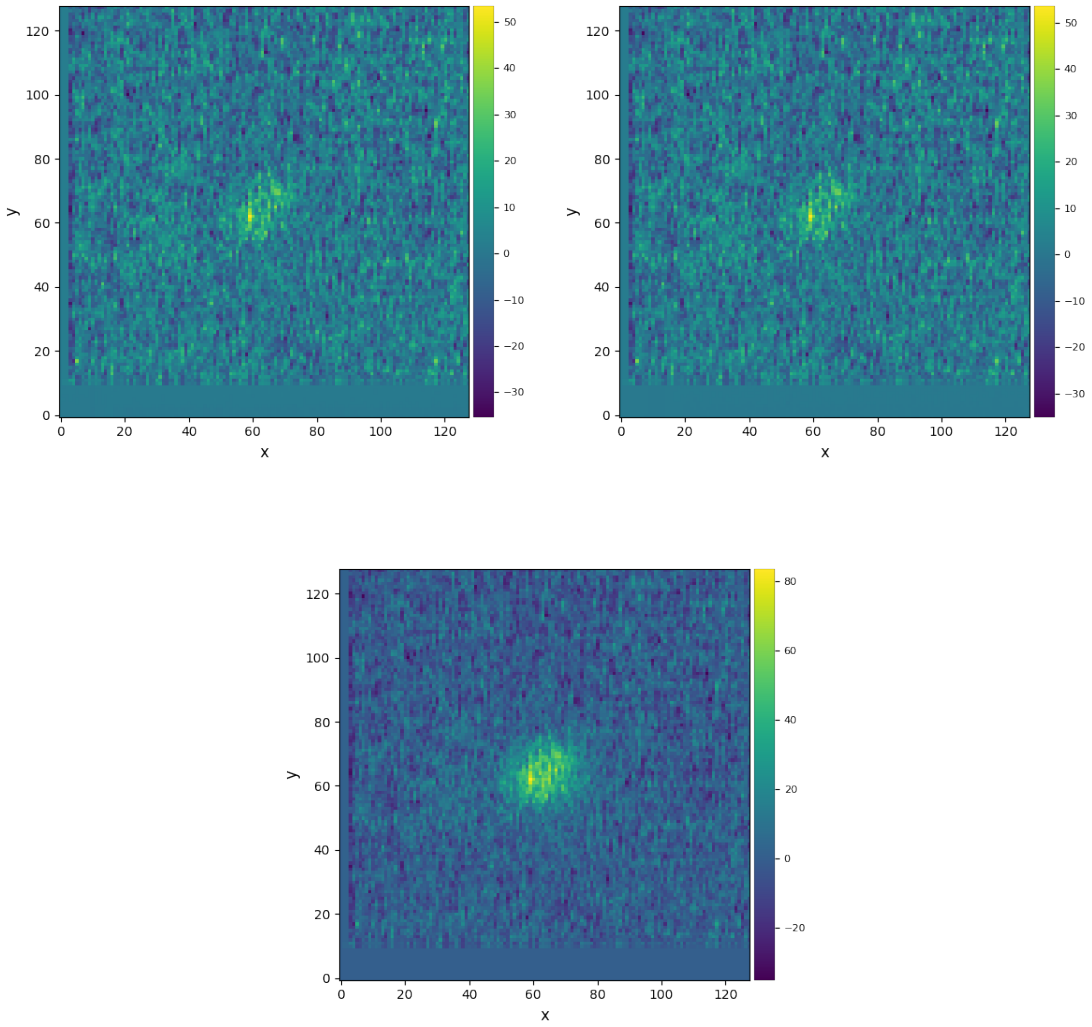

Figure 5.20: Frame subtracted with the mean image of the cube (top left), the median image of the cube (top right) and without subtraction (bottom).

As we can see the two first images are very similar, however looking carefully at the color range we can notice that the Mean-subtracted image is slightly better. We nonetheless run the FFPCA for both the new cubes, and Figure 5.21 shows that if the Median-subtraction significantly degrades the obtained contrast curves, the Mean-subtraction on the opposite improved the contrast curves by an order of magnitude.

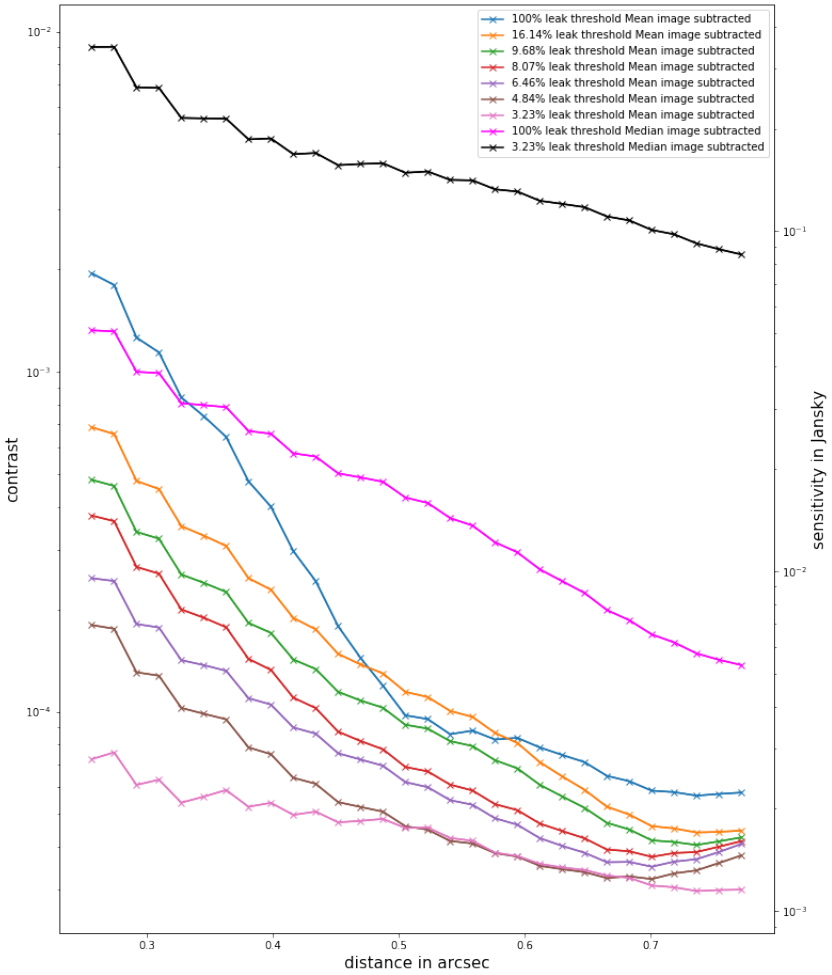

Figure 5.21: Contrast and sensitivity curves of the merged cubes with the Mean and Median image subtracted before the FFPCA processing

As we can see in Figure 5.21, we now reach very good contrasts with the Mean image pre-subtracted, and we wanted to check that these subtractions do not disturb the algorithms computing the throughput and the contrast curves. To do so we use the VIP functionality allowing to inject fake companions at different flux levels and distance from the star. We show in Figure 5.22 the final images with fake companions at different flux levels and in Figure 5.23 the final images with fake companions at different distance from the star.

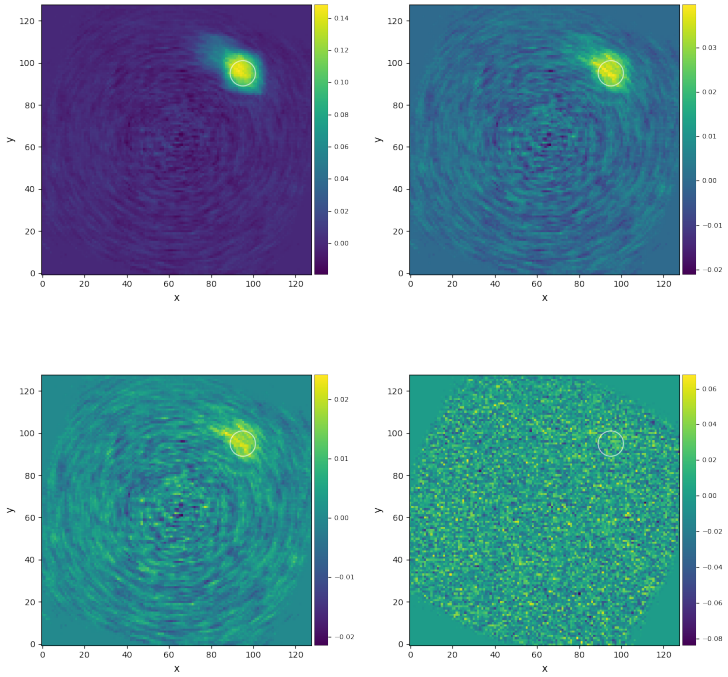

Figure 5.22: Final images with fake companion at a distance of 45 pixels and with flux levels at 0.006% (top left), 0.0015% (top right), 0.0008% (bottom left) and 0.00015% (bottom right) of the maximum flux of the star (619585 ADU).

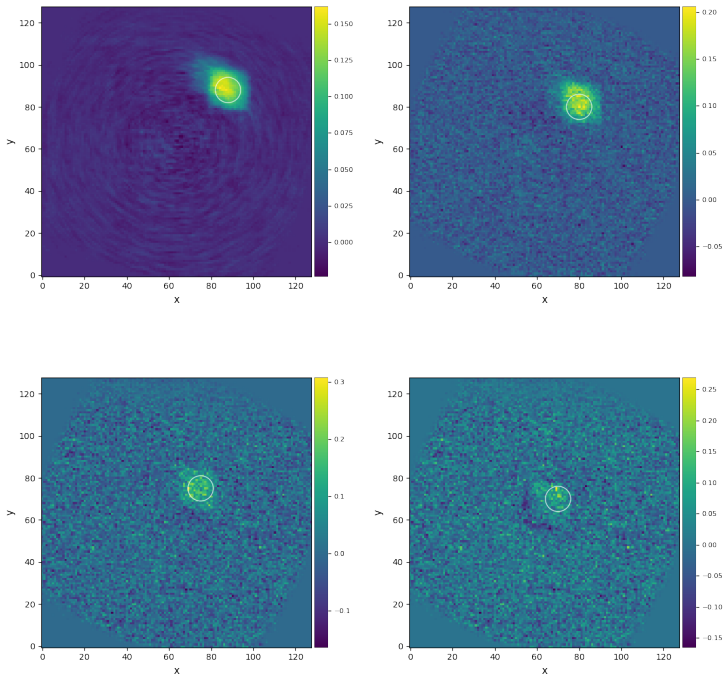

Figure 5.23: Final images with fake companions at a flux level of 0.006% of the maximum flux of the star (619585 ADU) at a distance of 35 pixels (top left), 25 pixels (top right), 15 pixels (bottom left), 5 pixels (bottom right) from the center of the frame.

The images presented in Figure 5.22 and Figure 5.23 were computed from the final images ob-

tained with FFPCA for the 3.23% null leak threshold cube after the pre-subtraction of the median image (obtained before the derotation of the images) in which we injected a fake companion. In the first set of images we injected a fake companion, at 45 pixels from the star, with different flux levels (0.006, 0.0015, 0.0008 and 0.00015% of the maximum flux of the star) in order to determine if the contrast curves were realistic. In the second set of images we injected a fake companion with the same flux level (0.006% of the maximum flux of the star) but at different distance from the star (35, 25, 15 and 5 pixels from the star) in order to check if the previsions of the contrast curves were realistic at different distances. As we can see, the images confirm the contrast levels predicted by the contrast curves. However we can notice in some of these images a circular pattern in the noise which seems to appear when the flux of the fake companion is significant compared to the noise and is not fully understand.

The contrast behavior at 0.77 arcsec of the new contrast curves is not plotted here but one can see on Figure 5.21 that the most selective cubes are providing the best results at 0.77 arcsec and thus that the photon-noise limited regime has not been reached yet.

β Leo

The same tests to improve the contrast curves than for α Lyrae were made for β Leo by subtracting the Mean or the Median images of the cubes to each frames before running the FFPCA processing. It is important to note here that β Leo possesses two cubes: one with Mean background subtraction and the other with Median background subtraction. These tests were made on both, allowing us to estimate if one subtraction method (Mean or Median before the FFPCA processing) was more adapted to one background subtraction method. This time, however, we do not notice any significant difference between the two subtractions nor any additional difference between the Mean and the Median background subtracted cubes. Those results are shown in Figure 5.24.

As we can see in Figure 5.24, as in the case of α Lyrae, the contrast curves improved by an order of magnitude, but this time in both cases. The reason why we obtain such a difference of improvement for the Median subtraction between α Lyrae and β Leo is unclear but further investigation of this result is beyond the scope of this master thesis.

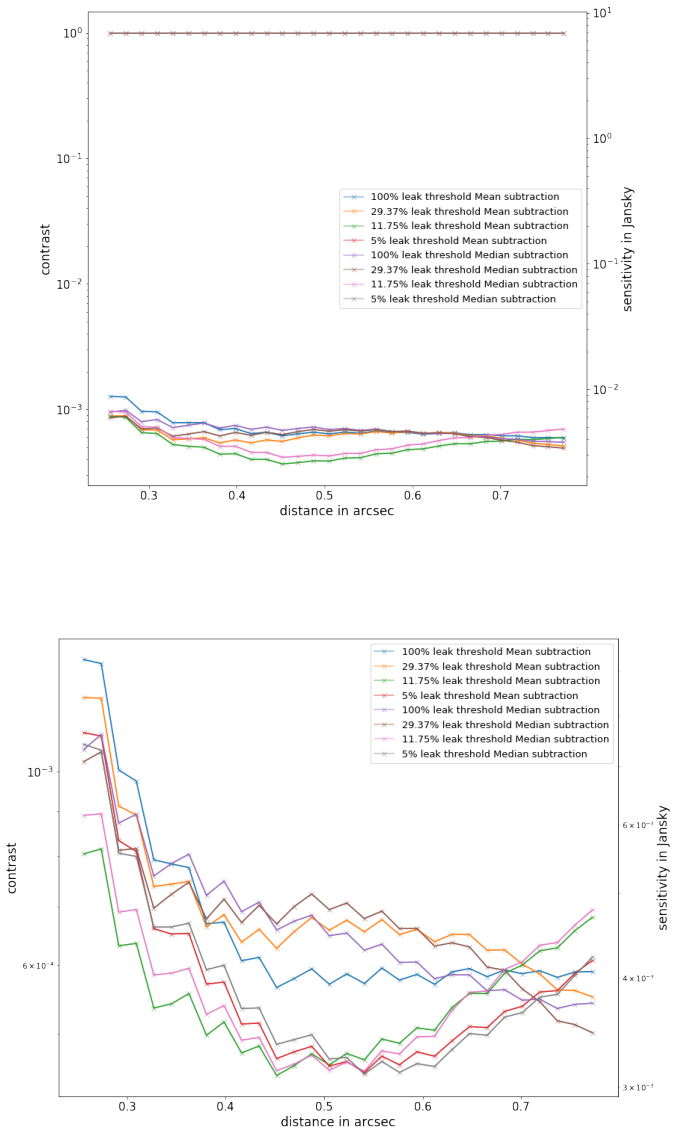

Figure 5.24: Contrast and sensitivity curves for the Mean and Median cubes with the Mean (top) and the Median (bottom) image of the cubes subtracted before to run the FFPCA processing.

5.3 RDI processing

5.3.1 α Lyrae

Our second analysis of α Lyrae was made with the RDI technique which requires a reference star to reduce the cube. To be consistent with the ADI processing we kept the FFPCA processing technique for the following analysis. To study α Lyrae RDI results in the widest possible way we consider all the reference stars taken in the two nights during which α Lyrae was observed. Among all these only the stars HD168775, HD177808, HD163770 and HD164646 were dedicated to α Lyrae, all the others were for the other scientific targets observed during these nights. However we performed the RDI processing of α Lyrae with all the calibrators. In Figure 5.25, we plotted the contrast curve for the 16.14% null leak threshold merged cube for each calibrator.

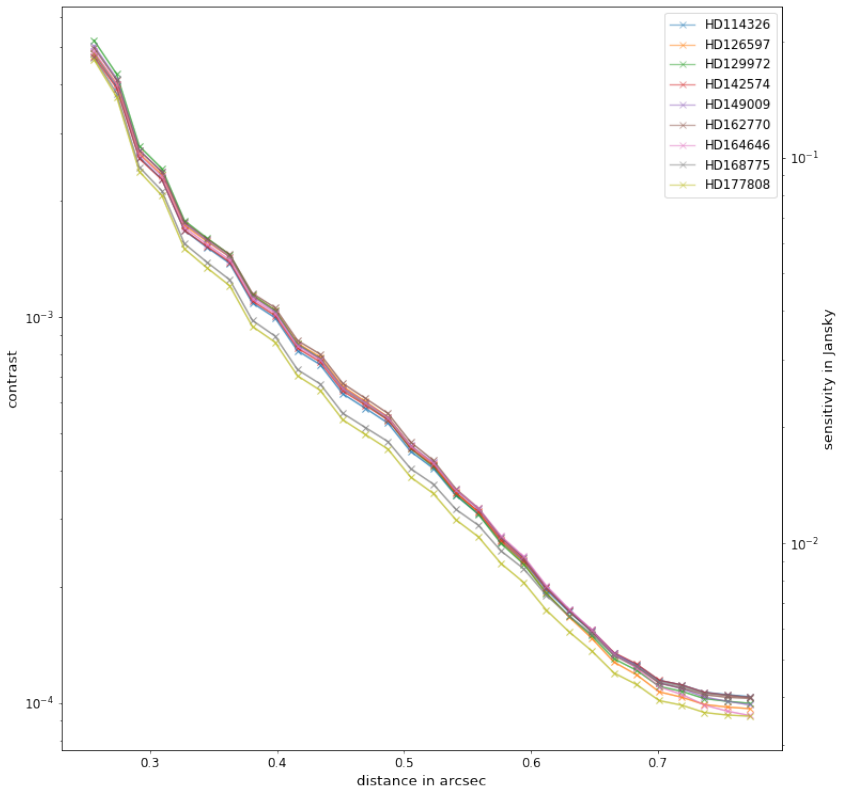

Figure 5.25: Contrast as a function of distance for each calibrator for the 16.14% null leak threshold merged cube

We show only the analysis for the 16.14% null leak threshold merged cube but it was performed on all the other cubes showing similar results but for the 100% null leak threshold cube for which the calibrator HD168775 provided slightly better results. However as we can see if HD177808 and HD168775 show overall better results, in particular between 0.3 arcsec and 0.6 arcsec the other curves are extremely similar. This can be surprising as among those some calibrators were not meant to calibrate α Lyrae, however, all of them seem to be as good as the calibrators of α Lyrae. Nonetheless, as HD177808 is better everywhere on the curve, we choose this calibrator to further analyse the α Lyrae with the RDI processing.

As for the ADI treatment of α Lyrae we then consider the impact of the number of PCs used to build the contrast curves. We did this analysis on both the 2018's cubes and the merged cubes. It appears that the RDI technique is much less sensitive to the number of PCs than ADI. However the contrast curves built with 1 PC were overall slightly better. With this knowledge and the coherence it brings with the ADI treatment we kept 1 as the PCs number for all the following analysis.

We present below the contrast curves for the 2018's cubes processed with the reference cube HD177808 as well, by concern for coherence between the 2018's cubes and the merged cubes.

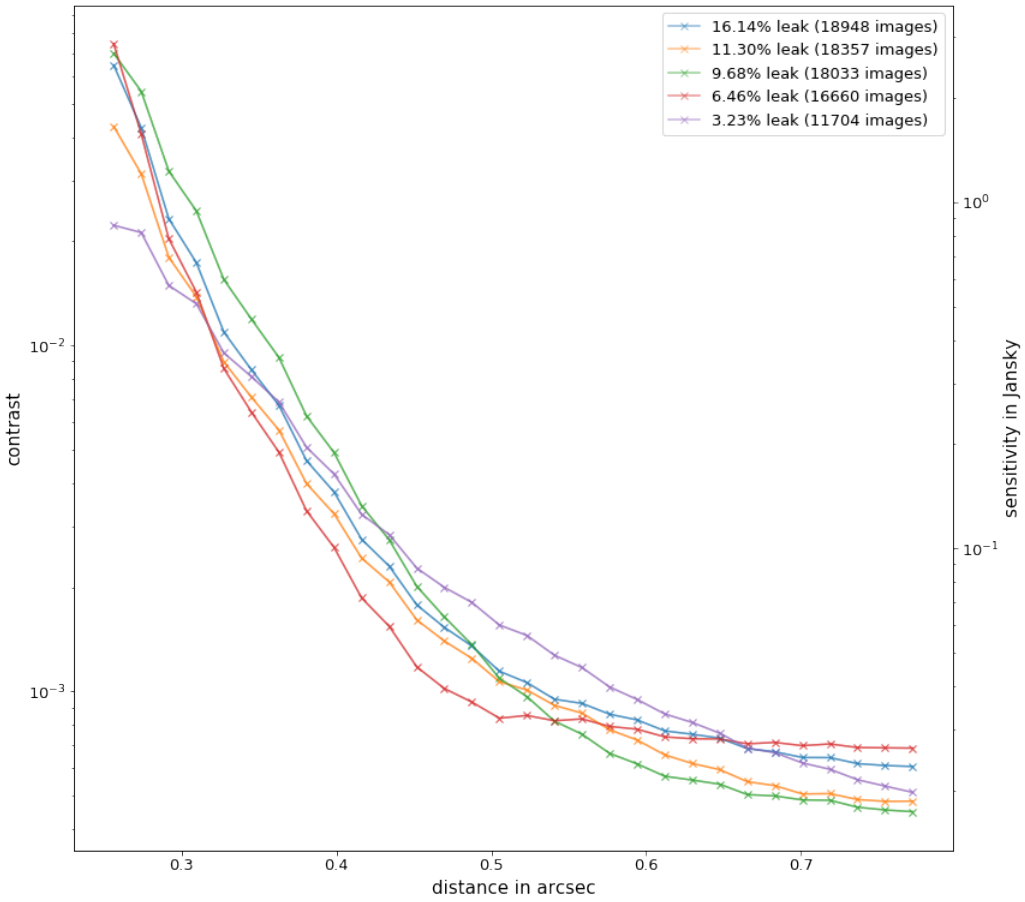

Figure 5.26: Contrast curves for the 2018's cube with HD177808 as a reference cube

We can see on Figure 5.26 that the overall shape of the curve is less steep than in the ADI case and seems to flatten faster in term of distance from the star. The 100% null leak threshold cube contrast curve was not plot for a better visibility as it goes to contrast of the level of 1. It shows that selections greatly improve the contrast curve even far from the star. Taking now a closer look at the contrast curves values at 0.25 arcsec we can see that the most selective cube is, as expected, the one providing the best results. However as for the ADI technique, some of the much less selective cubes also provide surprisingly good results compare to the more selective ones. In particular the 6.46% null leak threshold cube which, despite its selection, gives the worst contrast at 0.25 arcsec. The reasons that could explain this behavior should mostly remains the same than in the ADI case and will not be further discuss here.

The contrast values at 0.77 arcsec on the other hand were unexpected as the best results are obtained with the 9.68% and 11.30% null leak threshold cubes. These cubes are close in integration time to the 16.14% null leak threshold cube but it hardly explain how they can provide such good results compare to the less selective cubes. Once again this can be explained by the fact that we did not reach the photon-noise limited regime.

We display in Figure 5.27 the final images corresponding to the contrast curves plotted in Figure 5.26 with reference PSF built with two different PCs number.

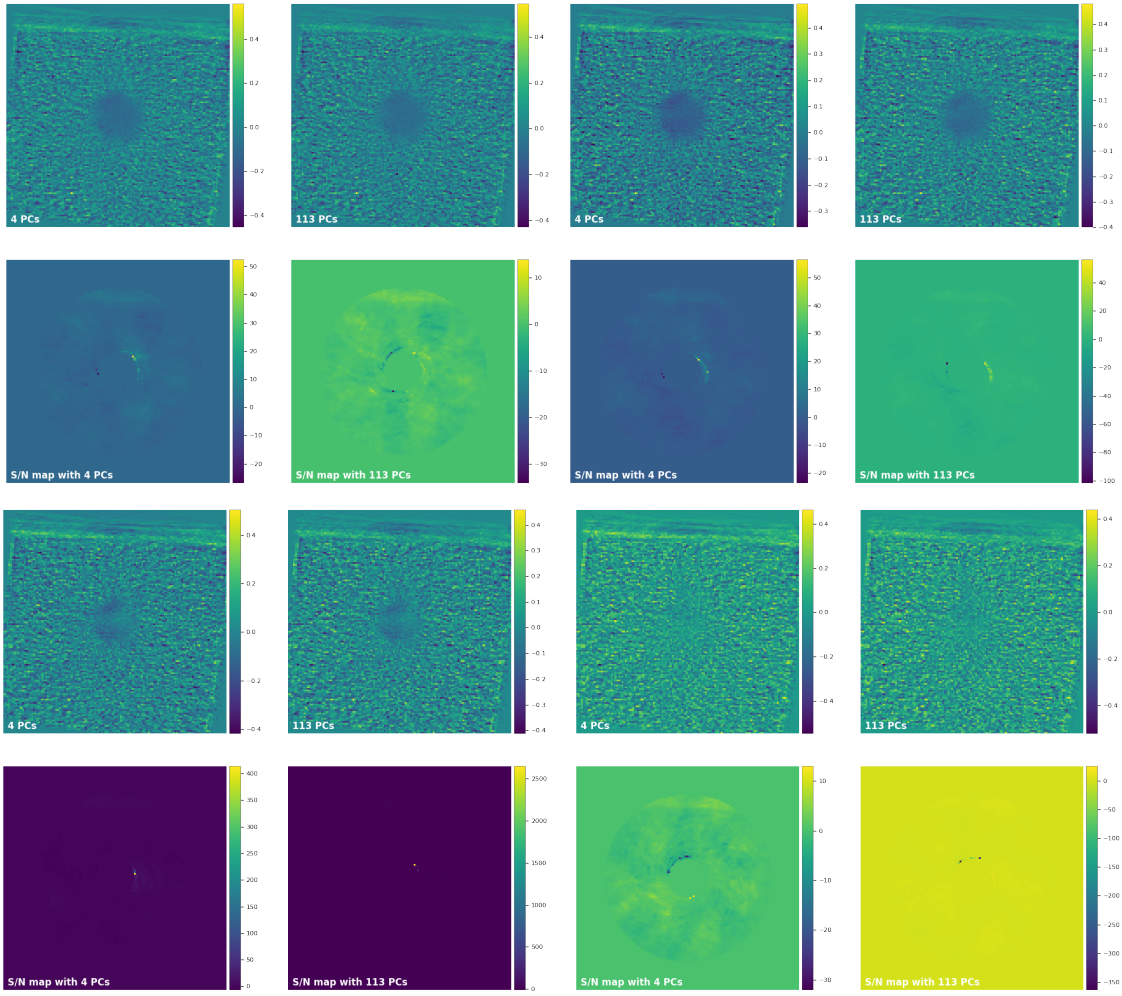

Figure 5.27: Final images for the 16.14% null leak threshold 2018's cube (top left), the 12.91% null leak threshold 2018's cube (top right),the 6.46% null leak threshold 2018's cube (bottom left) and the 3.23% null leak threshold 2018's cube (bottom right) and their S/N maps.

As for the ADI technique we then analyse the merged cube, with the same calibrator and number of PCs. Those results are displayed in Figure 5.28.

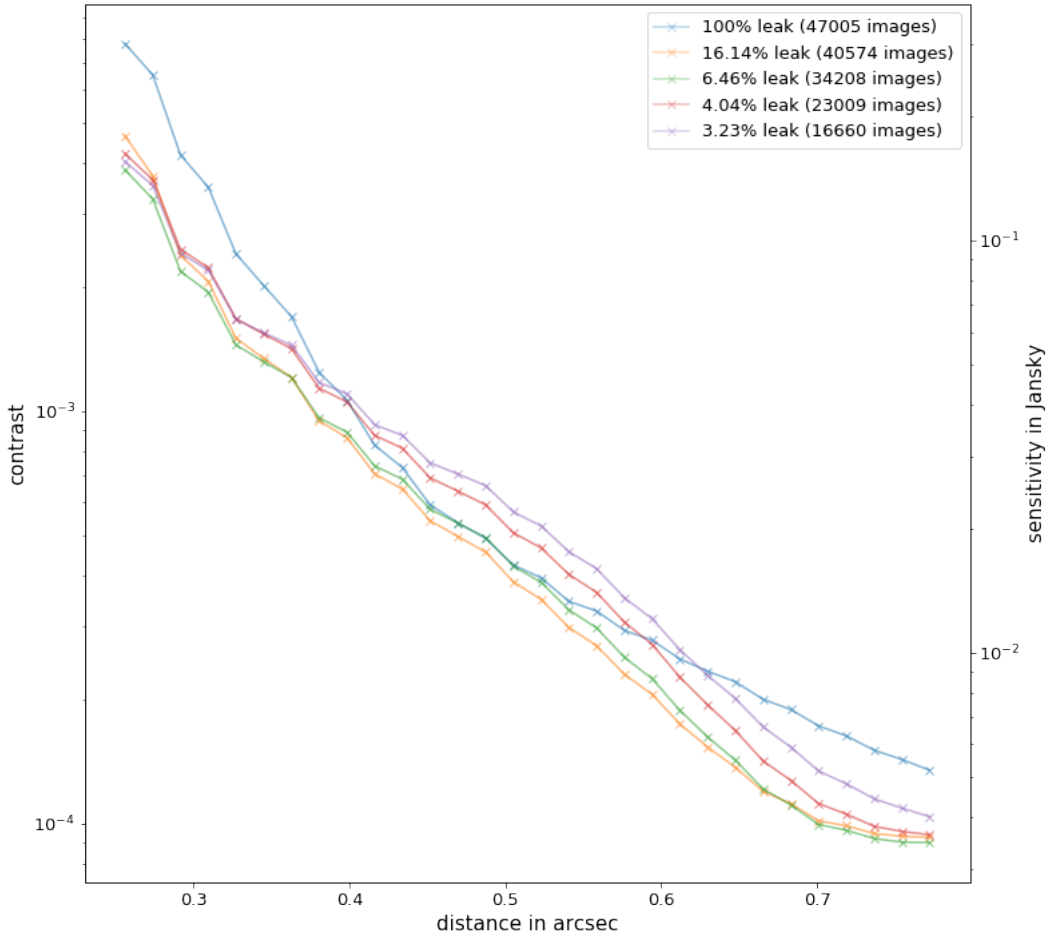

Figure 5.28: RDI Contrast curve for the merged cube using the HD177808 reference cube

If we have, this time, been able to plot the 100% null leak threshold cube with the cleaned cubes, it still presents a contrast curve significantly worse than the more selective cubes. However, as in the case of ADI, we can notice an overall improvement of the contrast curves. If once again we focus on the contrast values at 0.25 arcsec we can see much more expected results. The three most selective cubes give the best results and the inversions, if still present, are much less important and between cubes closer in null leak threshold. On the other hand, if we look at 0.77 arcsec we find a much more surprising result. Indeed at this distance from the star the best contrast curve should be provided by the cubes with the greatest integration times but are here given by the cubes with the shortest ones. This might be, as for the other cases, due to the fact that we did not reach the photon-noise limited regime yet. But such huge inversions would still be very interesting to investigate, however, this is beyond the scope of this master thesis.

We display in Figure 5.29 the final images corresponding to the contrast curves plotted in Figure 5.28 for reference PSF built from two different numbers of PCs.

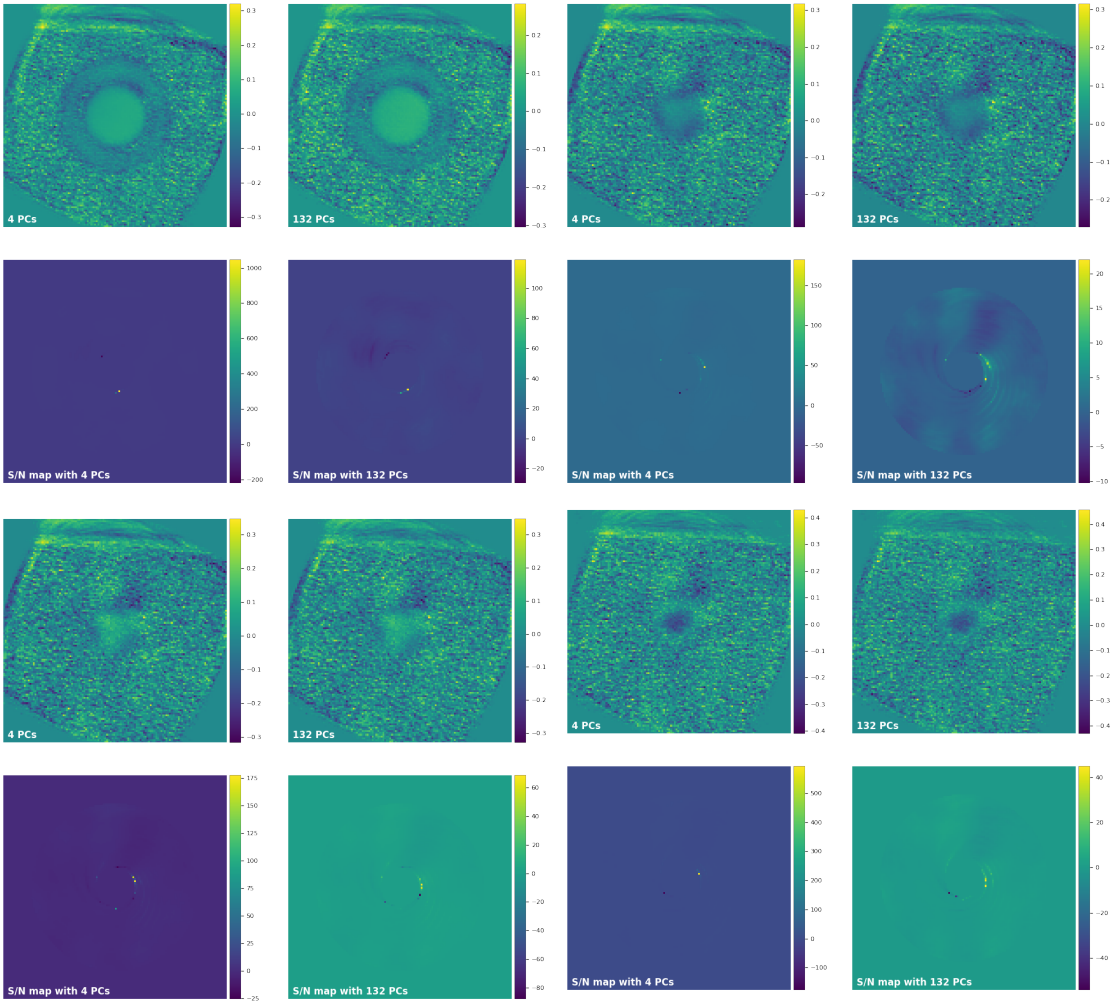

Figure 5.29: Final images for the 16.14% null leak threshold merged cube (top left), the 11.91% null leak threshold merged cube (top right), the 6.46% null leak threshold merged cube (bottom left) and the 3.23% null leak threshold merged cube (bottom right) and their S/N maps.

To better understand the impact of each parameter on the RDI processing of this cubes we then compare the two same pairs of cube than in the ADI case: one pair presenting the same null leak threshold but a different range of parallactic angles and integration time; and the other presenting the same null leak threshold and range of parallactic angles but different integration times.

As for ADI we first compare the two 8.07% null leak threshold cubes with different integration times and parallactic angles range to better understand their impact in the case of a RDI treatment and if their is notable difference with the ADI case. This comparison is shown in Figure 5.30.

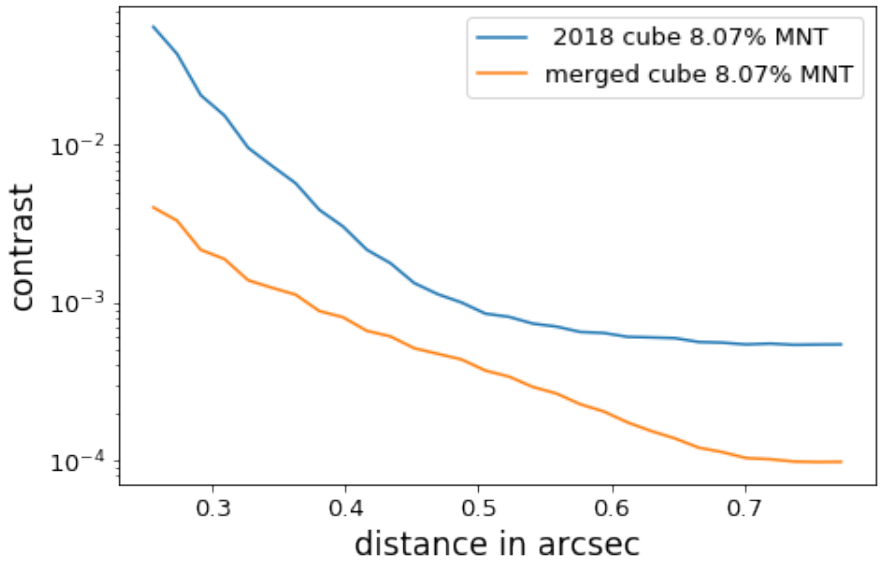

Figure 5.30: Comparison between the 2018's and merged 8.07% null leak threshold cubes. As expected we notice an overall improvement of the contrast curve due to the combination of the integration time gain and the widening of the parallactic angles range. Further comparison is needed to determine which parameter has the strongest impact.

As we can see here again we found a significant improvement of the contrast curve and, as for the ADI case this improvement is stronger close to the star. This would tend to indicate with this technique too that the parallactic angles range widening is also much more efficient than the integration time increase. This result in however much more surprising than in the ADI case as the RDI technique has been developed in order to provide better results close to the star than with ADI which needed larger parallactic angles range. This is thus surprising that the RDI technique displays such sensitivity to the parallactic angles range.

However to check if no additional effect from the integration time increase could explain at least in a part this surprising result, we also compare the modified and original 14.53% null leak threshold cubes as in the ADI case. This comparison is shown in Figure 5.31.

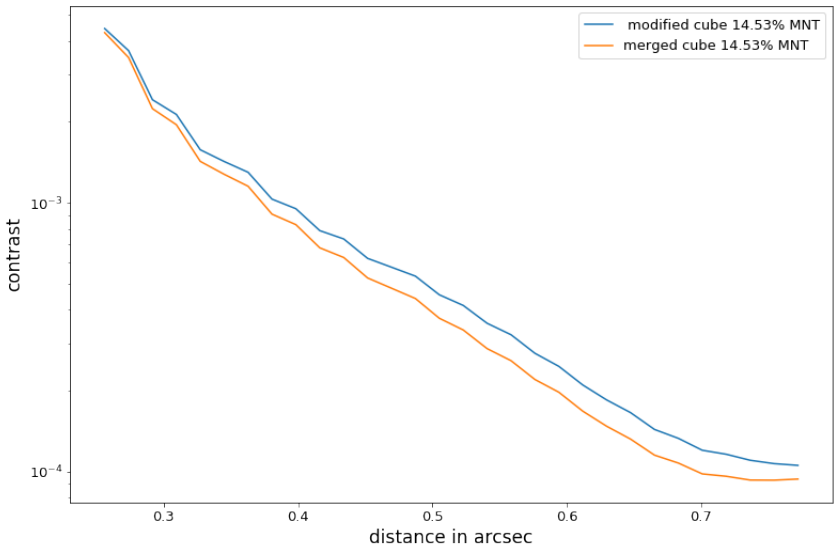

Figure 5.31: Comparison between the modified and original 14.53% null leak threshold cubes. We can see that the improvement of the contrast curve due to the integration time gain is very weak suggesting a stronger impact of the parallactic angles range.

On this figure we can see, as in the ADI case, that the effect of the integration time increase is very small, in particular compared to the one observed on the previous comparison. However, with this technique we do not observe an inversion as in the ADI case, which would tend to indicate that the RDI technique is more sensitive to the integration time increase than the ADI technique or on the contrary that it is less sensitive to the improvement of the null quality.

The comparison made on the RDI's α Lyrae results tends to indicate, as in the ADI case, that the parallactic angles range widening would be more efficient to improve the contrast curves than the integration time increase. Once again, despite this tendency we should remember that the parallactic angles range has been multiplied by 3.5 when the integration time as only been doubled and that it might have an impact on those comparisons.

5.3.2 β Leo

For the RDI treatment of β Leo we first compare the quality of the contrast curves provided by each calibrator, for the Mean and for the Median 11,75% null leak threshold cubes. We present these results in Figure 5.32 and 5.33

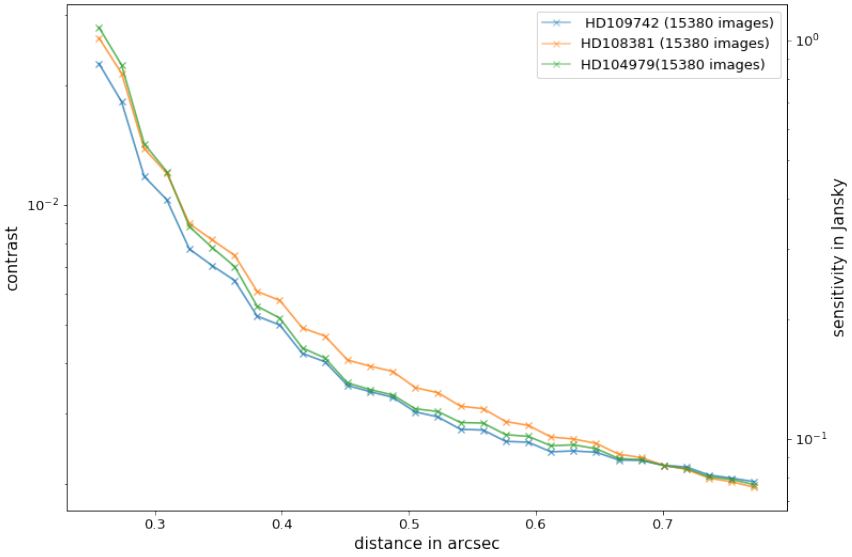

Figure 5.32: Comparison of the different calibrators for the Median background subtraction method. On the contrary of α Lyrae all the calibrators give very similar results. This is true also for other MNT levels.

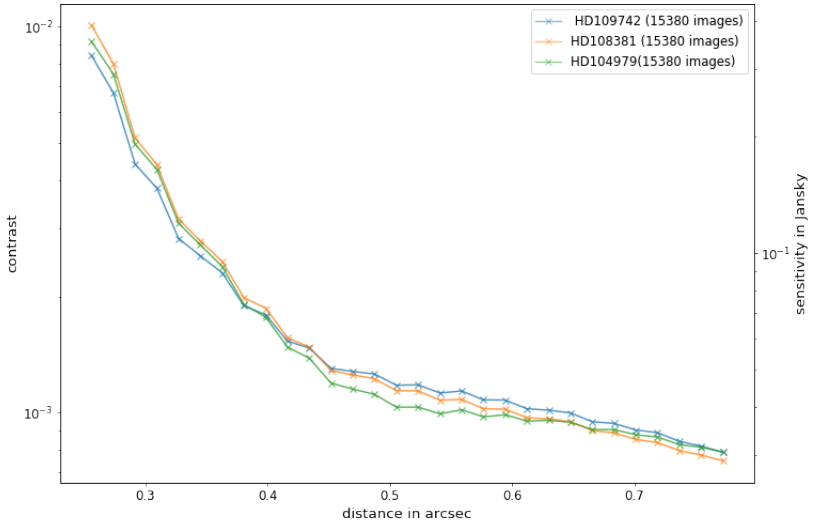

Figure 5.33: Comparison of the different calibrators for the Mean background subtraction method. On the contrary of α Lyrae all the calibrators give very similar results. This is true also for other MNT levels.

As we can see on Figure 5.32 , the calibrator HD109742 is the best at all distances from the star until 0.62 arcsec. On the other hand for the Mean cubes, HD109742 is better close to the star and HD104979 further from it. On the contrary of α Lyrae, it seems that we cannot choose one calibrator that will give overall the best results for all the cubes for both subtraction methods. This is even more true when we consider the 100% null leak threshold cubes where HD108381 gives fairly good results. Considering this we decided to perform the analysis of the cubes with all the three calibrators at our disposal. However, for a better visibility, we decided to show only the con-

trast curves for HD109742. These curves provide a good insight of the changes between the cubes of different integration times and background subtraction, however, they do not provide the best contrast curves we obtained. Indeed for RDI the best contrast we reached were obtained thanks to HD108381. We do not show this result in this section but in the section dedicated to the comparison of the ADI and RDI methods. The contrast curves for HD109742 are shown in Figure 5.34.

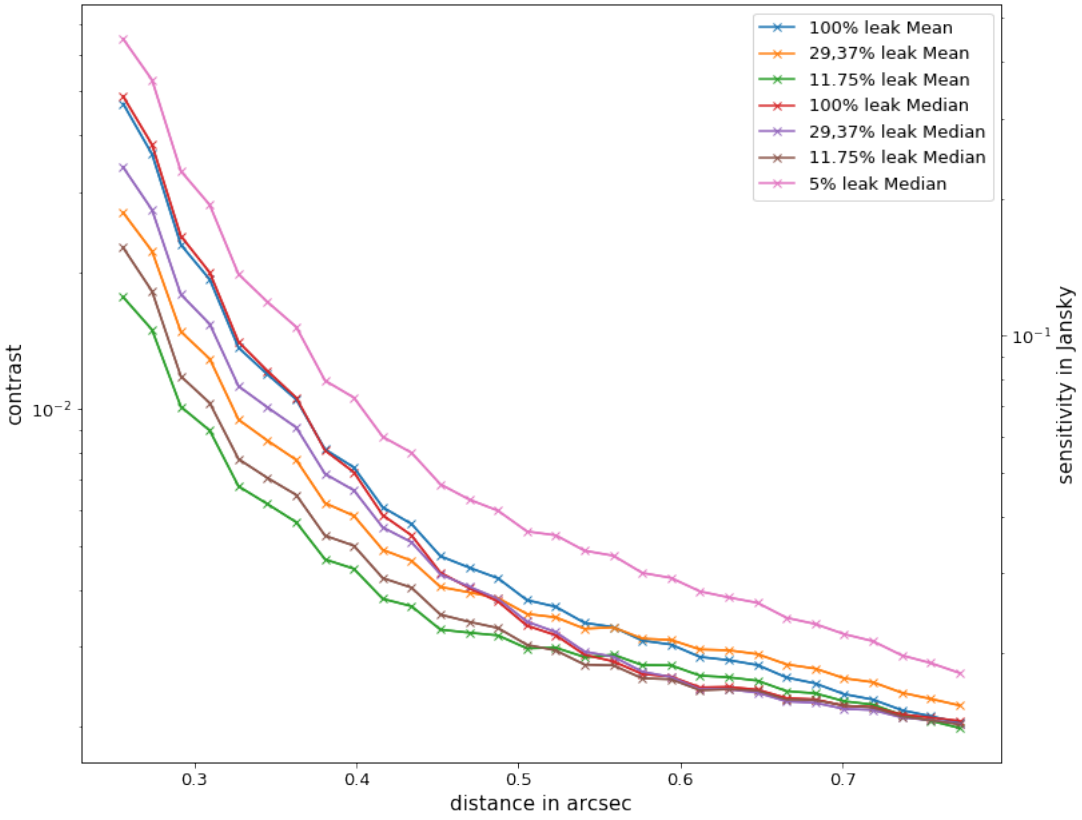

Figure 5.34: Contrast and sensitivity curves for the Mean and Median background subtraction methods with HD109742 as calibrator

The Mean 5% null leak threshold cube is not represented here due to its contrast at 1 which would have degrade the visibility. As we can see at 0.25 arcsec, but for the 5% null leak threshold the contrast behavior is exactly the one expected: the most selective cubes gave the best results. In addition, we can see that the curves obtained thanks to Mean background subtraction method are always slightly better than their Median equivalent. Once again the results obtained by the 5% null leak threshold cubes can be explained by their very small number of frames compared to the other, less selective, cubes. From 0.25 to 0.52 arcsec the best result is obtained thanks to the Mean 11,75% null leak threshold cube and from 0.52 arcsec to 0.62 arcsec by the Median 11,75% null leak threshold cube. This suggests that close to the star the Mean method might be better for RDI and that the Median method might be more adapted far from the star.

We display in Figure 5.35 the final images for the Mean and Median cubes respectively, with their S/N maps. One image for each has been built with a PCs number equal to 4 and one other with an optimized number of PCs.

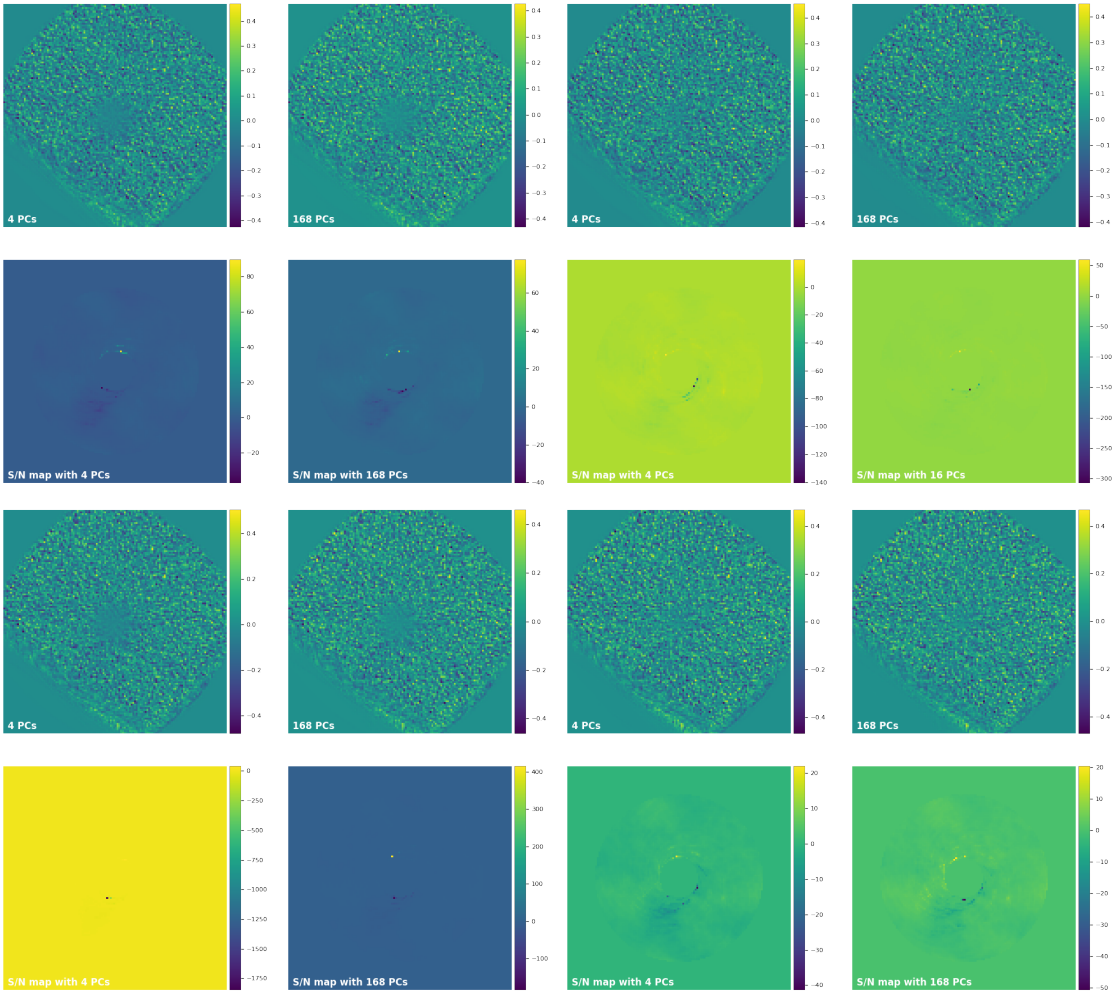

Figure 5.35: Final images for the 100% null leak threshold Mean cube (top left) and the 11.75% null leak threshold Mean cube (top right),the 100% null leak threshold Median cube (bottom left) and the 11.75% null leak threshold Median cube (bottom right) with their S/N maps.

As for the ADI treatment we then compare interesting cubes to estimate the effect of the different parameters of the cubes. Once again we can compare the Mean and Median background subtraction methods on Figure 5.34. For the other calibrators, if some Median cube can be better close to the star than their equivalent Mean cube, in the vast majority of the cases the Mean background subtraction method gave the best results. Far from the star, as for HD109742, inversions are much more frequent and Median cubes are often better than Mean cubes. We also compare, for both those methods the impact of the integration time. As in the ADI case we built a modified cube with only one image over two from the original cube. These results are shown in Figure 5.36.

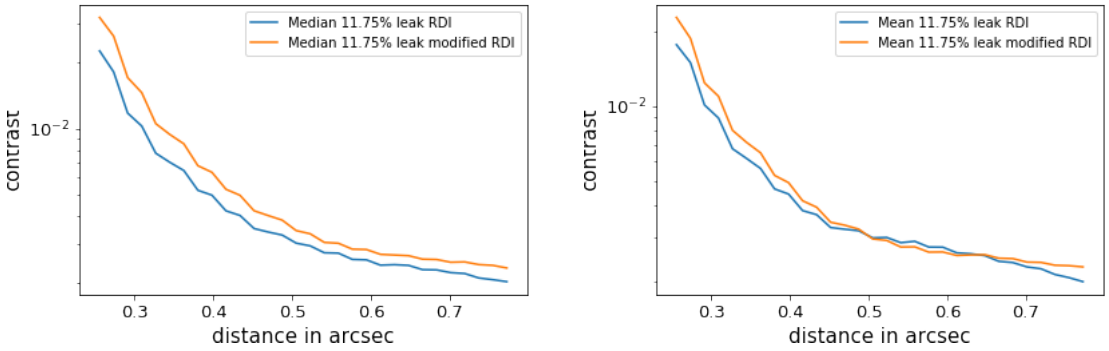

Figure 5.36: Comparison between the integration time modified cube and the original one for the Median (left) and Mean (right) background subtraction method.

As we can see for the Median cubes, the reduction of the integration time degrades the whole contrast curve. However, this effect is more mitigate for the Mean subtraction method as it shows between 0.5 and 0.6 arcsec better results for the modified cube than the original. A possible explanation for this result is the level of noise that has been discard from the modified cubes which might be more advantageous than in the original cube.

Then, as in the ADI case, we did a second comparison to estimate the effect of the parallactic angles range. For this we once again built a cube which only takes the first half of the images from the original cube thus reducing the integration time at the same value as for the previous modified cube while significantly narrowing the parallactic angles range. These results are shown in Figure 5.37.

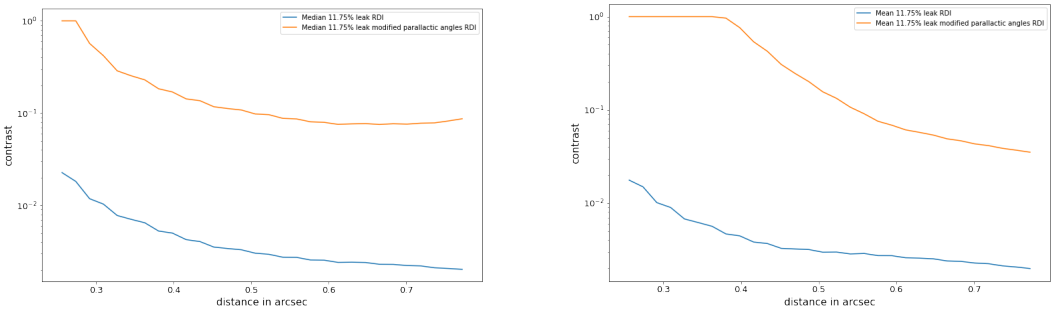

Figure 5.37: Comparison between the parallactic angles modified cube and the original one for the Median(left) and Mean (right) background subtraction method.

We can see a huge degradation of the contrast curves when the parallactic angles range is reduced. It is also interesting to note that the degradation is even stronger in the case of the Mean cube, suggesting that the Mean background subtraction method is more sensitive to the parallactic angles range than the Median background subtraction method. This degradation is much greater than in the case of a reduction of the integration time and so mainly due to the narrower range of parallactic angles. This shows, as in the ADI case that widening the parallactic angles range to improve the contrast curves is here much more efficient than increasing the integration time.

Comparison of the methods

6.1 α Lyrae

We first compare the processing with no PSF subtraction (see section 5.1.1) with the ADI processing (see section 5.2.1). To make this comparison, we plotted the two best curves of the simple analysis, one for the Mean derotated image and the other for the Median derotated image, along with the contrast curves obtained for various 2018's cubes in the ADI processing. This is shown in Figure 6.1.

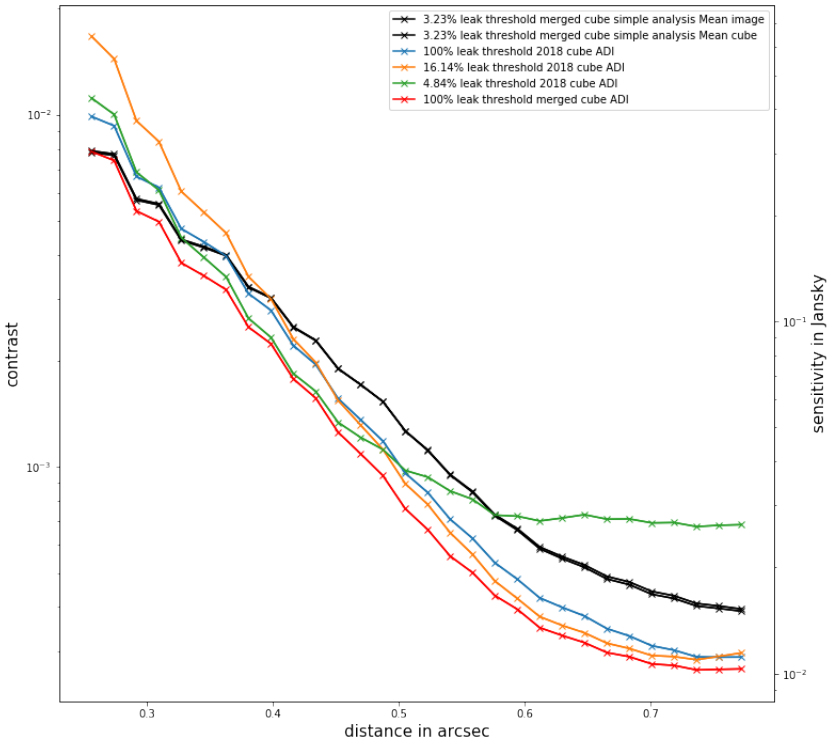

Figure 6.1: Comparison between the ADI processing and the processing without subtraction. The two black curves corresponds to the best curves of the processing without PSF subtraction. The red curves represent the worst curve obtained with ADI for the merged cube.

As we can see the processing without any subtraction provides better results very close to the star but the ADI processing proves to be more efficient everywhere else for the 2018's cubes. One can also notice that the 100% null leak threshold merged cube provides better result at all distances. It is thus clear that the ADI technique is generally more efficient than the processing

without any subtraction for α Lyrae.

In order to compare the ADI and RDI results for the analysis of α Lyrae 's merged cube, we choose to plot for each cubes the most external and the most internal values of the contrast (at 0.77 and 0.25 arcsec from the star respectively) for both techniques. This is shown in Figure 6.2.

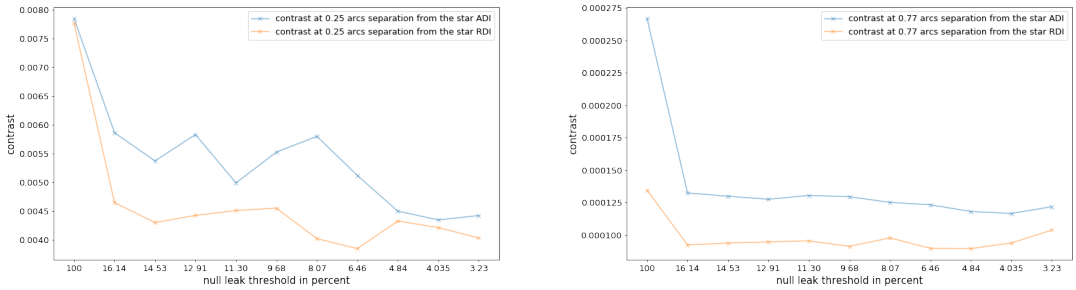

Figure 6.2: Comparison of the contrast behavior for the ADI and RDI techniques at 0.25 arcsec (left) and 0.77 arcsec(right)

Figure 6.2 allows to easily compare the most adapted method for those two extreme distances from the star but also with respect to the selection operate on the flux. As expected the RDI technique displays better results close to the star. However a much more surprising result is the tendency of the RDI results to be better far from the star too compared to those obtained thanks to ADI. It is however important to note that the differences in contrast between ADI and RDI are larger by one order of magnitude close to the star.

Another interesting result is found when comparing the ADI and RDI techniques with the 2018's cube images only. Indeed as shown in Figures 6.3, the ADI technique gives extremely good results compared to the RDI technique.

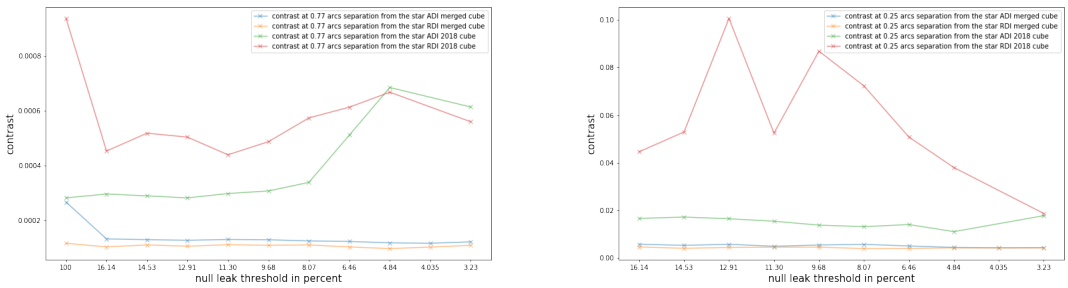

Figure 6.3: Comparison of the ADI and RDI techniques for both the merged cube and the 2018's cube alone at 0.77 (left) and 0.25 (right) arcsec from the star.

As we can see on the left graph the RDI results close to the star are better than far from it and this is coherent with the particularities of those techniques. However, even with this nuance it is still obvious than ADI works much better on this cube but for the most selective ones close to the star. This seems to indicate that the 2018's cube is very well suited for the ADI technique or, on the opposite, that it is not all adapted for RDI technique. We found interesting to further study this difference of results for ADI and RDI between the merged and the 2018's cube. To do so we first make another comparison on the 2017's cube alone. These results are presented in Figure 6.4.

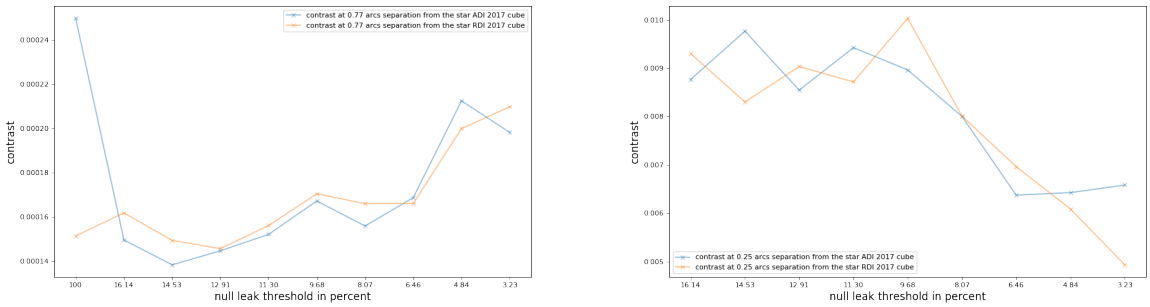

Figure 6.4: Comparison of the ADI and RDI technique for the 2017's cubes at 0.77 arcsec (left) and at 0.25 arcsec (right). For this cube the results provide by RDI and ADI are much more similar. Suggesting that some parameters of the 2018's cube might be responsible for the poor results obtained in RDI.

As we can see in Figure 6.4, the results for both techniques are much more similar (an order of magnitude) than in the 2018's case. The 2017's cubes have slightly more integration time for the 16.14%, 14.53%, 11.91%, 9.68% and 8.07% null leak threshold cubes, about the same integration time for the 6.46% and 4.84% null leak threshold cubes and less integration time for the two most selective cubes. But those graphs do not display any behavior which would tend to indicate that this slight integration time difference is responsible for the better results of RDI in the 2017's cubes. Another parameter which differentiates those two cubes and thus can play a role in the better results of RDI is the overall null quality of the 2017 original cube (less images with very bad null quality -above 100 000 ADU and even above 60 000 ADU- but less images with very good null -below 30 000 ADU) is better than the 2018's cube one. As the two cubes were not observed on the same night the observing conditions might play an important role too in those differences. However the parameter which differentiates the most those two cubes is the parallactic angles range. Indeed the 2018's cubes only have 10° of parallactic angles range whereas the 2017's cubes possess a 25° range.

If we start from the postulate that the greater parallactic angle range of the 2017's cubes has a positive impact of the results from the RDI technique it can seem contradictory as this method has been developed not to be sensitive to the parallactic angle range. Another contradictory observation is that the improvement of the results are greater far from the star where ADI is supposed to be more adapted. Considering those contradictions it is uneasy to determine which parameters of the cubes lead to the results obtained for the merged cube where RDI provides on the whole curve better results. A possibility resides in the fact that even with the combined parallactic angles range (35°) the calibrator used for α Lyrae (HD177808) still has a greater impact, and that the bad results obtained with the 2018's cube are due to a lesser correlation with the calibrator. In this hypothesis the 2017's cubes are also more suited for the RDI PSF subtraction built with HD177808 and that can explain the difference between those two cubes without the intervention of any other parameters. In this way the parameters which increase the quality of RDI between the 2017's cubes and the merged cubes would be the integration time and this would finally be consistent with the RDI technique. However as the calibrator HD177808 has been observed on the night 2018-03-28, it is unclear why the 2017's cubes would be more adapted to this calibrator.

It would also be interesting to investigate the effect of a Mean or Median image subtraction before running the FFPCA processing with the RDI technique in order to compare the improvement of the contrast curves with this additional subtraction. However this will not be done in this master thesis.

6.2 β Leo

A first comparison was made between the processing without any subtraction and the ADI processing. To do so we took the best curves close to the star and far from the star for both technique, this is presented in Figure 6.5

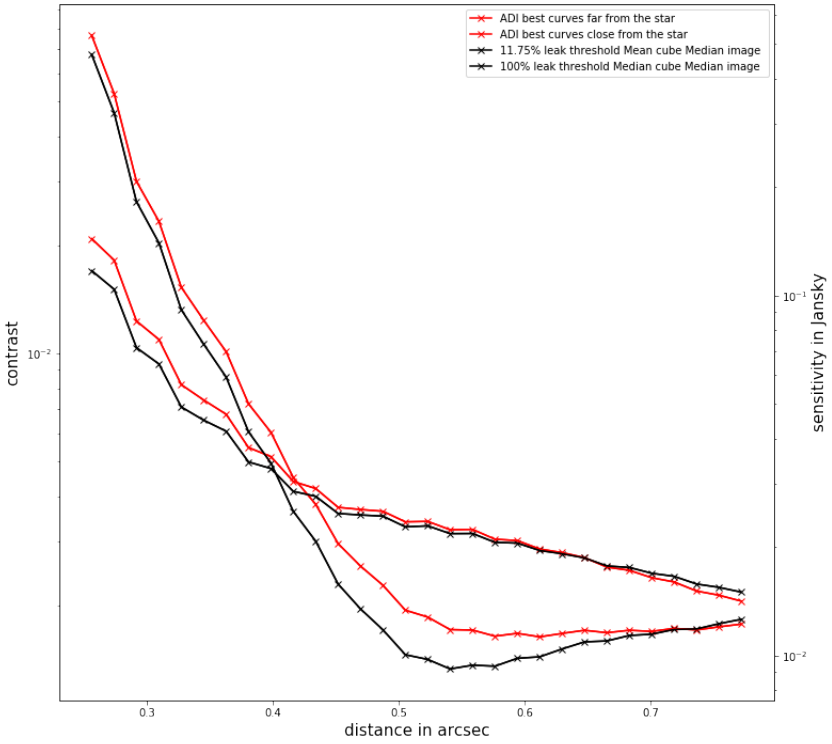

Figure 6.5: Comparison between the ADI technique and the processing without PSF subtraction. The black curves correspond to the processing without PSF subtraction while the red ones correspond to the ADI processing.

As we can see in Figure 6.5, the processing without subtraction provides better results everywhere but very far from the star. Furthermore, one should remember that at this distance we are in the cropping of the images so that the processing without any subtraction might prove to be more efficient than the ADI processing for cubes with similar parameters than those of β Leo.

We now compare the ADI and RDI techniques. Unlike α Lyrae, where one calibrator for the RDI technique proves to be better, the calibrators for β Leo were all very similar in terms of performances, and none was find to be better on the overall contrast curve. For this reason comparing the two methods through the same process than α Lyrae was much less intuitive, we so decided to plot only the best curves for ADI and RDI. These results are shown in Figure 6.6.

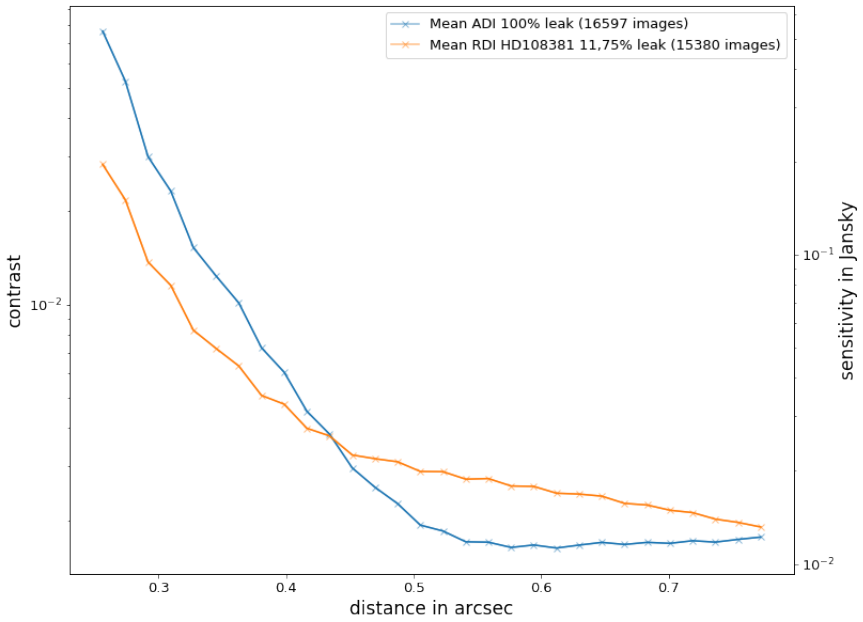

Figure 6.6: Comparison of the best contrast curve for ADI and for RDI. The RDI curve gives really good contrasts close to the star which is coherent with the purpose of RDI. ADI however stays much more efficient far from the star. This illustrates perfectly the complementarity of these two techniques.

Figure 6.6 clearly shows the complementarity of those two techniques as the RDI curve much better results close to the star and the ADI curve, on the opposite, provides much better contrast far from the star. This kind of results was much more expected than those found for α Lyrae as the RDI technique is designed to compensate the need of a greater parallactic angles range close to the star at the expense of the performance further from the star.

This new knowledge already suggests that the processing without PSF subtraction might be more adapted far from the star. We however compared the processing without subtraction to the RDI best curve. The processing without any PSF subtraction proves to be once more more adapted than the more complex techniques. A possible explanation of this result is the good null quality of the overall cube, and thus the important amount of kept frames even with very selective criteria on the flux.

However, one should remember the very good contrast we obtained with a subtraction of the Mean or the Median image of the cubes for the ADI processing. Indeed it improves the contrast curves by an order of magnitude thus providing much better result than the processing without subtraction. However the subtraction of the Mean and Median image of the cubes before derotating the images and process without PSF subtraction (after the images have been derotated) have proven to degrade the curves. So if we consider this pre-subtraction of the Mean or the Median images of the cubes, the ADI technique proves to be the more powerful. As for α Lyrae, it would be very interesting to conduct a similar experience for the RDI technique but this will not be done either in this master thesis.

6.3 Comparison of α Lyrae and β Leo results

First of all we should remember the parameters that differentiate α Lyrae and β Leo cubes. The most obvious is of course that the two stars do not have the same brightness, see Table 3.1. They also have really different integration times. As an example the most selective merged cube of α

Lyrae is about the same integration time that the 100% null leak threshold cube of β Leo. Further more, if β Leo's cubes possess a wider range of parallactic angles (16) than α Lyrae 2018's cube (10) it is much narrow than the merged cube of α Lyrae (35). Another parameter is the overall null quality of the cubes. Indeed, β Leo's cubes tend to show a better null quality, and a very strict selection has been applied without discarding an important amount of frames. Finally, a last parameter which the impact would be much more difficult to investigate is the excess in zodis level of β Leo which ha been detected while no excess has been found for α Lyrae. From those parameters we will try to find conclusions about the cubes which are more adapted to each methods.

As see in the two previous sections, α Lyrae and β Leo are not adapted for the same method. Indeed the best method for α Lyrae seems to be the RDI technique while for β Leo it is the processing without subtraction. Once again, one should remember than with a pre-subtraction of the Mean or Median image of the cubes for the RDI technique could change the results of this comparison. However, from the data we are able to compare today, we will start with the assumption that RDI and processing without subtraction are the methods which respectively give the best results for α Lyrae and β Leo.

A first interesting comparison is to be made between the results obtained with the processing without subtraction for both stars. Indeed if it works really well with β Leo it however does not provides as good results for α Lyrae. As no subtraction is operated, it would be very surprising that the source of this difference comes from the different parallactic angles range. However a good way to prove this hypothesis would be to run a processing without subtraction on cubes with only the half of the parallactic angles range and compared it with the results for cubes with only the half of the integration time and the total merged cubes. Another parameter that might play an important role is the integration time. Indeed as α Lyrae's cubes have greater integration times and on overall lower null quality, the summation of the remaining light is much more important than in the case of β Leo. If we look at the Mean or Median derotated images (Figure 5.1 and Figure 5.5) for both cubes we can clearly see that there are much less remaining light in β Leo's. As there is no subtraction in this case, the combination of those two parameters seems to be a coherent explanation for the difference of efficiency of this method for the two stars.

A second comparison must be made for the ADI technique. Indeed if it works well (in particular with the pre-subtraction of the Mean or Median images) and does not provide surprising results for β Leo, it is not the case for α Lyrae. As we can see on Figure 6.6 the ADI technique works better far from the star while the RDI technique is more adapted for the close in probing. However as we discussed in the previous sections, RDI provides better results for α Lyrae's merged cubes. This difference can seem even more surprising knowing that β Leo's cubes possess narrower parallactic angles range than α Lyrae's. The brightness of α Lyrae and the overall lower null quality of its cube is a possible explanation of this difference. Indeed the need for wider parallactic angles range could be even stronger at greater separation due to the brightness of the star. However this hypothesis hardly explained the situation for the whole curve. Indeed it is unlikely that this proposition extends to the whole frame until 0.77 arcsec. Further investigation of this situation would be needed to fully understand this result, but this is beyond the scope of this master thesis.

Finally, one should mention that the zodis level might impact the efficiency of the different methods, in particular for RDI and ADI. Indeed as the reference stars do not necessarily have the same zodi levels, the RDI might be more or less impacted whereas the ADI technique, as it builds the reference PSF from the images of the target star, would take into account this parameter. However, as the exozodiacal disks are much probably really close to the star and that the ADI technique knows limitations at small separation, due to the need of parallactic angles range, such impact is much probably really limited.

Conclusion and Prospects

In this master thesis, we analyse the images of two emblematic A stars α Lyrae (Vega) and β Leo (Denebola) taken during the HOSTS survey with the LBTI in nulling mode at 11μm. The goal of this master thesis is twofold: looking for the signature of resolved circumstellar emission and characterize the performance of the LBTI, in nulling interferometry mode, with the different processing methods at our disposal. To our knowledge, this is is the first time that images obtained using nulling interferometry as coronograph are analysed using classical imaging processing techniques such as PCA. In this work, we compared different processing methods and their performance with respect to several parameters of the data cubes. We first began by processing the image cubes without PSF subtraction and then move to the ADI and RDI processing. We did all this processing for α Lyrae and β Leo. This allows us to compare the efficiency of these different methods and estimate the imaging performance of the LBTI. This allows us to determine which parameters are more likely to positively impact the efficiency of one method or on the contrary to degrade its efficiency.

Regarding the performance of the LBTI, the best contrast obtained in this study was obtained on α Lyrae with the RDI technique by two different cubes with respective integration times of 30 and 25 minutes and reach, at large angular separation (0.77 arcsec), 10^{-4}, corresponding to about 4.10^{-3} Jansky in sensitivity (16.14 and 6.46 % null leak threshold merged cubes, see Figure 5.28). However, the ADI technique with the pre-subtraction provides even better results: 8.10^{-5} in contrast at 0.25 arcsec and 3.10^{-5} in contrast at 0.77 arcsec which corresponds respectively to 2.10^{-3} and almost 10^{-3} Jansky in sensitivity for 12 minutes of total integration time (3.23% null leak threshold cube, see Figure 5.21). It is however important to note that this pre-subtraction might be too optimistic given the limited parallactic angle range and was not made for RDI and that this last technique combined with this pre-subtraction might still be more efficient than ADI for α Lyrae.

The best contrast obtained for β Leo, excluding the pre-subtraction, were obtained with the processing without PSF subtraction, and reach about $1.5.10^{-3}$ in contrast and 9.10^{-3} Jansky in sensitivity for 16 minutes of integration time (100% null leak threshold) at 0.55 arcsec (see Figure 5.5). However, as for α Lyrae, the pre-subtraction combined with the ADI methods give even better results: 4.10^{-4} in contrast and $3.5.10^{-3}$ Jansky in sensitivity 15 minutes of integration time (11.75% null leak threshold Mean cube, see Figure 5.24). Once again this pre-subtraction was not apply to RDI and this technique might provide similar results than ADI if we do apply this pre-subtraction. However the pre-subtraction was applied to the processing without PSF subtraction and does not give any improvement of the contrast curve.

This analysis, applied to nulling interferometry, brings several surprising results that we think deserve further investigation. A first interesting result was obtained during the analysis of β Leo. Indeed, we observed that the mean background subtraction approach provides better contrasts, for ADI and RDI, than the Median background subtraction (see Figure 5.16 and Figure 5.34). On the contrary, for the processing without PSF subtraction the Median background subtraction tends to gives better results (Figure 5.5). This analysis has, however, been conducted on only one star and it would be interesting to extend this study to other stars. This would prove to be very useful to constrain the reduction and observing parameters which lead to better performances.

Another surprising result was found when considering the impact of the parallactic angle ranges

of the cube on the improvement of the contrast curves. This analysis was performed on both stars for the ADI and RDI techniques. The comparison was made thanks to two modified cubes: one with only one in two images from the original cube allowing to estimate the integration time impact and one with only half of the original cube. By comparing those two with the original cube we find out that the parallactic angles have a much greater impact on the improvement of the contrast curves for both stars and both techniques (see Figure 5.14 and 5.19 for ADI and Figure 5.30 and 5.37 for RDI). This indicates that the final sensitivity is limited by contrast over the whole field-of-view. This result seems surprising for RDI which should be independent of the parralactic angle range. Further investigating those results will be of great interest for future nulling interferometry images processing and to improve them.

A third surprising result was found when we tried to improve the ADI contrast curves. Indeed, by subtracting the Mean or the Median images of the cubes to each individual frame before running the FFPCA processing, we significantly improve the reachable contrast. This was performed for both stars with the ADI technique. In each case we found that this pre-subtraction improves the contrast curves by one order of magnitude (report to Figure 5.21 for α Lyrae and Figure 5.24 for β Leo). We also tried this pre-subtraction on the processing without PSF subtraction but it degrades the contrast curves in each case. A first step to further understand this improvement would be to realize the same test with the RDI technique and to compare those new results with the ADI ones. Of course extending this analysis to more stars would also be of great help to understand why this pre-subtraction is so efficient.

Extending the different analyses made during this master thesis to a larger sample of stars would be of great interest to further understand the result mentioned above and to put stronger constraints on the parameters which lead to such results. Adding the stars for which the HOSTS Survey has found an infrared excess would also be particularly interesting. If one wants to investigate the impact of zodis levels on such results pursue with stars without detected excess would be an important addition to this analysis. It would also be particularly interesting to study the impact of more complex background subtraction methods on the obtained contrast curves, such as the PCA methods (Hunziker et al (2018)).

Bibliography

Amara A, Quanz S (2012) PynPoint: An Image Processing Package for Finding Exoplanets. Monthly Notices of the Royal Astronomical Society 427(2):948–955, DOI 10.1111/j.1365-2966.2012.21918.x, URL http://arxiv.org/abs/1207.6637, arXiv: 1207.6637

Bracewell RN (1978) Detecting nonsolar planets by spinning infrared interferometer. Nature 274(5673):780–781, DOI 10.1038/274780a0, URL https://www.nature.com/articles/274780a0, number: 5673 Publisher: Nature Publishing Group

Defrère D, Hinz PM, Mennesson B, Hoffmann WF, Millan-Gabet R, Skemer AJ, Bailey V, Danchi WC, Downey EC, Durney O, Grenz P, Hill JM, McMahon TJ, Montoya M, Spalding E, Vaz A, Absil O, Arbo P, Bailey H, Brusa G, Bryden G, Esposito S, Gaspar A, Haniff CA, Kennedy GM, Leisenring JM, Marion L, Nowak M, Pinna E, Powell K, Puglisi A, Rieke G, Roberge A, Serabyn E, Sosa R, Stapeldfeldt K, Su K, Weinberger AJ, Wyatt MC (2016) Nulling Data Reduction and On-Sky Performance of the Large Binocular Telescope Interferometer. ApJ 824(2):66, DOI 10.3847/0004-637X/824/2/66, URL http://arxiv.org/abs/1601.06866, arXiv: 1601.06866

Ertel S, Defrère D, Hinz PM, Mennesson B, Kennedy GM, Danchi WC, Gelino C, Hill JM, Hoffmann WF, Mazoyer J, Rieke G, Shannon A, Stapelfeldt K, Spalding E, Stone JM, Vaz A, Weinberger AJ, Willems P, Absil O, Arbo P, Bailey VP, Beichman C, Bryden G, Downey EC, Durney O, Esposito S, Gaspar A, Grenz P, Haniff CA, Leisenring JM, Marion L, McMahon TJ, Millan-Gabet R, Montoya OM, Morzinski KM, Perera S, Pinna E, Pott JU, Power J, Puglisi A, Roberge A, Serabyn E, Skemer AJ, Su KYL, Vaitheeswaran V, Wyatt MC (2020) The HOSTS survey for exozodiacal dust: Observational results from the complete survey. AJ 159(4):177, DOI 10.3847/1538-3881/ab7817, URL http://arxiv.org/abs/2003.03499, arXiv: 2003.03499

Gomez Gonzalez CA, Absil O, Absil PA, Van Droogenbroeck M, Mawet D, Surdej J (2016) Low-rank plus sparse decomposition for exoplanet detection in direct-imaging adi sequences. Astronomy Astrophysics 589:A54, DOI 10.1051/0004-6361/201527387, URL http://dx.doi.org/10.1051/0004-6361/201527387

Gonzalez CAG, Wertz O, Absil O, Christiaens V, Defrere D, Mawet D, Milli J, Absil PA, Van Droogenbroeck M, Cantalloube F, Hinz PM, Skemer AJ, Karlsson M, Surdej J (2017) VIP: Vortex Image Processing package for high-contrast direct imaging. AJ 154(1):7, DOI 10.3847/1538-3881/aa73d7, URL http://arxiv.org/abs/1705.06184, arXiv: 1705.06184

Green J, Schechter P, Baltay C, Bean R, Bennett D, Brown R, Conselice C, Donahue M, Fan X, Gaudi BS, Hirata C, Kalirai J, Lauer T, Nichol B, Padmanabhan N, Perlmutter S, Rauscher B, Rhodes J, Roellig T, Stern D, Sumi T, Tanner A, Wang Y, Weinberg D, Wright E, Gehrels N, Sambruna R, Traub W, Anderson J, Cook K, Garnavich P, Hillenbrand L, Ivezic Z, Kerins E, Lunine J, McDonald P, Penny M, Phillips M, Rieke G, Riess A, van der Marel R, Barry RK, Cheng E, Content D, Cutri R, Goullioud R, Grady K, Helou G, Jackson C, Kruk J, Melton M, Peddie C, Rioux N, Seiffert M (2012) Wide-field infrared survey telescope (wfirst) final report 1208.4012

HabEx Team (2019) HabEx Final Report p 498

Hinz PM, Defrère D, Skemer A, Bailey V, Stone J, Spalding E, Vaz A, Pinna E, Puglisi A, Esposito S, Montoya M, Downey E, Leisenring J, Durney O, Hoffmann W, Hill J, Millan-Gabet R, Mennesson B, Danchi W, Morzinski K, Grenz P, Skrutskie M, Ertel S (2016) Overview of LBTI: a multipurpose facility for high spatial resolution observations URL https://core.ac.uk/reader/77929324

Hunziker S, Quanz SP, Amara A, Meyer MR (2018) PCA-based approach for subtracting thermal background emission in high-contrast imaging data. A&A 611:A23, DOI 10.1051/0004-6361/201731428, URL https://www.aanda.org/10.1051/0004-6361/201731428

JHPoynting (1903) Radiation in the solar system ; its effect on temperature and its pressure on small bodies. Monthly Notices of the Royal Astronomical Society LXIV(2):265–266, URL http://articles.adsabs.harvard.edu/pdf/1903MNRAS..64A...1P

Kelsall T, Weiland J, Franz B, Reach W, Arendt R, Dwek E, Freudenreich H, Hauser M, Moseley S, Odegard N, Silverberg R, Wright E (1998) The *COBE* Diffuse Infrared Background Experiment Search for the Cosmic Infrared Background. II. Model of the Interplanetary Dust Cloud. ApJ 508(1):44–73, DOI 10.1086/306380, URL https://iopscience.iop.org/article/10.1086/306380

Lafreniere D, Marois C, Doyon R, Nadeau D, Artigau E (2007) A new algorithm for point spread function subtraction in high-contrast imaging: a demonstration with angular differential imaging. ApJ 660(1):770–780, DOI 10.1086/513180, URL http://arxiv.org/abs/astro-ph/0702697, arXiv: astro-ph/0702697

LUVOIR Team (2019) The LUVOIR Final Report p 426

Marois C, Lafreniere D, Doyon R, Macintosh B, Nadeau D (2006) Angular Differential Imaging: A Powerful High-Contrast Imaging Technique. ApJ 641(1):556–564, DOI 10.1086/500401, URL https://iopscience.iop.org/article/10.1086/500401

Mayor M, Queloz D (1995) A Jupiter-mass companion to a solar-type star. Nature 378(6555):355–359, DOI 10.1038/378355a0, URL https://www.nature.com/articles/378355a0, number: 6555 Publisher: Nature Publishing Group

Nesvorný D, Jenniskens P, Levison HF, Bottke WF, Vokrouhlický D, Gounelle M (2010) COMETARY ORIGIN OF THE ZODIACAL CLOUD AND CARBONACEOUS MICROMETEORITES. IMPLICATIONS FOR HOT DEBRIS DISKS. ApJ 713(2):816–836, DOI 10.1088/0004-637X/713/2/816, URL https://iopscience.iop.org/article/10.1088/0004-637X/713/2/816

Reidemeister M, Krivov AV, Stark CC, Augereau JC, Löhne T, Müller S (2011) The cold origin of the warm dust around ε Eridani. A&A 527:A57, DOI 10.1051/0004-6361/201015328, URL http://www.aanda.org/10.1051/0004-6361/201015328

Robertson HP, Russell HN (1937) Dynamical Effects of Radiation in the Solar System. Monthly Notices of the Royal Astronomical Society 97(6):423–437, DOI 10.1093/mnras/97.6.423, URL https://academic.oup.com/mnras/article-lookup/doi/10.1093/mnras/97.6.423

Ruane G, Ngo H, Mawet D, Absil O, Choquet E, Cook T, Gonzalez CG, Huby E, Matthews K, Meshkat T, Reggiani M, Serabyn E, Wallack N, Xuan WJ (2019) Reference star differential imaging of close-in companions and circumstellar disks with the NIRC2 vortex coronagraph at W.M. Keck Observatory. AJ 157(3):118, DOI 10.3847/1538-3881/aafee2, URL http://arxiv.org/abs/1901.04090, arXiv: 1901.04090

Soummer R, Pueyo L, Larkin J (2012) Detection and Characterization of Exoplanets and Disks using Projections on Karhunen-Loeve Eigenimages. ApJ 755(2):L28, DOI 10.1088/2041-8205/755/2/L28, URL http://arxiv.org/abs/1207.4197, arXiv: 1207.4197

Weinberger AJ, Bryden G, Kennedy GM, Roberge A, Defrère D, Hinz PM, Millan-Gabet R, Rieke G, Bailey VP, Danchi WC, Haniff C, Mennesson B, Serabyn E, Skemer AJ, Stapelfeldt KR, Wyatt MC (2015) TARGET SELECTION FOR THE LBTI EXOZODI KEY SCIENCE PROGRAM. ApJS 216(2):24, DOI 10.1088/0067-0049/216/2/24, URL https://iopscience.iop.org/article/10.1088/0067-0049/216/2/24

Wyatt MC (2005) The insignificance of P-R drag in detectable extrasolarplanetesimal belts. A&A 433(3):1007–1012, DOI 10.1051/0004-6361:20042073, URL http://www.aanda.org/10.1051/0004-6361:20042073